Breast Elastography Modulus Reconstruction from Simultaneous Acquisition of Stress and RF Echo Signal

by

Md. Taslim Reza

DOCTOR OF PHILOSOPHY

IN

ELECTRICAL AND ELECTRONIC ENGINEERING

Department of Electrical and Electronic Engineering
Islamic University of Technology (IUT)
Board Bazar, Gazipur-1704, Bangladesh.

April 18, 2019.

CERTIFICATE OF APPROVAL

The thesis titled, **Breast Elastography Modulus Reconstruction from Simultaneous Acquisition of Stress and RF Echo Signal** submitted by Md. Taslim Reza, St. No. 122701 of Academic Year 2012-13 has been found as satisfactory and accepted as partial fulfillment of the requirement for the Degree DOCTOR OF PHILOSOPHY IN ELECTRICAL AND ELECTRONIC ENGINEERING on April 18, 2019.

Board of Examiners:

Dr. Mohammad Rakibul Islam (Supervisor) — Chairman
Professor, Department of Electrical and Electronic Engineering,
Islamic University of Technology (IUT), Gazipur.

Dr. Md. Ruhul Amin — Member (Ex-Officio)
Professor and Head, Department of Electrical and Electronic Engineering,
Islamic University of Technology (IUT), Gazipur.

Dr. Kazi Khairul Islam — Member
Professor, Department of Electrical and Electronic Engineering,
Islamic University of Technology (IUT), Gazipur.

Dr. Md. Ashraful Hoque — Member
Professor, Department of Electrical and Electronic Engineering,
Islamic University of Technology (IUT), Gazipur.

Dr. Sheikh Kaisar Alam — Member (External)
Visiting Professor, Rutgers University, New Jersey, USA.

Dr. Muhammad Shahin Uddin — Member (External)
Professor, Department of Information and Communication Technology,
Mawlana Bhashani Science and Technology University, Tangail, Bangladesh.

Declaration of Candidate

It is hereby declared that this thesis report or any part of it has not been submitted elsewhere for the award of any Degree or Diploma.

Dr. Mohammad Rakibul Islam
Professor,
Electrical and Electronic Engineering department,
Islamic University of Technology (IUT),
Date: April 18, 2019.

Md. Taslim Reza
Student No.: 122701,
Academic Year: 2012-13,
Date: April 18, 2019.

Dedicated to my parents, wife, sister, my daughter Radyah Reza

&

all the patients suffering for cancer diseases

Table of Contents

List of Figures

List of Tables

List of Abbreviations

AMC	Amplitude Modulation Correction
ARFI	Acoustic Radiation Force Impulse
FDA	U.S. Food and Drug Administration
FEM	Finite Element Modelling
MA	Moving Average
MRI	Magnetic Resonance Imaging
ROI	Region of Interest
RF	Radio Frequency
SNR	Signal to Noise Ratio
MR	Magnetic Resonance
US	Ultrasound
FOV	Field of View

Acknowledgment

"All the praises and thanks be to the one and the only Almighty Allah (sbw)"

Firstly, I would like to express my sincere gratitude to my thesis supervisor Prof. Dr. Mohammad Rakibul Islam for his tremendous support in completing my Ph.D study, for his patience, motivation, and immense knowledge. His guidance helped me in all the time of research and writing of this thesis. Beside my supervisor, I would like to thank Dr. S. Kaisar Alam for his quality guidance, idea sharing and encouragement. I would also like to show my gratitude to my first supervisor Dr. Kazi Khairul Islam for giving me the opportunity to start my work under his supervision. I would also like to thank the Head of EEE Department of IUT, Prof. Dr. Ruhul Amin for his support in my defence. My sincere thanks to Dr. Md. Ashraful Hoque, who gave me the strength to complete my degree with eminence research outcome.

Besides the above notable people, I would like to thank the rest of my Doctoral committee, for their insightful comments, encouragement and hard questions which incented me to widen my research from various perspectives.

My sincere thanks also go to Mr. Muhammad Rezaul Hoque Khan for his continuous support and time. He enlighten me with his experience in research and helped me to organize the thesis content. I also thank to Amk Muntasir Shamim for helping me with data processing. I thank to all of my colleagues and well wishers in Islamic University of Technology (IUT) to support me during my PhD period. I would like to extend my appreciation to my beloved university IUT to give me this opportunity to pursue my PhD in IUT.

Last but not the least, I would like to thank my parents, my wife and my sister for supporting me spiritually throughout my PhD work and my life in general.

Abstract

Modulus imaging has great potential in soft-tissue characterization since it reveals intrinsic mechanical properties. The elastic properties of biological tissues are usually modified by disease. The physical quantities that describe tissue elastic properties are stress, strain and elastic moduli. Stress distribution reconstruction is vital to find out the true value of the modulus distribution. Stress distribution not only depends on the physiology of the tissue but also largely changes with the boundary conditions. In clinical practice it is impossible to find out in-depth information about the stress distribution of the tissue. Stress distribution only can predict based on different parameters. In this dissertation stress distribution is predicted from the strain distribution and stress value on the top surface of the tissue body. For predicting the first stress distribution the difference of strain distributions and the top surface stresses are taken as the references. The stress distribution prediction is updated by addressing the error of the predicting strain values. Simulation is carried out for different aspects of the tissue background and the inclusion. The proposed concept is validated with the recent algorithm by the simulation data first then comparing with the recently published data. The modulus prediction error is around 4% to 5.5% comparing with the real modulus value. Researchers in this field show the inclusion to background modulus mean error as 6.87% for a particular phantom whereas the proposed algorithm found the mean error 4.69% for the same kind of phantoms. The overall stress prediction will improve the modulus prediction which refers to good quality modulus image. Clinically it will provide detail information about the modulus spectrum.

Chapter 1

Introduction

1.1 Introduction

Medical imaging is vital to modern clinical practice, enabling clinicians to examine tissues inside the human body non-invasively. Its value depends on accuracy, resolution, and the imaged property (e.g., density). Various new scanning techniques are aimed at producing elasticity images related to mechanical properties (e.g., density, stiffness) to which conventional forms of ultrasound, X-ray and magnetic resonance imaging are insensitive. Elastography, palpography or strain imaging has been under development for almost two decades. Elasticity images are produced by estimating and analyzing quasistatic deformations that occur between the acquisitions of multiple ultrasound images. Likely applications include improved diagnosis of breast cancer (which often presents as a stiff lump), but the technique can be unreliable and difficult to perform. Previously the imaging was based on freehand scanning, i.e., the ultrasound probe was moved manually over the surface of the tissue. This requires that elasticity images are calculated fast to provide a live display, and the images need to present meaningful elasticity data despite the poorly controlled properties of the deformations.

This thesis presents technical developments towards improved clinically used elasticity imaging. First, the simulation model is proposed for complex breast structure. Based on that complex structure and practical environment all the simulation is carried out. Upper surface pressure is taken into account to predict final Young's Modulus (mentioned as modulus), which is the main objective of this thesis. Secondly, for predicting stress value, different algorithm is checked and finally a novel technique from computational time consumption point of view and modulus prediction accuracy is proposed. Mentioned algorithm is validated for two phantom structures from recent research article by S.R. Mousavi $et. el.$ [2]. Pressure acquisition system attached with US probe is proposed for surface pressure measurement. In the clinical practice a large number of elasticity images are formed for a single patient. Among them most of the image frames are not clearly visible. In this dissertation a novel approach is proposed

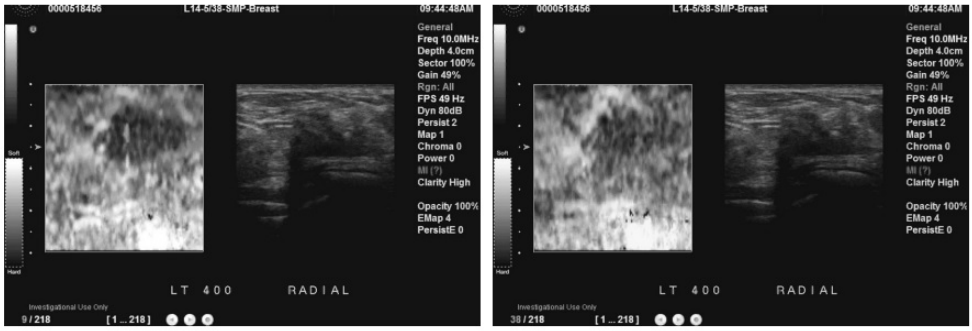

Figure 1.1: Side-by-side comparison of an ultrasound B-mode image with the corresponding elastogram of an excised uterus from a 51-year-old patient. The width of the B-mode image is 5 cm. The location of the fibroid is indicated by the arrow [3].

to find out the most visible image frames among the all the generated elasticity image frames.

1.2 Significance of the Research

An imaging technique for breast cancer detection employs tissue stiffness as contrast mechanism. When the acoustic characteristics of the inclusion and the background tissue are very close to each other then B-mode image suffers to provide clear idea about the tumor tissue. B-mode imaging suffers from this phenomena for various kind of malignant tumors. Here comes the importance to study elasticity imaging. Changes in tissue elasticity are generally correlated with pathological phenomena. Many cancers, such as scirrhous carcinoma of the breast, appear as extremely hard nodules which are a result of increased stromal density. Other diseases involve fatty and/or collagenous deposits which increase or decrease tissue elasticity. Complicated fluid filled cysts could be invisible in standard ultrasound examinations, yet be quite softer than the embedding tissue. In many cases, the small size of a pathological lesion and/or its location deep in the body preclude its detection and evaluation. Moreover, the lesion may or may not possess acoustic backscatter properties which would make it ultrasonically detectable. Diffuse diseases such as cirrhosis of the liver are known to significantly reduce the elasticity of the liver, yet they appear normal in conventional ultrasound examinations [3].

It is founded on the fact that alterations in breast tissue stiffness are frequently associated with pathology [4], [5]. This was demonstrated by stiffness measurement studies of ex vivo breast tissue samples conducted by Krouskop $et\ al.$ [6] and Samani and Plewes [7, 8]. Based on their measurements, there is a significant difference between the Young's moduli of breast tumor and healthy breast tissues. As such, imaging the variation of breast tissue stiffness due to the malignancy can be potentially used as a non-invasive breast cancer diagnosis method with a high efficacy. After develop-

ment of elastography techniques [9], breast elastography was introduced as one of the first reported clinical applications developed based on the elastography concept. Two alternative methods of quasi-static and harmonic elastography were proposed. In the quasi-static methods, the tissue is mechanically stimulated very slowly and the resulting tissue deformation data are acquired using imaging modalities such as MR or ultrasound (US). In harmonic elastography, a mechanical wave is induced in the tissue and either vibration amplitude or wave speed is measured using MRI or US imaging techniques. In both cases, acquired data is used to estimate the tissue mechanical properties (e.g., Young's modulus).

Several feasibility studies [10, 11] aiming at breast cancer diagnosis which involved harmonic US elastography were reported. Among relevant groups, Sinkus $et\ al.$ [12, 13] and Van Houten $et\ al.$ [14] proposed harmonic MR elastography techniques to measure the viscoelastic shear properties of in vivo breast lesions. While harmonic elastography techniques provide information related to tissue viscosity properties that may potentially carry more diagnostic information to characterize a breast lesion, they usually require additional hardware attachments for wave generation in addition to ad hoc software including specialized pulse sequences for MR elastography. These techniques also involve approximations which lead to elastic modulus reconstruction formulation based on the wave form and propagation characteristics. Other groups developed quasistatic elastography methods in the form of mechanical imaging [15], strain imaging [16, 17] and full inversion techniques [18, 19] for breast cancer diagnosis. In mechanical imaging [15], mechanical parameters of the breast lesions were estimated using contact stress patterns on breast surface measured through a force sensor array pressed against the breast. This imaging approach is based on the premise that temporal and spatial changes in the stress pattern allow detection of internal structures with different elastic properties and assessing their geometrical characteristics. Strain imaging is based on a simplifying assumption of uniform tissue stress distribution under which tissue stiffness is proportional to its strain reciprocal. Since stress spatial variation developed within the breast tissue during mechanical stimulation is far from uniform, strain imaging does not provide reliable quantitative tissue stiffness information necessary for high sensitivity and specificity in breast cancer diagnosis. Full-inversion based elastography techniques on the other hand, account for tissue stress variation, permitting reconstruction of quantitative maps of elasticity modulus. One difficulty with inversion based quasi-static elastography methods is that they are computationally intensive, unstable and hard to implement. To reduce the complexity of the elastography inversion algorithms, Samani $et.\ al.$ [20] developed a MR-based iterative inversion algorithm for breast elastography. This technique was later implemented based on an ultrasound platform [21] as a step to develop near real-time, low

cost and widely available imaging system. The algorithm was shown to be robust, however, it requires image segmentation for healthy and tumor tissue delineation. This requirement is not easy to fulfill, especially with US imaging.

In this research, the proposed methodology is shown for unconstrained full inversion-based breast elastography considering the surface pressure of the top surface of the field of view (FOV). In this work, it is also shown that, to predict the proper stress distribution throughout the experimental object, the surface pressure data guide to get the modulus distribution for more precise and take less computational time which give the real advantage to get more accurate quantitative modulus distribution and the characteristics of the tumor.

1.3 Research Challenges and Objectives

Imaging internal soft tissue displacements and strains resulting from mechanical forces applied to the body surface is rapidly developing into a new diagnostic modality [22, 23]. Internal deformational images, however, emphasize both the spatial distribution of the Young's or shear modulus and global boundary conditions, including mechanical constraint of the body, its geometry, the types of external and internal forces, etc. That is, displacement and/or strain images may exhibit significant artifacts due to global boundary conditions, as discussed in [20, 21]. It is challenging to reduce artifacts in elasticity images significantly by directly reconstructing and imaging the elastic Young's modulus. Although absolute quantitation may ultimately be important for certain applications, differential diagnosis based on tissue elasticity will probably be based on relative modulus reconstruction. Computing the mechanical properties of a medium based on its response to mechanical action can be posed in a number of ways. Because of physical limitations inherent in measuring internal displacements with an ultrasound imaging system, (i.e. limitations of traditional longitudinal speckle tracking algorithms for large absolute displacements and the poor accuracy of lateral displacement measurements), work to date has focused on estimating elastic moduli with limited deformation information [14, 20, 21, 24, 25]. Based on simplified models of both the elastic modulus distribution in the body and the mechanical boundary conditions, these methods are accurate only in limited applications or, otherwise, produce large artifacts in the elasticity reconstruction [21]. Consequently, expanded reconstruction methods are needed to handle more complex objects and boundary conditions.

Motivated by the issues relating to the modulus reconstruction and elasticity imaging the objectives of the current research is defined as follows:

- To develop a simulated model of a section of the breast tissue with the inclusion, which refers to the practical physiology of breast.

- To validate the simulated tissue model by comparing reconstructed modulus value using commonly used methods.
- To develop an algorithm to reconstruct modulus based on actual strain distribution of the tissue plane and only the surface stress data, which will help to generate enhanced elastography images.
- To develop an algorithm to identify the eminence image frames from a large number of elastography image frames for making the diagnostic process more faster and reliable.
- To verify the proposed approaches with the recently published data.

1.4 Main contributions

Based on the research challenges and objectives mentioned above, this dissertation provides main contributions listed below:

- A practical simulated model of the breast with the tumor is developed which provides a practical complex environment in the modulus reconstruction algorithm.
- A stress spectrum updating process is proposed and the effectiveness based on the window size of the stress vector is shown.
- A novel modulus reconstruction algorithm is proposed and compared with the classical method where the surface stress is not taken as the input data. The mean error rate is calculated for both cases. For the proposed algorithm, surface stress and the strain data is taken as the input data.
- The proposed reconstruction algorithm is applied for different conditions of the inclusion.
- The proposed reconstruction algorithm is validated by comparing with the recently published article.
- A semi-automated best frame selection algorithm is proposed to find some significant image frame from the strain image sequence and validate by human visual perception.

1.5 Thesis outline

Subject to the above research objectives and targeted contributions this dissertation is outlined as follows:

Chapter 1 provides the background and motivation of the current research including main contributions and significance of the research. Later, the thesis outline is presented at the end of this chapter.

Chapter 2 focuses on contemporary literature survey related to quasistatic imaging and modulus reconstruction algorithm. This chapter also discusses the theoretical and research aspects of the relevant current works.

Chapter 3 presents the algorithm to predict the modulus by inverse method considering only the surface stress and the displacement distribution from pre and post compression US data. A relevant simulated tissue structure with skin, fat, inclusion and background tissue is designed and validated. The challenges of the proposed algorithm is discussed and the solution is presented in this chapter. Various cases are considered to validate the real life scenario.

Chapter 4 concentrates on the result, analysis and validation. A number of practical cases are considered and for all the cases the simulations are done. All the results are presented and analysis is carried out after the result. Validation of the proposed algorithm is made by comparing with stranded and recently published research data.

Chapter 5 presents the algorithm to find out the best frame from the image sequences of the strain image. It can also be implemented in the actual elasticity imaging sequence for efficient image selection. The result is also presented at the last part of this chapter.

Chapter 6 provides the concluding remarks and future directives for this research. The future work is also presented to get better output from the proposed approach.

Chapter 2

Literature Review

2.1 Introduction

Modern medical practitioners have the opportunity to acquire the important information in a continual basis by the haptic properties of tissue . Developing countries have invested enormously at research and infrastructure for breast screening programs. Irrespective of the steps towards evidence based medicine, researchers are focusing on the measurement of tangible changes in medical outcomes. Manual palpation in clinical breast examination is still widely believed as a vital procedure, contributing towards reducing the breast cancer mortality rate [5]. On the other side, breast cancer elucidates the bindings of subjective examinations when the apparatus may not be adequate [4]. It was presumed that training woman in self-examination of their own breast could unlock better medical results, owing to previous cancer detection, but the conglomerated attestation indicates that such training programmes have only one remarkable outcome. The Rate of biopsies on benign lesions increases, which may be damaging to health [5].

Among females, breast cancer is the most commonly diagnosed cancer and the leading cause of cancer death, followed by colorectal and lung cancer (for incidence), and vice versa (for mortality); cervical cancer ranks fourth for both incidence and mortality. There will be an estimated 18.1 million new cancer cases (17.0 million excluding nonmelanoma skin cancer) and 9.6 million cancer deaths (9.5 million excluding nonmelanoma skin cancer) in 2018 [26, 27]. In both sexes combined, lung cancer is the most commonly diagnosed cancer (11.6% of the total cases) and the leading cause of cancer death (18.4% of the total cancer deaths), closely followed by female breast cancer (11.6%), prostate cancer (7.1%), and colorectal cancer (6.1%) for incidence and colorectal cancer (9.2%), stomach cancer (8.2%), and liver cancer (8.2%) for mortality. Lung cancer is the most frequent cancer and the leading cause of cancer death among males, followed by prostate and colorectal cancer (for incidence) and liver and stomach cancer (for mortality). According to estimates from the World Health Orga-

nization (WHO) in 2015, cancer is the first or second leading cause of death before age 70 years in 91 of 172 countries, and it ranks third or fourth in an additional 22 countries [28, 29].

This literature review draws extensively on the comprehensive review provided by Lindop [1]. The mechanical properties of tissue have always been considered as a notable factor for medical diagnosis in the long history of clinical practice. In The Book of Prognostics (c. 400 BC) Hippocrates stated indicating abdominal swellings that,

"Such, then, as are painful, hard, and large, indicate danger of speedy death; but such as are soft, free of pain, and yield when pressed with the finger, are more chronic than these" [22].

As noted in [1], The hindrance of manual examinations is searching for hard chunks and encourage the expansion of more updated diagnostic tools. Every form of diagnosis have a subjective component but most probably up to the minute technology will help by serving clinicians with more accurate information than is available now. For a long period physicists are holding interest in the mechanical properties of biological tissues but this complex issue cannot draw the attention for some obvious practical reason where the study of engineering materials are getting full concentration [6, 7]. There is so little tabulated data existed which would be relevant to medical diagnosis of biological tissue [8]. However, such quantitative measurements illustrates that changes in rigidity may discriminate between healthy and infected tissue in numerous circumstances [8, 9, 19, 20]. This thesis will exploit such differences with a diagnostic imaging technique and concentrate over the technical development of a practical system for generating images related to mechanical properties for freehand ultrasound scanning. This could be a beneficial approach to both 2D and 3D imaging of differing tissues which is made on the existing abstract idea of quasistatic elasticity imaging [11, 45].

This task is motivated by general medical interest in mechanical property imaging and concreate opportunities linked with quasistatic elasticity imaging which can be supported in the context of the alternatives which are being constructed elsewhere. An elaborated exordium is given which is considered to be a range of connected ultrasonic techniques, in which facile contrasts mask general principles. Some features of the gesture processing method updated for 2D and 3D elasticity imaging using ultrasound may be relevant to a scale of different imaging concepts.

To quote [1]: ‘Since the arrival of real time ultrasound in the 1980s, clinicians have been eligible to notice movement in the scans. At the time of working with image sequences, Dickinson and Hill established a mutual relationship method for measuring small motions within tissue [30]. Thereafter, multifold researchers have come up with

ultrasonic methods for assessing mechanical attributes, with broad variation the physical principles associated involved [12,21,30,31]. Each and every method is connected with the in vivo application of reversible deformations to human tissue ,so imagery techniques founded on measurement and reasoning of such elastic deformations are defined as elasticity imaging.

In the mean-time, other researchers proposed methodology using magnetic resonance imaging (MRI) [32, 33]. One of the noteworthy favorable condition of ultrasound is the relative ease of manufacturing a real time display, which empowers clinicians to scan investigatively and focus on regions of parts of interest. Generally orthodox approaches to MRI and ultrasound have relative merits and likely to continue on to elasticity imaging. Moreover ultrasound devices are less expensive and moveable. While achieving fairly isotropic image quality, MRI has the plus point of producing 3D scans of large volumes. Though ultrasound can surpass the resolution of MRI in the axial direction, the characteristic of ultrasound images are tremendously anisotropic. Methodology for processing focused ultrasound beams are called beamforming. Conventional beamforming tends to weaker resolution in the lateral and elevational direction (see Figure 2.1) [15]. Future advances may recover the non- axial resolution [16]. However there are several methodologies for accomplishing 3D ultrasonic imaging with conventional beamforming [23,34,35] . In the long run, successful techniques for elasticity imaging evolved with MRI.

Ultrasonic elasticity imaging can provides significant inlet for a wide range of clinical applications. To discover Breast imaging and diagnose cancer is a significant motivation of research and it is among the first application involved in routine clinical practice [36, 37]. Other studies have viewed diagnosis prostate cancer [38, 39], which drives analogous changes in mechanical properties. Further applications approximately emerge considering other soft tissues. By means of ultrasonic elasticity measurement, a commercial system has already been developed for classify liber fibrosis [40]. Elasticity imaging systems altered for dermatological scanning may improve skin cancer diagnosis [41, 42]; chronic dermatological conditions including scheroderma and Ehlers- Danlos syndrome are also categorized by changes in skin elasticity [43]. Various cardiovascular diseases are familiar for causing changes in mechanical properties. Elasticity imaging may recover the detection and staging of deep vein thrombosis [44], and the recognition of vulnerable plaque deposits in patients with atherosclerosis [40, 45]. Similar information would take credit in examinations of the myocardium [46, 47]. Furthermore non-diagnosis applications include monitoring the formation of thermal lesions during ablation therapy (a form of non-invasive surgery) [48, 49]. Techniques which serve real time images may also have intra-operative uses, such as ameliorating the delineation of tumor boundaries during neurosurgery [50].'

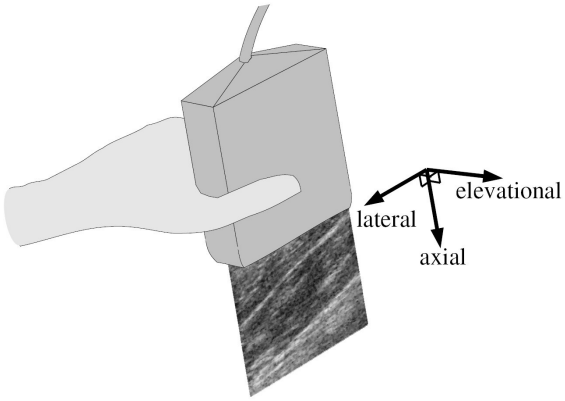

Figure 2.1: Naming convention for three orthogonal directions relative to an ultrasound probe. The "axial" direction is normal to the face of the probe (vertical in a 2D ultrasound image), and the "lateral" direction is parallel to the transducer array (horizontal in a 2D ultrasound image). These are both orthogonal to the "elevational" direction (out-of-plane with respect to a 2D ultrasound image). Figure reproduced by kind permission of Joel Edward Lindop [1].

2.2 Theory of Elasticity Imaging

As noted in [1], An overflowing number of formally defined mechanical properties could be accepted in the analysis of human tissue. Examples related with elastic deformations are listed in Table 2.1. There is a probability of a subset of properties for which measurements or images would be clinically fruitful, and another subset of properties for which incident measurement or imaging has some possibilities. The overlap is the type of property that may provide as the foundation for successful elasticity imaging. An overview of relative theory is presented, framing the role of qualitative approaches to elasticity imaging.

When researching ultrasound image to illustrate mechanical properties, deformation motion is required, i.e., compression, expansion or shear. A field of displacement data has defined in the simplest manner about the recording tissue motion as a function of spatial position. A more useful elaboration is in terms of strain, i.e., quantities measured by taking spatial derivatives of the displacement of the field to vanish components connected with rigid body motion (bulk translation and rotation) which are irrelevant to mechanical properties.

In 1D, strain is typically illustrated as the change in length divided by the original length [6]. Definition differs noticeably when the large strains arrive (e.g. greater than 10%). Various definitions are appropriate for 3D analysis, where the most popular is also simplest, and they converge when considering small deformation. Throughout the thesis, strain means elements from Cauchys strain tensor.

To quote [1]: ‘Generally in 1D, strain is determined as the change in length divided by either the original or the final length [6]. Large strains, which is greater than 10%,

Table 2.1: Examples of formally defined mechanical properties. Table reproduced by kind permission of Joel Edward Lindop [1].

Categories	Names	Symbols	Descriptions
Linear elasticity [7, 51]	Elastic modulus tensor	C_{ijkl}	A $3 \times 3 \times 3 \times 3$ matrix with up to 21 independent coefficients, describing 3D linear-elastic behavior of anisotropic materials.
	Lame coefficients	μ, λ	Often used in physics, these coefficients describe isotropic linear elasticity.
	Shear modulus, bulk modulus	G(G=μ), K	Referred to in engineering; an equivalent description of isotropic linear elasticity.
	Young's modulus, Poisson's ratio	E, v	An equivalent description with appeal to intuitive understanding.
1D linear viscoelasticity [7, 51, 52]	Creep compliance, relaxation modulus	$J(t), Y(t)$	Functions of time indicating strain and stress responses to step changes in stress and strain respectively.
	Complex compliance	$G_1(\omega) + jG_1(\omega)$	A complex representation indicating the magnitude and phase of strain divided by stress as a function of frequency in tissue subject to harmonic loading.
Linear isotropic poroelasticity [53, 54]	Young's modulus, Poisson's ratio, permeability	E_s, ν_s, κ	The Kwan-Lai-Mow biphasic model of porous media: these parameters describe an isotropic linear-elastic matrix saturated with fluid.

make a significant difference in the definition. Several definitions are favorable for 3D analysis. One of the most popular definition is the simplest, and they converge when accepting small deformations. Throughout this thesis, "strain" means elements from Cauchys strain tensor:

$$\varepsilon_{ij} = \frac{1}{2}\left(\frac{\partial u_i}{\partial x_j} + \frac{\partial u_j}{\partial x_i}\right), \qquad i, j = 1, 2, 3..... \tag{2.1}$$

Where u_i is displacement in direction i, and x_j is pre-deformation position in direction j. The different meanings of longitudinal and shear strain are indicated in Figure 2.2.

Strain arises for the changes in the stress field (force per unit area) within the tissue, and this in turn go behind changes in forces acting internally or no bounds defines as mechanical excitation. The tissue may pressed by a compression plate [22], vibrated from its surface [55], bumped on the surface by a small mass [21], or palpated internally by using the radiation pressure [56] (see Section 2.3.2) the resulting stress consist of (1) an isotropic or hydrostatic component which causes change in volume (change in pressure), and (2) anisotropic components which causes change of shape (shear

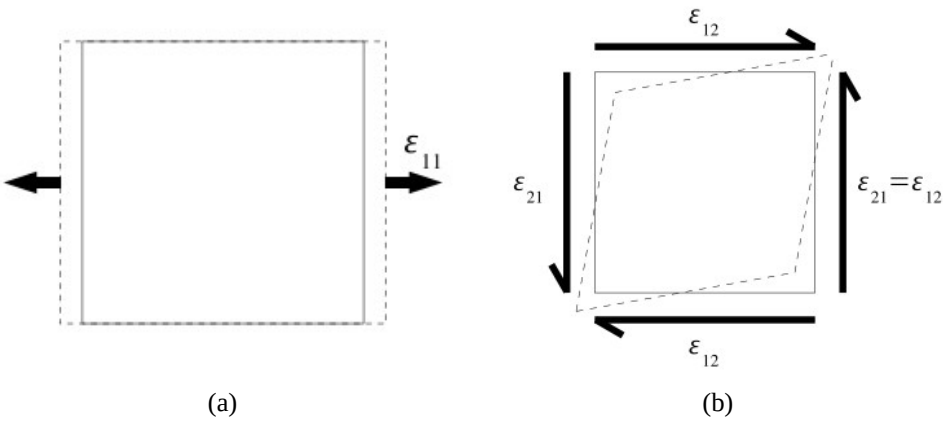

Figure 2.2: Components of 2D strain, (a) Longitudinal strain and (b) Shear strain. Figure reproduced by kind permission of Joel Edward Lindop [1].

stresses and anisotropic components of longitudinal stresses). Components from 3D stress tensor are classified in Figure 2.3.

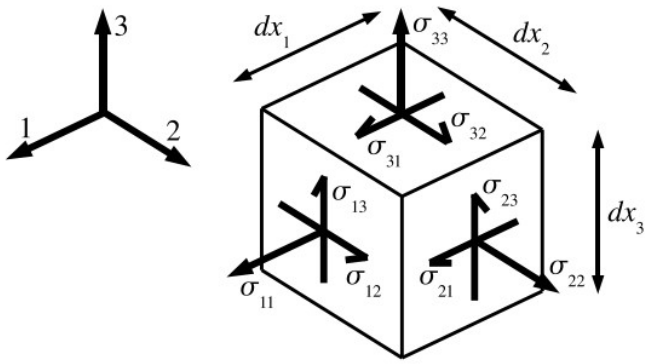

Figure 2.3: Elements from the 3D stress tensor labelled on an infinitesimally small cube. Force components acting on the surface of a finite object can be found by integration, e.g.,$dF_1 1 = \sigma_1 1 dx_2 dx_3$. Strains with matching subscripts (not labelled above) indicate matching deformations, so the tissue has stretched over direction 1 if ε_{11} is positive, while a positive value of ε_{23} indicates warping in the 2-3 plane along the lines of Figure 2.2(b). Figure reproduced by kind permission of Joel Edward Lindop [1].

For estimating mechanical properties, measurements or assumed calculation of deformation have to be merged with prior knowledge, estimates or reasonable predictions regarding mechanical excitation. In accordance to the theory, deformation and excitation are connected through constitutive equations contingent on mechanical properties of the tissue. For example the theory of linear elasticity founded on Hooks law has been developed by mathematicians, physicians and engineers. It is proven to be beneficial for analyzing the properties of man-made construction as buildings and machines [51]. Much of the characteristics of general engineering materials, such as steel and timber, is actually poorly illustrated by linear elasticity, but the theory is precious because

engineers are acquainted with circumstance in which it applies relatively accurately [57].

If there is any requirement for manufacturing quantitative images of a particular mechanical property by solving an inverse problem, one of the major challenges is the demand for accurate deformation measurements and it is considered at length in all the term of the thesis. Basically, computational cost is also a notable issue, i.e. the time which is required to produce each image and the quantity of computing power that have to be constructed into the ultrasound scanner. Both reflections execute similarly with the accordance of producing images which are related to mechanical properties qualitatively.

Three other fundamental challenges are presented by quantitative imaging: (1) Complexity: approximately this is the greatest hindrance. The mechanical deportment of tissue is not strictly narrated by simple, convenient models [6]. (2) Computational stability: the increasing number of parameters diminishes the availability of the chance of a unique solution, in the mean-time the quantity of data which is mandatory for achieving acceptably low error boosts drastically [58]. (3) Unknown boundary conditions: basically elasticity imaging is based on scanning a limited area of tissue, spanning a low volume (3D scans not encircled the entire human body) or a slide (2D scans). This creates problem, because some approaches to quantitative analysis only produce the accurate solutions if the mechanical properties are known all over the boundary [59].

$$\sigma_{ij} = \sum_{k} \sum_{l} C_{ijkl} \varepsilon_{kl} \qquad i, j, k, l = 1, 2, 3..... \tag{2.2}$$

where σ is the stress tensor, C is the elastic modulus tensor, and e is the strain tensor. Symbols i, j, k and l denote the three spatial dimensions. Stresses and strains are longitudinal where $i = j$ or $k = l$, while shear stresses and shear strains have subscripts $i \neq j$ or $k \neq l$. The mechanical properties described by C may vary throughout the tissue. Equation 2.2 can be used to find out the stress and strain fields throughout an area with known C subject to known boundary forces. Calculating strain fields based on trial sets of mechanical properties and boundary forces can handle the inverse problem. Likely parameter sets are spotted by predicting the degree of correspondence between the estimated and measured strain fields. Generally the identification of approximate parameter sets is also instructed prior prophecy regarding their connected plausibility [58]. Adapting the most probable solution, coefficients in C can be charted to pixel values in quantitative elasticity images.

This example is determined to point out the value of circumspection when determining how to analyze mechanical properties for elasticity imaging. As linear elastic

theory enables acquainted linear algebra techniques, it is accepted logically [60], at the time of agreeing the probability of real tissue being highly anisotropic. The mechanical properties of every piece of tissue are elaborated in C by 21 independent coefficients [51].consequently, static analysis demands reasonably exact prediction regarding the 21-dimentional mechanical properties over the circumference otherwise most of the model is redundant. Concerning computational cohesion, a single still deformation measured with perfect idea of the boundary conditions and perfect estimations of every strain elements throughout the scan region is not suffice to yield a unique solution. Any determined solution relies on prior prediction [58]. It can be possible specify distinctive maximum likelihood solution which is independent of prior to knowledge, if various deformations are judged together. Whatever, the inverse problem may remain in a poor condition; the most favorable solution may contain huge errors even for data that are almost free of noise [60]. Previous knowledge stays significant for enforcing a credible solution.

Linear elastic analysis may nevertheless accepted as a reliable approach to elasticity imaging. Prior knowledge for practical analysis could embrace prediction of dependent connectivity between some of the coefficients in C so as to diminish the dimensionality of the difficulty. There is a little point in acclimating a highly complex linear elastic model if there is any chance of tissue nonlinearity bounds its validity, and the effects which are time dependent in the loading response bring up further errors.

An assorted range of coefficients can be measured to describe tissue characteristics for analyzing ex-vivo samples [6, 7] but inclusive characterization of mechanical property is different from a practical basis for elasticity imaging. The analysis needs to concentrate on salient properties of interest to clinicians, considering that disregarded properties may contribute to errors and artefact.

Fundamental biophysics encourages a range of techniques. Soft tissues in the human bodies are difficult composites. They are composed mostly of fluid filled sacks (cells), which are almost incompressible, i.e. the volume here is static, but cells presents almost no resistance to shear [6]. An extra-cellular networks of fiber provides structural integrity, of which there are various types. Elastin demonstrates highly linear characteristic but is only an insignificant constituent accept in the skin and vasculature. The most noteworthy structural material is collagen, which is made of long, helical, covalently-bonded protein molecules, twisted like rope. This is too much complicated to analyze. The micro structure of the fiber network recognizes its macroscopic properties and these are usually anisotropic and nonlinear [8]. Abrasion associated with reorganization of fibers contributed to atrocious behavior in most biological materials. When writing, it feels sensitive to make fairly basic estimations so as to understand practical imaging techniques, while the progression of convenient models that more

precisely characterize the mechanical properties of tissue is an advanced research topic [7]. A small of elasticity imaging notion give priority to the value of measuring viscous behavior. Stress in viscoelastic tissue relies on the rate of deformation and size. This is assumed to be a notable in the behavior of all oft tissues [6]. It has been supported that measurements of viscoelastic time constants would connect to biochemical changes, either giving information or impassable by ultrasonic methods [61]. Though this is an interesting concept, viscoelastic modelling is extremely convoluted. Even 1D theory places no boundary on the number of parameters that may be necessitated for an accurate elaboration of loading responses over time, relying on which type of linear model nearly matches the tissue behavior [6, 52]. Researchers in ultrasound [62] and MRI [63] preferred that the simplest viscoelastic model (the Kelvin- Voigt solid [52], which is rather unlike tissue [6] can be implemented where viscosity would otherwise be neglected or for improving the precision of quantitative images delineating other elastic moduli. Although the escalation in accuracy has not measured, this sort of development might be useful.

A more relatable application of viscoelastic analysis is poroelasticity imaging. Hardly the fluid in the tissue can free to flow, except in vessels. It can do so in case of oedema, where fluid collects and causes the swelling progression. Fluid flow which is correlated with elevated porosity can be presumed qualitatively utilizing images founded on the changes in non-axial over period in tissue to an unchangeable load [58, 62]. It should be possible to excerpt meaningful assumption of parameters to describe poroelastic behavior quantitatively and it is also assumed that the tissue consist of a solid, isotropic , linear elastic matrix, imbued with compressible , near inviscid fluid, which is recognized by a permeability coefficient that connects pressure gradients for flowing rates [54]. (see table 2.1). If or not development is made towards quantitative poroeladticity imaging [59], primarily studies propose that the qualitative images can be useful in themselves for presuming oedematous tissue [64, 65].

On the other hand, the most general basis for elasticity imaging is a facilitation that neglects the viscosity. Most noticeable differences between hard and soft tissues have long been discovered by touch through manual palpation. It is predicted that elasticity imaging techniques which are aspiring the same physical property may co-operate by offering superior accuracy and/or spatial resolution. The mechanical properties of tissues are diminished to a single parameter by hypothecating the characteristics to be isotropic, linear-elastic, inviscid and incompressible.

Can these estimation be justified? At first while tissue is hardly isotropic, the chance for condensing more information by adding to the model complicacy may be bounded, as the mechanical properties in a single direction influences deformations mainly. Secondly, tissue feature is highly nonlinear under large deformations but any

deformations can be linearized if it is small enough. There are three common methods of expressing the predicted constitutive equation under equilibrium condition [51].

$$\sigma_{ij} = \begin{cases} \lambda \sum_k \varepsilon_{kk} + 2\mu\varepsilon_{ij} & if\ i = j, \\ 2\mu\varepsilon_{ij} & otherwise \end{cases} \tag{2.3}$$

$$= \begin{cases} K \sum_k \varepsilon_{kk} + 2G\left(\varepsilon_{ij} - \frac{1}{3}\sum_k \varepsilon_{kk}\right) & if\ i = j, \\ 2G\varepsilon_{ij} & otherwise \end{cases} \tag{2.4}$$

$$= \begin{cases} \frac{E}{1+v}\left(\varepsilon_{ij} + \frac{v}{1+2v}\sum_k \varepsilon_{kk}\right) & if\ i = j, \\ \frac{E}{1+v}\varepsilon_{ij} & otherwise \end{cases} \tag{2.5}$$

(λ, μ), (K, G) and (E, v) are the parameter pairs associated with each formulation (see Table 2.1) Equation (2.3) is the most elegant mathematical expression, but Equation (2.4) is easier to explain. Change in volume multiplied by K gives the isotropic component of stress, and anisotropic components of strain multiplied by $2G$ give anisotropic stress components. The parameters in Equation (2.5) are also widely referred to, despite the cumbersome $3D$ formulation. (For uniaxial stress, E is the ratio between axial stress and strain, while v is the ratio between non-axial and axial strain.) In any event, these formulations are equivalent. Each parameterization separates components of elastic behavior in a useful way if tissue is assumed to be incompressible. This would be an unreasonable assumption for porous tissue, as discussed above, but it applies fairly accurately in most healthy tissue, provided that fluid channels such as blood vessels and lymph ducts are not a large fraction of the tissue volume. This fixes one of the elasticity parameters ($\lambda \simeq 8, K \simeq 8$, or $v = 0.5$), so the remaining parameter (μ, G, or E) fully characterizes any variation. These formulations are same at any situation. If tissue cannot be compressed each parameterization distinguishes of the compounds of elastic behaviour in an efficient way. As stated above this would be an incomprehensible assumption for porous tissue but it applies properly in most healthy tissue. Under the condition that fluid channels for example blood vessels and lymph ducts are not a large portion of the tissue volume. This settle down one of the elasticity parameters, so any changes are fully characterized by the remaining parameter. A suggestion is that, this accounts almost fully for the useful information perceived by manual palpation [10, 66]. It is probable to apply a little load to a region of tissue, Calculate the deformation, explain the strain pattern to detect any changes in the shear modulas, G, or young's modulas, E. Many factors lend obscurity to this, not the least

of which is viscosity.

Equation (2.3) concerns static load, on the other hand in reality all kinds of loads are partially dynamic. If the loading rate is too much high, viscous damping may have sufficient impact or if static loads are applied for a longer period(minutes or hours) viscous creep may be sufficient [6]. Dynamic effects are insignificant at a "quasistatic" loading rate which is somewhere between those extremes, hence "quasistatic" elasticity imaging. In alternate order, by measuring and analyzing dynamic behavior, tissue elasticity can be investigated. If viscous effect are not important, the reason behind the difference between quasistatic and dynamic behavior is inertia. Newton's second law of motion gives the followings with the assumptions of isotropic linear elasticity [51].

$$\rho\frac{\partial^2 u}{\partial t^2} = \left(K + \frac{4}{3}G\right) \bigtriangledown (\bigtriangledown . u) - G \bigtriangledown \times \bigtriangledown \times u, \tag{2.6}$$

$$c_p = \sqrt{\frac{K + \frac{4}{3}G}{\rho}}, \qquad \text{and} \quad c_s = \sqrt{\frac{G}{\rho}}. \tag{2.7}$$

The amplitude of pressure waves in the ultrasonic frequency range which is reflected back from inhomogeneities in soft tissue is showed by the usual ultrasound images (B-scans). As K and ρ are most of the time constant to a great extent, so c_p , the speed of sound exhibits little variation. After a pressure pulse has been sent from the ultrasound probe into the tissue, the depth of a reflector can be thought proportional to the incoming time of its echo. If the speed of sound alters, all kinds of composition of ultrasound pictures are perverted, although minor distortion can be corrected by using some opportunities [66].

To give entry of the improvement of shear waves which is propagating through the tissue, its possible to gain raw ultrasound data rapidly when c is constant. As K is very large, the assumption of soft tissue being incompressible implies $c_p \gg c_s$. For instance, in fat the wavespeed of pressure is at large 1000 times greater than the wavespeed of shear [67]. According to the assumed fact, the time taken for a shear wave to propagate over the length of a picture can acquire up to 500 B-scans. Consequently, it is possible to testament ultrasonic methods for calculating shear wavespeed and it is concerned with the shear modulus by Equation (2.5). Practically, while viscosity makes minor or partial changes to the wavespeed and causes attenuation, nonlinearity corrupts the shear waveform. Nonetheless, information provided by effective calculation of shear wavespeed will have great clinical value with considerable certainty.'

2.3 Concepts of Elasticity imaging

Though the following review is not representing the entire factors, but it should provide as a significant context to judge the effectiveness of the approach followed in this thesis. Quasistatic, dynamic (continuous), dynamic (transient) are the three categories based on the time dependency of mechanical excitation which are considered to summarize the main ultrasonic concepts and to highlight the differences [68].

2.3.1 Quasistatic

The basic scanning method consists of (1) recording a "pre-deformation" ultrasound image of unloaded tissue (2) applying a load (3) recording a "post-deformation" ultrasound image. A suitable single processing technique estimates the deformation between pre- and post- differentiation ultrasound frames and analyses to generate an elasticity image.

As mentioned in [1], loading can be implemented at a quasistatic rate by various means. For instance, research into itravascular elasticity imaging utilizes psychological excitation : change in blood pressure over the cardiac cycle causes artery walls deform [69]. The frequency of the loading is approximately 1Hz and it seems compatible for quasistatic analysis. In terms of other tissues, breathing is the reason behind quasistatic deformation.

Several investigation have been executed, by the use of the ultrasound probe as the source of quasistatic mechanical excitation. To quote [1]: 'When the probe is pushed steadily against the surface the tissue is compressed, whereas relaxes at the time when the probe is held gently (see Figure 2.4). Suppose that motion of the ultrasound probe results a big change in the axial element of longitudinal stress. Strain at every point in the image is understood as inversely proportional to Young's modulus when the behavior is isotropic linear-elastic. Usually the stress field is nonuniform and so strain data are confusing but strain imaging is the most understandable path of showing quasistatic deformation data for providing a visual inkling of variation in mechanical properties. Techniques which are exploiting probe movement for mechanical excitation can be differentiated into two subcategories. Automated scanning requires additional hardware [22, 36], where freehand scanning is the common technique applied in conventional sonography [10, 38, 70]. The selection of significant scanning technique has noteworthy consequences.

Deforming tissue by means of a carefully defined movement at the surface , automated scanning involves necessary consequences mounting an ultrasound probe on a mechanical actuator .For example, tissue can be flatten by pressure by translating the probe accurately 1 mm in the axial direction [22,36,71]. The prime opportunity is that

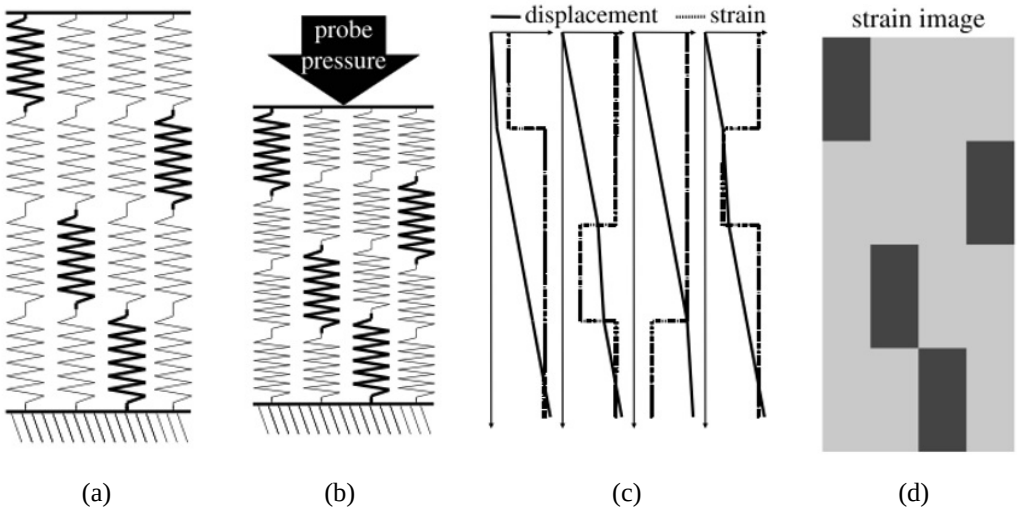

Figure 2.4: The principle behind quasistatic elasticity imaging [5]. Figure reproduced by kind permission of Joel Edward Lindop [1].

a certain probe movement is repeatable specially if it is defined to lead to clear elasticity images in a specific application. Moreover, the depended acquisition of appropriate pre and post deformation ultrasound data explains that computation for manufacturing an elasticity image can be performed off line. Probably this take time for lengthy computational methodology to maximize the quality of the elasticity images.

Figure 2.4(a) demonstrates inhomogeneous tissue modelled as a set of springs, where various spring constants symbolize diversification in Young's modulus. The rest are three times less stiffer than bold springs. The pre deformation state of the tissue are recorded by an ultrasound images. Figure 2.4 (b) describes the tissue deformation when the ultrasound is pressed dynamically against the surface, and a post deformation ultrasound image is documented .The deformation here is overvalued for illustrative purpose (25% compressive strain). While examining human tissue, it is likely that comparatively smaller deformations (strain on the order of 1%) are more relevant. Figure 2.4(c) illustrates the tissue deformation related to the ultrasound probe is illustrated by analyzing the ultrasound images and strain is calculated by differentiation.

If the stress throughout the tissue is constant (as in this example), strain is oppositely part of the spring constant and so the strain in hard spring is three times lower than anywhere else. By setting pixel intensities as stated by the strain values which is presented in the figure 2.4(b) reveals the diversification in the spring constant.

Equally, the demand for correct prior idea of the probe movement is potentially a hindrance. The transcendent movement for quasistatic elasticity imaging is varying from one patient to another. Automated scanning is clunky in comparison to the freehand approach that clinicians are used to. Normally the sonographer grips an ul-

trasound probe in his or her hand and change the position manually over the patients skin to make images of approachable tissue from whichever angle illustrates to be the most visible [38, 70]. There is certainly some difference in the pressure implemented through the probe between the sequential ultrasound frames in a freehand scan [72], which is a cradle of continuous mechanical excitation.

As it can potentially be applied on conventional ultrasound machines with negligible modification to the hardware and scanning procedure, the free hand scanning methodology is highly charming. When it is needed in the time of routine sonography elasticity imaging could be made accessible as a display option to switch on anytime. Such an evolution might mirror the prior adoption of Doppler techniques for measuring blood flow [73, 74], which has hastily become an essential accessory to conventional ultrasound imaging [15].

In comparison to automated scanning, the distortion in a freehand scan is significant and unpredictable. Probably clinicians are not eligible to perform prescribed probe movements precisely on a very high scale. For this, freehand deformation may often be very low or high for inferring mechanical properties or the variety of deformation may simply be unacceptable. Figure (2.4) demonstrates axial probe movementby which the compression is created. Freehand scanning is determined to throw up more difficult movements such as rotation about the rising axis. Some freehand strain images are extremely less informative than automated strain images. On the other hand, a chronological sequence of freehand strain images can examine a range of deformation, so the best freehand images may be more visible than the best automated strain images [70]. Moreover, the variation within a process of freehand deformation could rise the dependence of inferences related to the mechanical properties. The value of a strain image consequence must rely on the sonographers scanning technique. A live strain play provides continual feedback to improve the usefulness freehand scanning significantly, so the scanning tactics of sonographer can be adjusted by him/her towards what seems to work best [70]. Live strain displays have been exhibited in the former period rates as the same as conventional ultrasound imaging (some tens of Hz) [10, 75]. The geometry of regions distinguished by the mechanical properties of Quasistatic elasticity imaging may be exhibited in fine detail, whether through automated or freehand scanning. However, the effectiveness of the images will rely on how perfectly deformation can be calculated using ultrasound, and how closely inferences relying on the deformity calculates can be made to correspond to quantitative mechanical properties of the tissue such as Young's modulas.

When estimating strain or inferring mechanical properties and when tends to amplify noise, raw displacement are spatially differentiated which is critical. By implementing larger deformation, the signal strength can be enhanced but the deformations

that are large, are unlikely to be desirable. As discussed in section 2.2, the response is more nonlinear and also more troublesome to interpret exception of the basic issue of patient comfort. That is to say, a notable deformations may not enhance the signal-to-noise ratio, As a rise in the "deformation signal" results in greater decorrelation between successive ultrasound frames, which as a result increase the level of estimation noise [76]. This topic is considered thoroughly in this thesis. Although there may be no simple means of assuring that all deformation calculates are properly accurate, the feasibility of properly calculating tissue deformation using ultrasound data is a fundamental premise behind this work.

On the second point, strain images along the lines of Figure 2.4(d) are not identical to Young's modulus images that are meant by nonuniformity while it is in the stress field, can strain data be transformed into Young's modulus images? The assumption of isotropic, incompressible, linear-elastic behavior introduced in section 2.2 greatly simplified the inverse problem. If the stresses or Young's moduli are known at all points over the scan boundary then it is possible to calculate Young's moduli in the entire scan region, by accepting the approximate nature of this analysis [59]. Many researchers have tried to generate quantitative images on this basis [77, 78], but boundary conditions that are not known are a significant obstacle. It is (probably) implausible to determine all of the boundary stresses, so the information is necessary about boundary values of Young's modulus. By assuming uniformity over the boundary, it has been put for consideration that images of relative Young's modulus can be generated [79, 80], but major mistakes can happen if the assumption of uniformity is not correct. The choice of proper assumption is given priority in model based approaches, which may be more fruitful for clearly identified well constrained tasks [81].

Challenges which are connected to the inverse problem will not follow the simpler approaches to quasistatic elasticity imaging. In spite of the variation in stress, strain images displays useful information. Limitations in exact strain images usually correspond to boundaries with respect to mechanical properties, though the size of differences in strain does not keep pace with the size of differences in Youngs module [82]. Strain images cant give grounds for quantitative statements such as, Youngs module in the lesion is 2.5 times higher than in the background, but it may often be having sound judgement to make qualitative observation such as, the round lesion (diameter of 3 mm) is much stiffer than the background. This point of interpretation is cleared up in Section 2.4. To date, strain imaging has come nearer to almost every clinical formal exhibition of evidence by judging of quasistatic elasticity imaging. In one instance, data were attained by automated scanning [36], but free hand scanning has been examined more frequently [39, 70] with a centre of attention on breast and prostate examinations. Sometimes successful strain images are better than established ultrasound for

pointing out tumors [39]. Malignancy and diversified cancer may be distinguishable on the basis of either strain constraint [36] or differences in geometrical appearance in between conventional ultrasound and strain images [36, 70, 83, 84]. Reports conclude collectively that strain imaging could potentially be a beneficial detached tool, but none has yet clearly showed truth of conclusive case for taking on routine clinical practice. Stress variation issue and limitations seems not to be a prime issue, as the qualitative information is still beneficial. The dubiosity of how to produce accurate images is the main problem, because strain images is persisted to be undependable [36, 70, 84]. The existence of many bad images makes assumption complicated and vigorous for sonographers who are typically required to examine sequences of stored strain images by using eye to choose those which are informative [84]. This thesis confer towards improving the dependability of the prior prediction of the stress field and hence Youngs modulus prediction.'

2.3.2 Dynamic (continuous)

Question might be asked, can better elasticity images be generated by techniques founded on continuous dynamic mechanical action? As noted in [1], normally a vibrator acts on the tissue surface, dispatch shear waves in the same frequency range similar as audible sound. Techniques with this form of actions are familiar as sonoelastic imaging. In contrast, an oscillatory force in the audible frequency range can be implemented to a small region within the tissue using high intensity focused ultrasound by which the mechanical response is calculated in vibro acoustography.

Sonoelasticity imaging

As noted in [1], adaptation of Doppler methods was introduced by Lerner and Parker et al. [85, 86]. They used it for generating vibration-amplitude pictures which show patterns of steady-state vibration in soft tissue. When there is low frequency (10-1000 Hz), vibration is applied at the surface where the amplitude is 0.1 mm. In figure 2.5(a) a typical imaging setup has been shown. For transmitting shear waves throughout the scan region, vibrators should be set at suitable locations. Figure 2.6 is there for further clarification. Rigid inclusions in soft tissues appears as dark portion of low vibration amplitude. Two reasons can be identified for this. Firstly, a continuous travelling wave of a given intensity possess lower amplitude within an inclusion of high shear modulus. Secondly, reflections at inclusion boundaries intensifies the deviation in vibration amplitude. In this process, while the background energy level is slightly increased, reduction of the wave energy entering the inclusion is used.

Sonoelasticity has the advantage of the robustness and simplicity of signal processing. In pulse-doppler method, the amplitude of vibration is measured by transmitting a

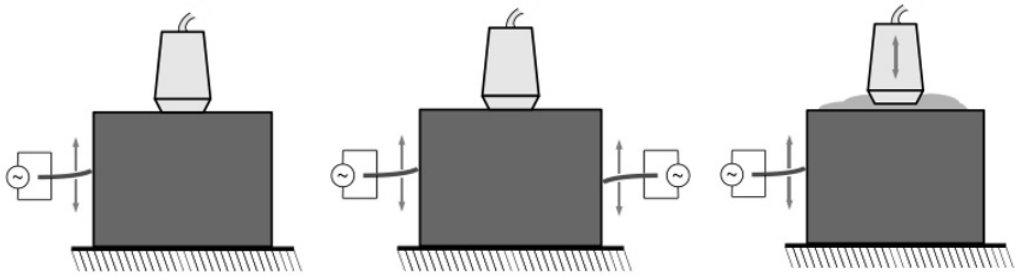

(a) (b) (c)

Figure 2.5: Setup for sonoelasticity imaging: (a) Vibration-amplitude imaging, (b) Crawling-wave imaging and (c) Holographic-wave imaging. Figure reproduced by kind permission of Joel Edward Lindop [1].

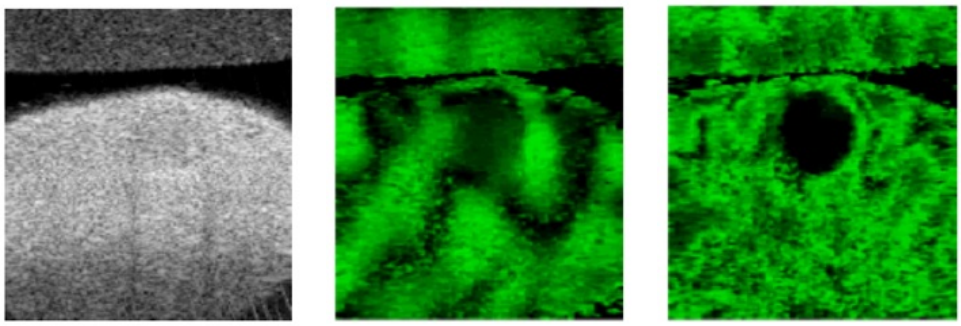

(a) (b) (c)

Figure 2.6: Vibration-amplitude images, reproduced by permission of Kenneth Hoyt, University of Rochester, NY, USA: (a) B-mode image showing a tissue-mimicking phantom with a stiff spherical inclusion, 7 mm in diameter, of matched echogenicity. There is almost no contrast between the inclusion and the background. (b) Vibration-amplitude image produced by mechanical excitation at 150 Hz. (c) Vibration-amplitude image produced by mechanical excitation at 250 Hz. Modal patterns dominate the 150 Hz image, so the 250 Hz image gives a better indication of the inclusion geometry [5].

narrow-bandwidth pulse of ultrasound into the tissue. For estimating vibration amplitude at various depths along the beam, it is needed to window the echoes and calculate the spectral variance [87]. Kasai $et.\ al.$ [74] first described the well-known auto-correction method to have fast computation and sufficient accuracy for the task. As derivatives are not needed to be taken and there is insignificant noise level compared to vibration-amplitude artifact, relatively low accuracy is not considered as a major problem. However, for other elastic imaging concepts low accuracy is not acceptable.

The Vibration amplitude and stiffness is not directly linked. Owing to diffraction, refraction, reflections and viscous losses (wave severity degrade away from the vibration source), vibration amplitude images are affected by nonuniform wave severity as stress nonuniformity is a limitation of quasistatic strain images. Viscous losses are

frequency-dependent, hence lower frequencies enter deeper into the tissue, and however the images then have lesser resolution [88]. Images such as Figure 2.6(c) show that qualitative result of vibration-amplitude images which could sometimes be helpful for lesion detection though there is no hope of transforming vibration amplitude into quantitative estimates of mechanical properties [89].

Modal patterns are an important superfluous artifact in vibration-amplitude images. As noted in [1], they arise for the reason of interference between steady-state shear waves travelling in inverse direction [90], therefore regions with reduced vibration amplitude appear in patterns not related to local changes in mechanical properties. The overall geometry of the scan target, its global mechanical properties, and the position and frequency of the vibrator determine the patterns. For example, the images in Figure 2.6(b) showing the vibration amplitude is dominated by modal patterns. Comparison with image 2.6(c) indicates that the geometry and the strength of modal patterns is dependent on frequency. By vibrating at multiple frequencies together, the artifacts can be made less severe ; some modal patterns reject the joint vibration-amplitude image, although they cannot be removed completely [68, 90, 91].

As an outcome, vibration-amplitude images are possibly more troublesome to interpret than quasistatic strain images. Additionally, the practical scanning setup is more complex. Limited improvement has been made looking forward to clinical demonstration: in vitro homogeneous phantoms are perfect and exact. Moreover, the practical scaning setup is not that easy. Limited advancement has been made towards clinical demonstration: though in vitro scanning of prostate tumors after excision pointed out the possibility of producing useful images of germane biological tissue [92, 93], the prospect of vibration amplitude imaging entering routine clinical practice seems distant.

Other kinds of sonoelasticity imaging might be further fruitful. As noted in [1], phase as well as amplitude is recovered by a more complicated and noisier extension to the signal processing for vibration amplitude imagining. Yamakoshi $et\ al.$ used maps of amplitude and phase to form images of wavefront propagation through a ROI [70]. Wavefront images are used for estimating shear wavespeed by a manual image-analysis procedure [35] since vibration amplitude images were intended for detecting small stiff inclusions [85, 86, 90]. For assessing diffuse conditions in large organ such as the liver successful estimates would be useful.

As quote [1]: ‘The manual way to wavefront analysis provides as a noise rejection strategy as users learn to ignore data that seem not reliable [94]. Practically, the final output is a single number not an image. The stiffness has been evaluated in a clinical test involving 200 plus liver patients [94]. Despite surprisingly wide variation in the speeds measured within each group, significant differences were recorded between the

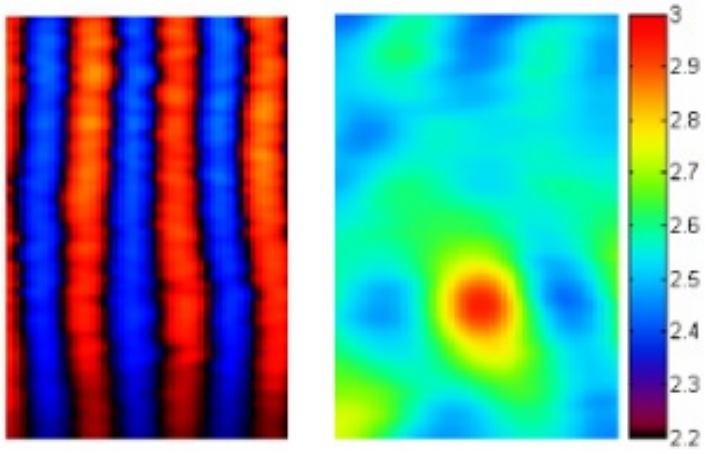

(a) (b)

Figure 2.7: Crawling-wave images, reproduced by permission of Kenneth Hoyt, University of Rochester, NY, USA: (a) Vibration-amplitude image of a gelatin phantom containing a stiff inclusion with a diameter of 5 mm. Vibration sources at 199.9 Hz and 200.1 Hz transmit shear waves from either side. A special color map highlights the wavefronts, with red-black-blue indicating low-medium-high vibration amplitude. (b) Shear wavespeed image (units of ms-1) produced by analyzing a sequence of vibration-amplitude images. Shear wavespeed estimates differentiate successfully between the background and the stiff inclusion [11]. Figure reproduced by kind permission of Joel Edward Lindop [1].

average wavespeed estimates from patients with different conditions. Including modal patterns, many complicated effects associated with continuous vibration introducing bias into wavespeed estimates [21]. The manual way to image analysis is very much arduous and the wavespeed estimates need to accurate and useful to justify the effort. Further technical development reported in [95] but the technique seems at last to have been abandoned.

Modal patterns in vibration amplitude images are the most prospectus form of sonoelasticity. Special interference patterns can be generated to support shear wavespeed estimation. A standing wave with nodal spacing proportional to the shear wavespeed, or a pair of vibrations at slightly different frequencies produces a moving interference pattern(the crawling wave) with speed proportional to the sgear wave speed multiplied by different frequency [96] is produced by two sources of equal frequency. On the other hand, the ultrasound probe is vibrated at a frequency near that of the shear waves converting steady state shear excitation from a single vibrator into a slow moiving interference pattern (the holographic wave) [97]. Figure 2.6(b)-(c) shows the setups for these techniques. Quantitative shear wavespeed images can be potentially through the analysis of the interference patterns.

The major benefit of the crawling and holographic wave techniques compared to the method of Yamakoshi $et.\ al.$ [3, 94] is that larger quantities of more accurate wavefront data are generated and is a more promising base for developing automatic

analysis methods [96, 98]. When the wavespeed is measured in inhomogeneous media, the holographic wave technique seems to be biased which is described by [21]. For having a correct estimate of shear wavespeed by the using the crawling-wave technique, the interfering wavefronts should be planar and parallel which is difficult to have and may be impossible in homogeneous tissue. So, further analysis [99] is needed to overcome this particular limitation. Despite having biased absolute values, the qualitative discrimination of a stiff inclusion has been displayed a number of times using vitro scanning [97, 98]. For further clarification Figure 2.7 is referred. Whether crawling or holographic-wave imaging can be applied successfully to in vivo scanning, will be interesting to see in the view of a complicated experimental setup.'

Vibro-acoustography

Radiation force is the force induced by the absorption of energy near the focus of a high-intensity focused ultrasound beam [100]. As mentioned in [10], in some special cases, the force prevails within a small area near the focus [56]. Elasticity imaging comprises several concepts which exploit this effect, especially in the dynamic category. Besides, continuous excitation by radation force is used in vibro-acoustography is deemed a form of elasticity imaging.

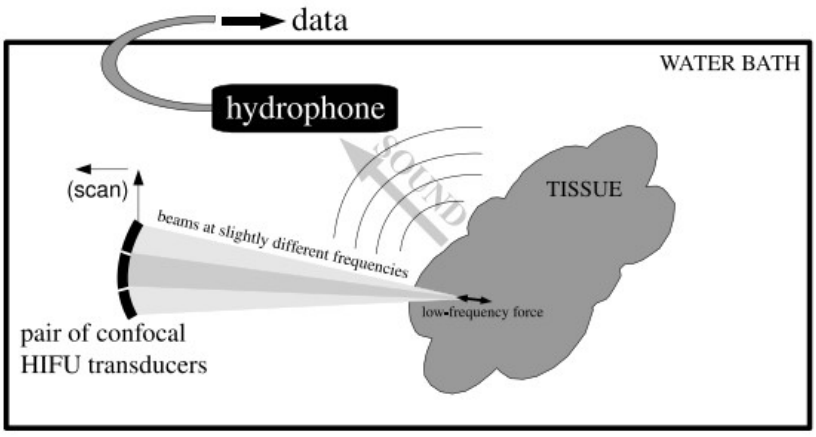

Figure 2.8: Setup for vibro-acoustography. A pair of confocal HIFU transducers at slightly different frequencies produce an oscillatory force at the difference frequency at their focus, from which sound is emitted and detected by a hydrophone. By scanning different points throughout the tissue, an image can be constructed of the sonic amplitude, which is related in a complicated way to mechanical properties [5]. Figure reproduced by kind permission of Joel Edward Lindop [1].

As quote [1]: 'Transmitting at slightly different frequencies, (see Figure 2.8), the tissue is excited for a pair of confocal HIFU beams. The foci overlap in a dense confined region, where radiation pressure muddled at the beat frequency (typically 10 kHz). A hydrophone detects the resulting motion around the focus makes an acoustic

wave [12, 101]. Scanning over the ROI construct an image and plotting the measured power of the sound from each focal space. Pixels in a vibro-acoustogram symbolize the merged effects of diversification in tissue properties above the focus (shadowing and refraction), the level of engrossment at the focus, the size of the resultant fluctuated motion (which relies on mechanical properties near the focus), and the transfer function to the signal which is recorded by hydrophone (which relies on mass mechanical properties).

However, vibro-acoutogram are fully determined by mechanical properties. There is no speckle in the images and it is advantageous in comparison to conventional ultrasound images, and they acquire high resolution, probably superior to that of any other elasticity imaging abstract idea, [12, 101, 102]. However vibro-acoustography provided information is not even close to similar to the quasistatic elasticity imaging. It would be highly difficult to relate pixel values in a in a vibro-acoustogram to a specific mechanical property such as Youngs module vibro-acoustography may be a good methodology for pointing out microcalcifications in breast issue; the principal has been proved by ex vivo scanning of histological samples [102, 103]. However this thesis is motivated to produce images that shows contrast between regions of tissue that are soft or hard, which vibroacoustograms do not [104]. Similarly conventional ultrasound images relies on mechanical properties but a clinician is not eligible to differentiate between hard and soft tissue by looking at a conventional ultrasound display. '

Dynamic (transient)

Transient concepts mean if impulsive mechanical excitation is used, tissue will have a short duration response to the excitation. As noted in [1], the tissue in which the transient excitation is applied, stresses spread to the nearby tissues at a finite rate which varies as per the wavespeed. In the initial moments, how the response will be solely depends on mechanical facets at the point of application.

As data is needed to be captured very fast so the realization of transient methods is technically challenging. Ultrafast ultrasound scanning, a significant technological development, employs novel beamforming to acquire 2D ultrasound frames up to 10000 Hz [105] which is 100 times faster than commercial scanners available in todays marketplace. So, it is feasible to acquire many 2D snapshots to record the propagation of a single shear wave passing through soft tissue.

Transient shear imaging

As noted in [1], transient elasticity imaging with impulsive excitation has been proposed as a solution to biases in shear wavespeed estimates basing on continuous excitation by Catheline $et.\ al.$ [21]. Besides, vibration of the transducer can generate a

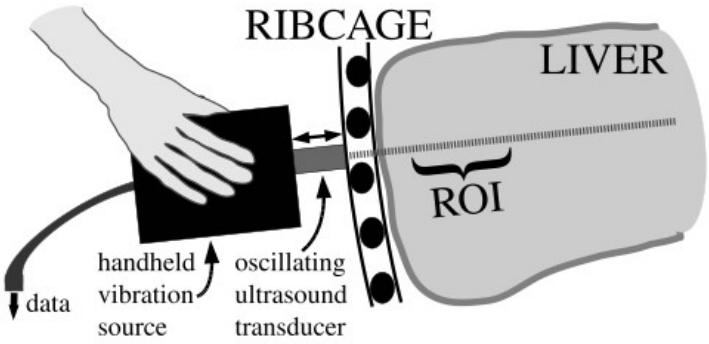

Figure 2.9: Setup for using $FibroScan^{®}$ to measure shear wavespeed. Figure reproduced by kind permission of Lindop [1].

suitable shear wave impulse having a center frequency of 100 Hz spreading along axis of single-element ultrasound transducer [106]. In Figure 2.9, it has been shown that by mounting the transducer on vibration in a handheld device, a practical system was constructed [106]. The need of using vivo scanning was there to display the accurate measurement of shear wavespeed in homogeneous tissue. To generate 2D elasticity images by tracking the motion of a plane wave in 2D, ultrafast ultrasound scanning has been used [107]. It is possible to generate a shear wave by mounting the ultrasound probe on a handheld vibrator by using the single-element device [107]. Compared to the primary utility of shear wavespeed calculation characterizing big tissue regions, the added value associated with 2D images from the instrument is limited as it is difficult to perceive surface-generated shear waves that spread sufficiently parallel to the imaging plane covering the ROI for producing accurate images having good radiation [31, 107].

However, clinicians highly prefer the simple scanning system producing accurate, repeatable measurements of shear wavespeed. FibroScan is the name of single-transducer device exists as a commercial product [55]. It produces a single wavespeed estimate for characterizing bulk stiffness in a big area of issue which is bound to be affected by a diffuse condition near to the surface. For examples of the first clinical study, Figure 2.10 is referred. As the liver has to be a potential target, so FibrosScan has advanced swiftly towards widespread adoption as an apparatus for predicting liver fibrosis, along with thousands of patients already comprehended in clinical trials.

Acoustic radiation force impulse (ARFI) imaging

For the generation of images portraying relative differences in tissue stiffness, Acoustic Radiation Force Impulse (ARFI) imaging has been developed [29], in which the tissue displacement response is monitored within the ROE, and image data are generated by

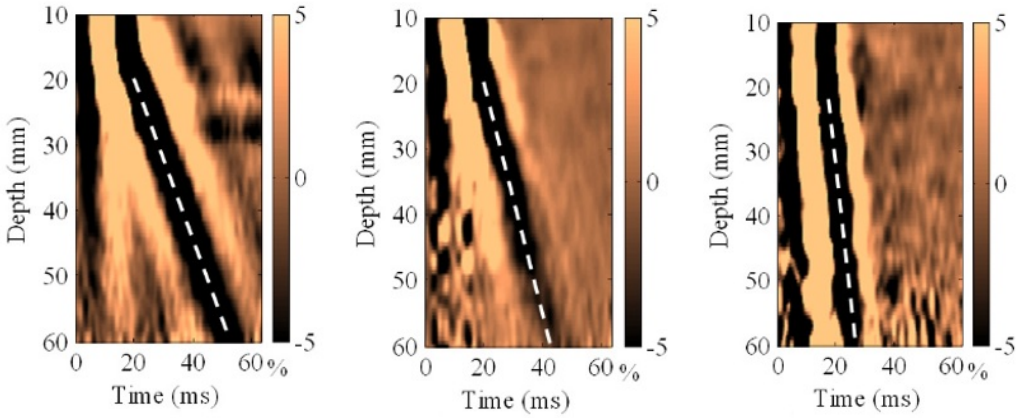

(a) (b) (c)

Figure 2.10: The $FibroScan^{®}$ display [39], reproduced by permission of Laurent Sandrin, EchoSens, Paris, France (http://www.echosens.com). These images from clinical scans of liver in vivo shows strain data over depth (vertical axis) against time (horizontal axis). The gradient of the dark stripe is the axial component of the shear wave velocity, from which stiffness may be inferred. (a) Healthy patient. (b) Mild fibrosis. (c) Liver cirrhosis. Figure reproduced by kind permission of Joel Edward Lindop [1].

sequentially interrogating different lateral positions, as is done in conventional 2D ultrasound imaging. To recite [108]: 'Images are then synthesized of tissue displacement at a given time after radiation force excitation at each interrogation location. Monitoring the displacement response within the ROE has the advantage of higher displacement magnitude and SNR (as compared to outside of the ROE), but quantification of tissue elasticity within this region is challenging due to inertial effects within the ROE. To create quantitative elasticity images from impulsive radiation force excitations, the displacement response is typically monitored outside of the ROE. The speed of the shear wave propagation is quantified and used to estimate the tissue shear modulus, as was originally proposed by Sarvazyan et al. [23] as shear wave elasticity imaging, or SWEI, [27]. Early implementations of this approach utilized inversion of the homogeneous Helmholtz equation to estimate tissue shear modulus [5, 30]. However, most groups have moved to utilization of time-of-flight wavespeed estimation methods, due to challenges associated with differentiation of noisy ultrasonic displacement estimates [31-34]. ARFI images are formed using commercial diagnostic ultrasound scanners to both generate localized, impulsive acoustic radiation forces in tissues, and to monitor the transient, dynamic displacement tissue response within the ROE using correlation based methods. An ARFI pulse sequence consists of tracking beams and pushing beams. The tracking beams are conventional B-mode ultrasound beams (A-lines), and the pushing beams are transmitted along the same A-line and have higher intensity, with typical parameters. A typical sequence involves transmitting a series of pre-push

reference A-lines, which are used to monitor underlying physiologic motion, followed by a pushing pulse along the same A-line, and then a series of tracking Alines that are utilized to monitor the tissue displacement response within the ROE of the pushing beam (typically for 3-5 msec at pulse repetition frequencies (PRFs) between 5 and 10 kHz). In ARFI images, the displacement data from multiple, sequentially interrogated radiation force excitation locations are synthesized into a single dataset representing the temporal displacement response from within each ROE throughout a 2D (or 3D) tissue region of interest (ROI). As shown in Figure ARFI, these datasets are rich with information about the transient tissue deformation. ARFI images have been generated of tissue displacement at a given time after force application, the maximum tissue displacement, the time the tissue takes to reach its peak displacement, and the time it takes the tissue to recover [41]. In the presence of uniform acoustic attenuation, ARFI displacement magnitude images generally reflect tissue structure and relative stiffness. Images of the transient temporal behaviors, such as the time to peak displacement and recovery time can be used to derive quantitative estimates of tissue stiffness [21, 37]. The majority of ARFI images generated in clinical applications portray relative displacement at an early time after the force application (i.e. Figure 2.11(b)) in order to optimize the accuracy of structural details [35].'

Supersonic shear imaging

Supersonic shear imaging was first introduced by Bercoff [26, 43]. To quote [109]: 'The ultrafast echographic imaging approach was coupled with the remote generation of a supersonic shear wave in tissues using a modified sequence of ultrasonic beams transmitted by the echographic probe. This transient elastography approach, called supersonic shear imaging (SSI), provides a way to apply both the mechanical vibration and the ultrafast imaging of the resulting shear wave propagation by using a conventional ultrasonic probe. The concept of remote palpation induced by the radiation force of an ultrasonic focused beam is not new and was introduced in the medical imaging community by [32]. Recently, Trahey et al. [18] and Nightingale et al. [22] proposed to use this concept to induce motion in the focal area of the ultrasonic beam and to image the resulting displacement at the location of the pushing beam. A complete strain map can be computed by repeating, at every focal spot, the pushing beam and displacement detection. However, this requires a significant amount of acoustic energy. Nightingale et al. [22] also applied this concept to the visualization of shear waves generated by the acoustic radiation force by repeating the acoustic radiation force for different speckle-tracking locations. Finally, they emphasized the benefit of using the ultrasonic radiation force to discriminate the liquid/solid behavior of tissues and consequently to provide a clever discrimination between benign viscous cysts and soft tumors [24]. The

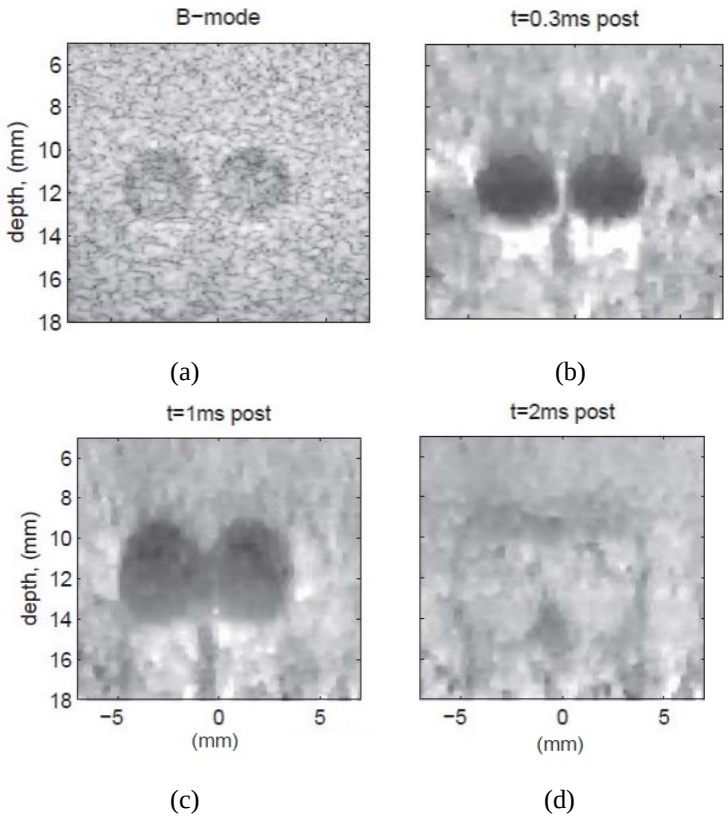

Figure 2.11: Experimental data: matched B-mode (a) and normalized ARFI displacement images, (b)-(d), of a Computerized Imaging Reference Systems, Inc. Norfolk, VA) custom tissue mimicking phantom (E = 4 kPa) with two 3 mm spherical lesions (E=58kPa). The lesion contrast in the ARFI images is largest at t=0.3 ms (b), decreases with time after excitation (c), and reverses later in time (d). In addition, the lesion size appears to grow with time post-force, which is caused by shear wave propagation and reflection at lesion boundaries [35]. Note also the posterior enhancement, or increase of displacement beneath the lesions in (b) and (c). This arises because the lesions were slightly less attenuating than the surrounding tissue, thus the tissue beneath the lesions experienced larger radiation force than that adjacent to it. Figure reproduced with permission from: [36].

SSI approach tries to merge the advantages of the previous techniques by combining the remote palpation of the acoustic radiation force imaging technique and the ultra-fast echographic imaging approach of transient elastography into a single ultrasonic sequence (lasting less than several tens of milliseconds). This combination is expected to provide a quantitative elasticity imaging mode, with a significant reduction of operator dependence compared with static elastography [32]. This manuscript presents its initial clinical investigation for breast cancer diagnosis. There were several purposes of this preliminary study: to evaluate the ability of SSI in providing millimeter-resolution images of breast elasticity, to examine SSIs ability to clearly emphasize the appearance of various breast lesions on these images and to investigate SSIs role in the diagnosis of breast lesions.'

2.4 Modulus reconstruction

Modulus imaging has great potential in soft-tissue characterization since it reveals intrinsic mechanical properties. A novel Youngs modulus reconstruction algorithm that is based on surface stress and strain distribution is described in this thesis paper. To quote [110]: 'The elastic properties of biological tissues are usually modified by disease. Surgeons often describe the feel of excised abnormal tissues. As a result, a quantitative measure of the elastic properties of tissue should be useful in diagnosing abnormalities. The physical quantities that describe tissue elastic properties are stress, strain, and elastic moduli, and methods have been developed to estimate each of these. Palpation, which has been used for more than 4000 years, utilizes tissue surface stress information to detect tissue abnormalities. Palpation remains an effective diagnostic tool. In fact, the majority of breast tumors are discovered with palpation [1]. However, palpation is qualitative and lacks sensitivity to small deep abnormalities. Quantitative methods similar to palpation have been developed to visualize surface pressure [2], [3]. Other recent developments in bioelasticity imaging techniques involve accurately and noninvasively measuring the tissue strain distribution during external compression. Studies have shown that these techniques show promise in diagnosing and monitoring diseases of the breast [4], [7], kidney [8], [11], and blood vessels [12-13].

Mapping stress or strain distributions provides only relative information about tissue elasticity. Using either stress or strain information alone, one can only identify a region of tissue that is stiff (or soft) relative to its surroundings. Elastic moduli provide an absolute measure of tissue elasticity that is intrinsic to the material.

The stress or strain distributions alone lack a one-to-one relationship with the elastic moduli distribution. Images of the stress or strain distribution may also include misleading artifacts that could lead to uncertainties in diagnosing tissue abnormalities.

Therefore, it is desirable to measure elastic moduli in bioelasticity imaging techniques. However, measuring the distribution of elastic moduli is more difficult than either the stress or strain distribution. The theory of mechanics shows that to describe the complete elastic properties of a material requires a tensor that has 81 components [14]. Clearly, it is impractical to measure all these components. Assumptions can be made to simplify the problem and reduce the number of unique tensor elements. If a material is assumed to be continuous, incompressible, and isotropic, then its elasticity can be completely described by one elastic modulus, either Youngs modulus or shear modulus. Strictly speaking, none of the above assumptions are valid for biological tissues, but most biological tissues closely approximate continuous and incompressible materials. Some tissues, such as muscle, are anisotropic in their structure, function, and mechanical properties. For this paper, however, we will assume tissue to be continuous, incompressible, and isotropic as a first approximation.

Currently, ultrasonic-based techniques for measuring the elastic modulus of tissue fall into two categories. First, dynamic compression techniques [15], [18], such as sonoelasticity, use a vibrator to propagate low-frequency pumping waves into tissue. In the most promising of these approaches, shear wave velocity or wavelengths are estimated, and from these the shear modulus can be estimated. However, problems associated with this technique are high image noise, low spatial resolution, and difficulty in propagating the shear wave energy across tissue boundaries.

The other category is referred to as (quasi)static compression techniques. In static compression techniques, the tissue Youngs modulus distribution is estimated from the tissue deformation and boundary pressure measurements. The methods to estimate tissue deformation have been extensively discussed in ultrasound based elastography [19], [28]. The tissue is deformed either by an external force or an internal force. The RF echo waveforms before and after an incremental deformation are recorded, and the tissue displacement distribution is estimated by comparing these RF waveforms. Tissue internal displacement can be also obtained using magnetic resonance imaging [29], [31] and optical elastography [32] techniques. Youngs modulus estimation can be performed utilizing the tissue deformation information obtained with the strain imaging techniques. In addition to the displacement distribution, some Youngs modulus estimation methods also require knowledge of the pressure or force boundary conditions.

There are four methods in the literature for reconstructing the Youngs modulus distribution based on static compression techniques for displacement estimation. The first method estimates Youngs modulus by numerically solving a second-order partial differential equation that describes a linear, isotropic, incompressible medium under static deformation [33]. That method requires significant spatial smoothing of the displacement estimates to obtain second-order partial differentials that are also smooth.

Hence, with noisy displacement estimates, that method inherently has low spatial resolution. Another problem associated with that method is that for a two-dimensional (2-D) analysis, the force boundary condition of the medium must be known on all sides. However, in practice, the force distribution can only be (easily) measured on one side (the compression surface) of the medium.

The second method uses an iterative technique to reconstruct the modulus distribution [34], [35]. That method uses finite element analysis (FEA) to solve the forward elasticity problem. The input to the FEA algorithm is the measured displacement field, the assumed boundary conditions, and an initial guess of the modulus distribution. The output of the FEA algorithm is an estimate of the displacement distribution. The difference between the measured displacement distribution and the FEA prediction is used to adjust the modulus distribution from its initial guess. By repeating the process multiple times, one can obtain a modulus distribution that minimizes the displacement distribution difference in a least squares sense. The advantage of that approach is that it does not require knowledge of the pressure boundary conditions. However, without knowing the boundary pressure, only relative modulus estimates can be obtained. In other words, the ratio of the modulus between different locations can be determined. Although that method can reduce the artifacts in strain images, it does not provide absolute measurement of the tissue modulus distribution which can be useful in tumor discrimination as suggested in [36], and an incorrect initial modulus guess may result in convergence to an incorrect modulus distribution. For media, such as tissue, that have a complicated modulus distribution, a good initial guess for the modulus distribution is difficult to obtain.

In the third modulus reconstruction method, a finite-difference approach is used to describe the elasticity problem in a medium [37]. That approach rearranges linear equations that describe the forward problem so that the modulus distribution becomes unknown variables in these equations. The modulus distribution can then be solved. However, that method also requires knowledge of the boundary conditions on all sides of the object.

The fourth approach uses a variational method to formulate the forward solution [38]. Then the terms with unknowns are rearranged to derive a matrix equation similar to ours. However, the boundary force condition was not utilized in their treatment. Hence, this method can only reconstruct the ratio between the Lame constants and tissue mass density.'

2.5 Conclusion

The elasticity methods obtaining viscoelastic characterization of tissue provide efficient indicators identifying diseased tissue versus normal tissue. Elasticity methods can be commercial applications, a true testament to the progress of the field. General Electric (GE) and Philips 1.5T MRI scanners have been used in MREs report. Siemants, Philips, GE, Hitachi, Toshiba, Aloka, Ultrasonix implemented Quasi-static-elastography on many systems. Transient elastography has been implemented in the FibroScan product produced by Echosens (Paris, France) in an effort to quantify liver stiffness to diagnose liver fibrosis. The literature has many clinical studies reported. In Summary the viscoelastic material properties of soft tissue can be characterized using elasticity imaging methods. These viscoelastic material properties vary between normal and diseased tissue providing a unique difference mechanism for diagnosis of different pathologies. A number of elasticity measurement and imaging methods have been embodied and improved. This model has great potential for many different applications to assist to identify disease and improve patient outcomes. In the next chapter a novel algorithm is discussed. This algorithm can be used for the influential modulus prediction process.

Chapter 3

Proposed Approach for Modulus Estimation

3.1 Introduction

A reconstruction technique for breast tissue elasticity modulus is described in this chapter. This technique assumes that the geometry of normal breast and pathological tissues is available from a realistic FEM model. Furthermore, it is assumed that the modulus is constant throughout each tissue volume. The technique, which uses quasi-static strain data, is iterative where each iteration involves modulus updating followed by stress calculation. Breast mechanical stimulation is assumed to be done by the pressure given by the ultrasound probe. As a result, stress is calculated using the finite element method based on the well-controlled boundary conditions of the compression plates. Using the surface stress, calculated stress in other area and the measured strain, modulus updating is done element-by-element based on Hooke's law.

3.2 Proposed Algorithm

The proposed method was developed assuming that the tissue is linearly elastic and isotropic undergoing small deformation. As such, the following equation, which is derived from Hooke's law, governs each point in the tissue domain:

$$E = \frac{\sigma}{\varepsilon} \tag{3.1}$$

In this equation, ε and σ denote the tissue strain and stress developed under mechanical stimulation, respectively. The tissue was assumed to be a near-incompressible material, hence tissue's Poisson's ratio 0.49 was employed in the reconstruction. The reconstruction technique is iterative as the YM followed a $E^{(i+1)} = f(E^i)$ recursive formulation used in each iteration, where f involves strain calculation using finite element method. In this approach, it is assumed that the tissue elasticity uniform through-

out the volume of each of the normal and pathological tissues. The proposed novel modulus reconstruction algorithm follows the following steps:

1. Actual Strain distribution will be calculated from pre and post compression US data. At the same time, only the upper surface stress data will be collected by the 1D pressure sensor attached with the US probe (model proposed in Figure 3.6).

2. First predicted stress distribution is calculated based on the surface known stress and known strain distribution, ε_{actual} (Equation 3.5).

3. First YM distribution is calculated based on the first predicted stress distribution and known strain distribution (ε_{actual}) using Hooks law.

4. The YM is clustered for a defined number of clusters based on the structure of the tissue viewed in the B-mode image.

5. Then the full cluster is replaced by the average value of that clusters YM.

6. Simulated tissue model is created based on previous step. Same amount of stress is placed on the top surface for this simulated model.

7. From the simulated model, directly the strain distribution (ε^i) is collected.

8. The error distribution value of the strain is calculated (Equation 3.7) compared with the actual strain (ε_{actual}) to the simulated strain distribution (explained in the previous step).

9. Strain distribution is updated based on the error distribution of the strain value Δ, actual strain value and top surface stress value (Equation 3.6).

10. Step 2 to 7 will be repeated targeting to a certain level of average error distribution value of the strain.

The flow diagram of the proposed method is shown in Figure 3.1.

3.3 Finite Element Modeling

A model of breast tissue is created using COMSOL Multiphysics software. COMSOL Multiphysics is a cross-platform finite element analysis, solver and multi-physics simulation software [111]. It allows for the creation of a conventional physics-based user interface. The size of the overall model is taken as 3 cm width and 3.6 cm depth. The tumor is modeled by 1 cm diameter circular structure and placed in different positions

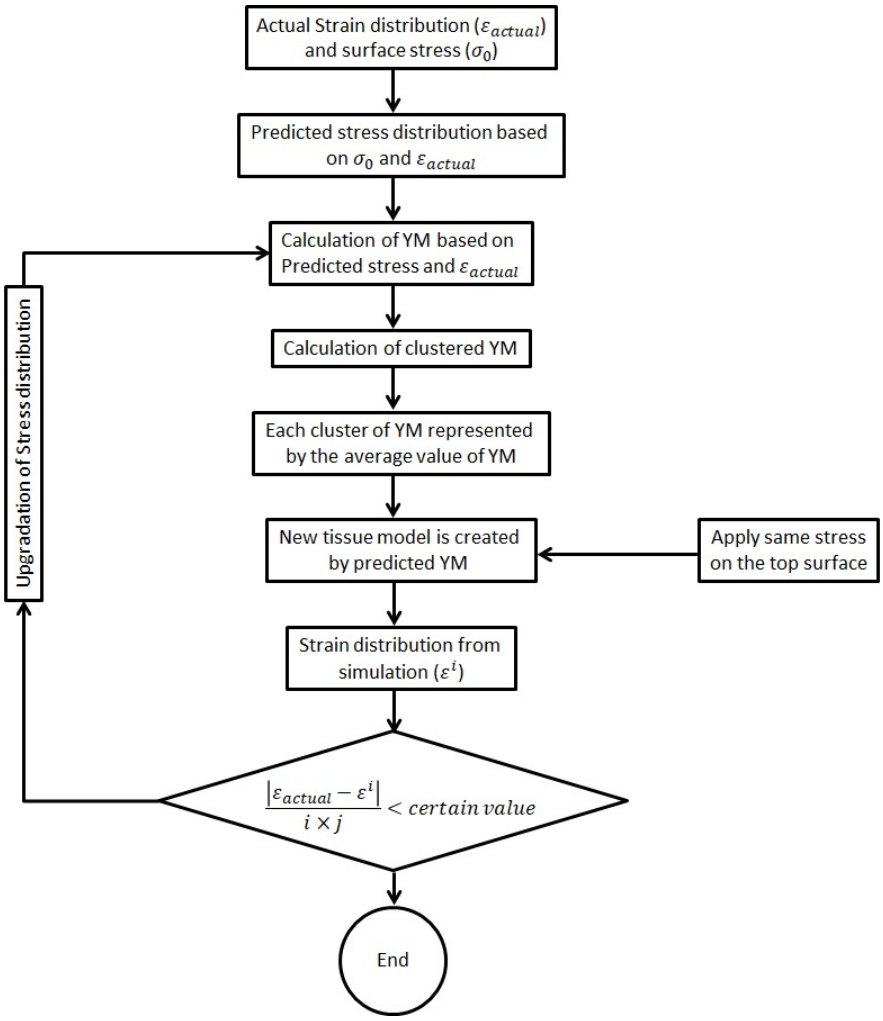

Figure 3.1: Flowchart illustrating the YM reconstruction procedure using surface stress.

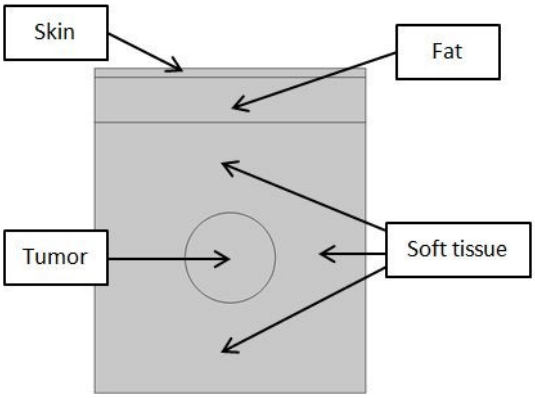

Figure 3.2: Geometry of the FE model of breast tissue

for analysis. Skin and fat tissue depth are taken as 0.1 cm and 0.5 cm respectively where the width is 3 cm.

Water is the selected material used to represent various parts of the model. Distinctions were made between soft tissue, tumor, skin and fat by varying the mechanical properties. The altered properties included the Poisson's ratio and Young's modulus according to the literature [11]. Poisson's ratio is the ratio of the proportional decrease in a lateral measurement to the proportional increase in length in a sample of material that is elastically stretched. Young's modulus is a measure of the ability of a material to withstand changes in length when under lengthwise tension or compression. Sometimes referred to as the modulus of elasticity, Young's modulus is equal to the longitudinal stress divided by the strain. Poisson's ratio is taken as 0.495 for soft tissue, tumor, skin and fat. Young's modulus is considered as 10 kPa, 40 kPa, 200 kPa and 1.5 kPa for soft tissue, tumor, skin and fat respectively. It is assumed that bone is at that side. All the other sides were left free for movement.

Table 3.1: Mechanical properties of tissue components of breast

Tissue type	**Poisson's ratio**	**Young's modulus**
Soft tissue	0.495	10 kPa
Tumor	0.495	40 kPa
Skin	0.495	200 kPa
Fat	0.495	1.5 kPa

For Young's Modulus reconstruction, stress and strain values are required. In a practical scenario, compression is made by the ultrasound probe. The stress field is usually non-uniform, so strain data are ambiguous, but strain imaging is the simplest way of displaying quasistatic deformation data to provide a visual indication of variation in mechanical properties [7, 12]. Our model utilizes a fixed displacement of 0.03 cm to represent the compression from an ultrasound probe.

3.4 Realizing Strain data

3.4.1 Strain resolution

In the practical case, the strain data will be calculated from the pre and post RF data. The most obvious restriction on strain image resolution comes from the spacing between neighboring estimation locations, but it is less important than filtering effects related to the size of windows and kernels. The only disadvantage of dense estimation spacing is increased computation time, while it improves both resolution and SNR . The estimation locations used in this chapter are very closely spaced, so as to focus on

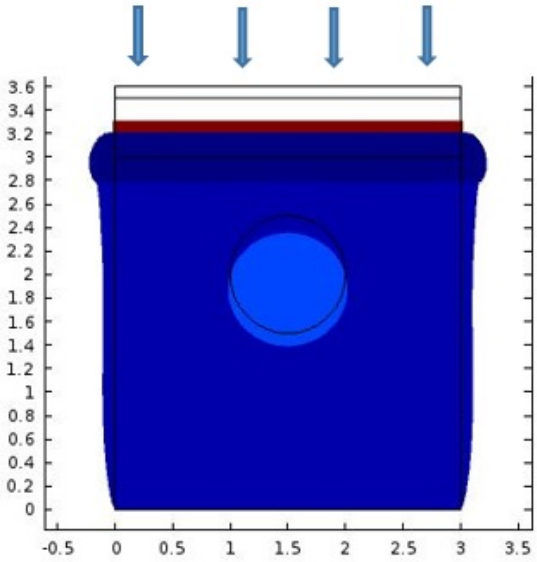

Figure 3.3: Ultrasound probe is pressed at the top surface which is represented by fixed displacement of 0.03 cm

the significance of the other parameter choices.

The Effects on strain estimates of changes to window and kernel size are similar, though not identical, to denoising by applying a moving average (MA) filter. The overall error decreases as a MA filter gets larger, because uncorrelated error components spanned by the filter average to zero. However, the output from a large MA filter has coarse resolution. There is no universal definition of resolution that can be applied sensibly to all imaging tasks. For the present analysis, the resolving limit is defined as the feature scale, L_r, at which there is no longer any positive contrast between two or more bands of low strain sandwiching and surrounded by background material with higher strain (see Figure 3.4). The resolving limit is reached when strain estimates after the filter exhibit zero contrast between the low and high strain bands. For example, the resolving limit of a MA filter is half the filter length. The resolving limit is assumed similarly to be approximately proportional to window and kernel dimensions, although the constant of proportionality may not be the same in both cases. The greatest estimation accuracy at a given resolution will usually be achieved by windows and kernels of the maximum allowable size.

3.4.2 Strain estimation error

Differentiation amplifies estimation noise, particularly if the displacement estimates are closely spaced. Figure 3.5 illustrates this point for 1 D strain estimation. Predicting strain estimation error requires an understanding of how displacement estimation error filters through. There are various techniques for reducing noise in gradient estimates,

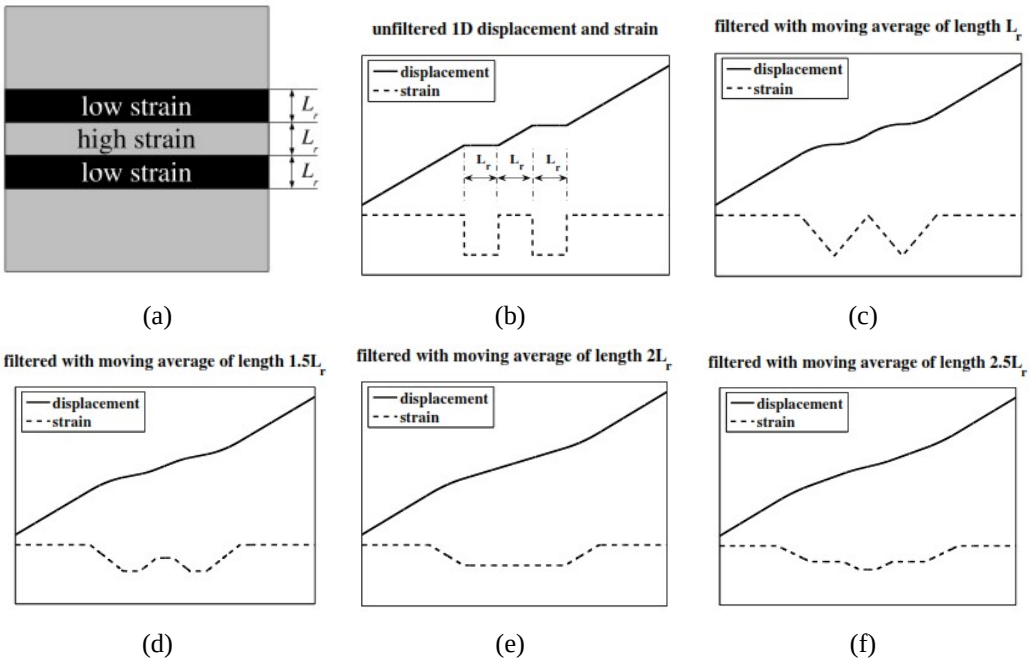

Figure 3.4: Effect of a MA filter on the contrast between low and high strain bands. (a) The axial resolving limit is the axial length scale at which features are just resolved, with a strain field that is uniform in the lateral direction. (b) Displacement and strain fields against distance. (c) A MA filter (length=L_r) easily resolves the different strain regions. (d) Resolution is still achieved with length=$1.5L_r$. (e) The contrast is zero when the filter length is $2L_r$. (f) Filter lengths > $2L_r$ register negative contrast. Figure reproduced by kind permission of Joel Edward Lindop [1].

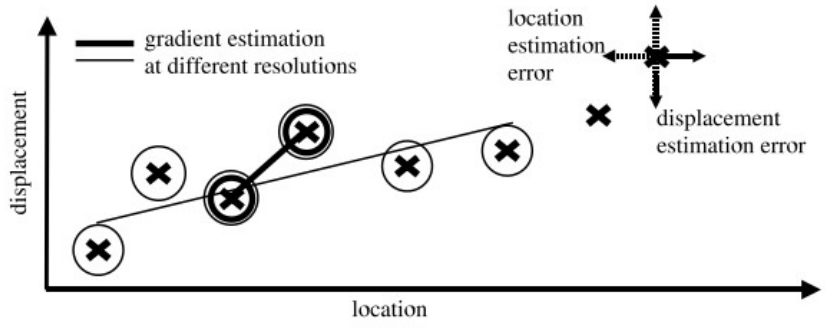

Figure 3.5: 1D illustration of strain estimation. Errors in strain estimates depend on the resolution of the gradient estimator, but the original sources of error are the locations and values of displacement estimates. Figure reproduced by kind permission of Joel Edward Lindop [1].

including lowpass filtering and wavelet denoising. As noted in [1], the following analysis focuses on piecewise-linear least squares regression, which is more commonly applied. Analysis of alternative approaches would involve similar considerations. The simplest unweighted least squares gradient estimate is [11]

$$\hat{\varepsilon} = \frac{\sum\limits_{\Omega_n \epsilon\ K_m} \check{y}_n \hat{u}_n}{\sum\limits_{\Omega n \epsilon\ \kappa} \check{y}_n^2} \tag{3.2}$$

where y denotes axial distance. The strain estimate, $\hat{\varepsilon}$, is produced using data from a set of displacement estimation windows, $\{\Omega_n\}$, comprising displacement estimates $\{\hat{u}_n\}$ at locations $\{\check{x}_n, \check{y}_n\}$ (measured relative to the center of kernel K_m). Note that, although $\{\check{y}_n\}$ are axial location estimates, the kernel is usually 2 D, taking displacement estimates from multiple neighbouring columns. The set of displacement estimate locations must be symmetric about the center of the kernel to ensure that the strain estimate has greatest validity at that point. The scale of strain estimation errors is predicted by evaluating the variance of this estimator. In general, there are errors in both displacement and location, all of which lead to strain estimation error. Location errors in $\{\check{y}_n\}$ are assumed to be negligible, having been substantially reduced by amplitude modulation correction (AMC). This leaves errors only in $\{\hat{u}_n\}$, resulting in the following strain estimation variance if covariances are negligible [11]:

$$\sigma_{\hat{\varepsilon}}^2 = \frac{\sum\limits_{\Omega_i \epsilon\ K_m} \check{y}_i^2 \sigma_{ui}^2}{\left(\sum\limits_{\Omega i \epsilon\ \kappa} \check{y}_i^2 \right)^2} \tag{3.3}$$

It is also possible that the displacement estimator introduces significant covariances, in which case a more complicated expression must be evaluated:

$$\sigma_{\hat{\varepsilon}}^2 = \frac{\sum\limits_{\Omega_i \epsilon\ K_m} \sum\limits_{\Omega_j \epsilon\ K_m} \check{y}_i \check{y}_j \sigma_{ui} \sigma_{uj}}{\left(\sum\limits_{\Omega i \epsilon\ \kappa} \check{y}_i^2 \right)^2} \tag{3.4}$$

3.4.3 Simulated Strain data

In this thesis work, the simulated strain data is taken as the input. Simulated strain data is collected from the COMSOL platform based on the FEM model. Simulated strain data provides the actual strain information which can be taken as the base-line of the iteration method. For establishing optimization method this strain data works

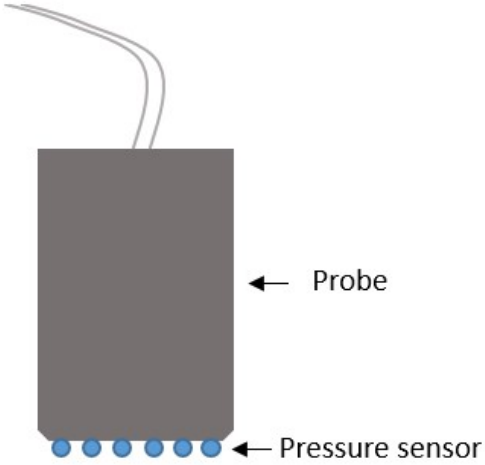

Figure 3.6: Ultrasound probe with pressure sensor.

as the reference. In practice, the strain data will face the problem with scattered noise and other sources of noise. Those sources of error will make the prediction system more challenging. Those challenges have been taken into account during the modulus prediction. Strain data is taken from the COMSOL platform to the MATLAB platform for further calculation.

3.5 Estimation of Stress and Modulus

Prediction of the stress value is dependent on the boundary condition. In this thesis, the lower boundary is kept bounded and fixed. Right and left side remains free. Figure 3.2 shows the geometry of the FEM for the simplified model. To collect the pre and post RF data, ultrasound probe will be used and at the top of the probe one pressure sensor matrix will be implanted in such a way so that the ultrasound transmitting and receiving signal do not have any distortion. From COMSOL, it is easy to realize the surface stress in each point. Practically, it is not possible to get continuous stress value for all the surface points but it is easy to get the stress value if we have at least a few stress values for different points by using interpolation. In COMSOL, a fixed displacement is created to simulate the pressure on the surface and the stress data is taken from the top surface.

From the FEM structure, the strain data is exported to the MATLAB for the whole structure. At first, it is a scattered data which is difficult to handle. So it is converted to matrix data for easier calculation. Based on the surface stress data and strain data, the modulus value is being predicted. For this, Hooke's law is the governing theory. In this phase, the surface stress value is taken as it is. All other stress values are calculated based on the surface stress and a certain percentage of change of strain value.

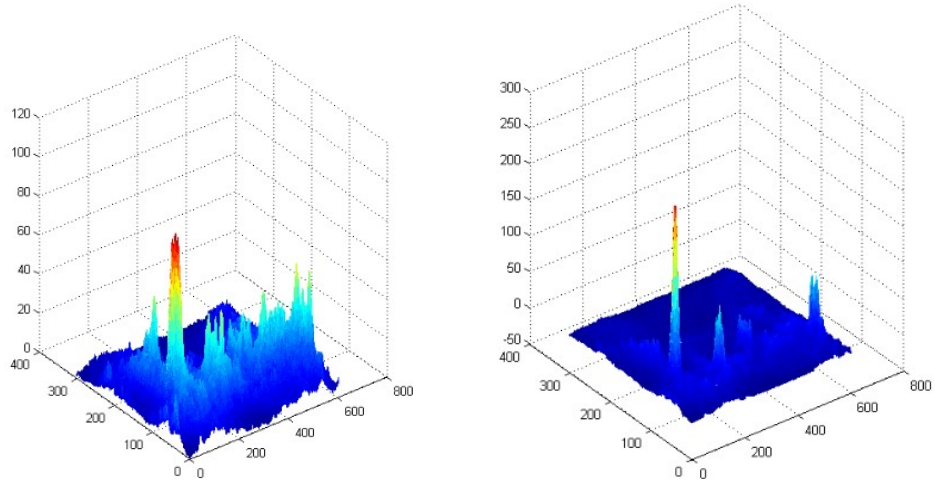

(a) (b)

Figure 3.7: (a) Predicted value without implementing Gaussian filter, (b) after implementing Gaussian filter.

$$\sigma^{i_0+1,j} = \sigma^{i_0,j} \times \alpha \times \left| \varepsilon^{i_0+1,j} - \varepsilon^{i_0,j} \right| \tag{3.5}$$

Equation (3.5) shows the stress prediction process based on the surface stress and the strain change. Here, $\sigma^{i_0,j}$ is the soft tissue surface stress, $\sigma^{i_0+1,j}$ is the predicted stress of the next row just under the top surface, α is the empirical percentage and $\varepsilon^{i_0+1,j}, \varepsilon^{i_0,j}$ are the two consecutive strains from the top, respectively.

It is been observed that due to the skin and the fat layer, the first predicted modulus values shows some mentionable errors. It is also important to mention that the stress value and the stress profile just under the fat tissue or to be very specific, on the top surface of the soft tissue are almost the same. So the top surface stress of the soft tissue is taken as the top surface for the calculation. This will help to give good prediction result from the very first step. For this reason, soft tissue along with the tumor is selected as the field of view for predicting modulus and updating the stress value.

3.5.1 Filtering Unwanted Modulus value

The modulus is calculated from the strain data, stress data of the soft tissue and predicted stress data. It is observed that there is some sharp changes in the first predicted modulus which is not practical. Different filtering options are tried and Gaussian filter is applied to resolve the unwanted predicted modulus problem [112]. This filter helps to smooth the predicted value. For the Gaussian filter, the standard deviation is taken as 1.

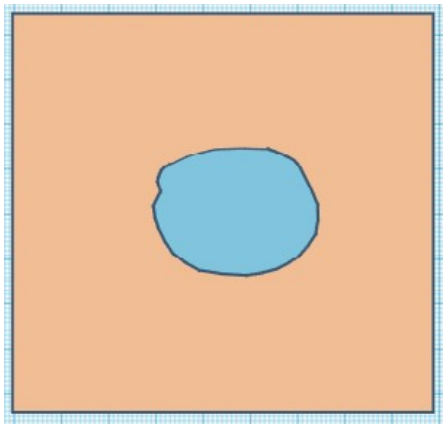

Figure 3.8: After implementing K-Means Clustering there are two distinct modulus.

3.5.2 Clustering Modulus values

In this phase, the adjacent modulus values are clustered by using the clustering algorithm which mostly provides two prominent areas since the tissue in consists example only of soft tissue and tumor. However, due to error in the prediction, there might be more distinct areas present as well. The number of unwanted areas depends on proper selection of the threshold value, clustering algorithm and matrix size. For this thesis, K-Means Clustering, Mean-Shift Clustering, Density-Based Spatial Clustering, Expectation-Maximization (EM) Clustering using Gaussian Mixture Models (GMM) and Agglomerative Hierarchical Clustering are tried [113]. The K-Means Clustering performs well for this purpose based on the error estimation which is shown in the next section with the result. All the values of each cluster are replaced by one modulus value which is calculated by taking the average of all those values under that cluster.

3.5.3 Updating stress value

Based on the cluster modulus data found in the MATLAB environment, FEM structure is created in the COMSOL for the first iteration. On that new model, the same amount of displacement is created on the top surface of the structure. Since this structure is created based on the predicted stress profile, it will not provide the actual strain distribution. Scattered strain data is imported to MATLAB again and converted to matrix data. This is the first error strain data. In this phase, the actual strain data is compared with the first error strain data. In the second iteration, the challenge is to predict the stress value for each point based on the previously predicted stress value and the first strain error distribution.

$$\sigma^{i,j} = \sigma^{i-1,j-1} \times \beta \times \left| \varepsilon^{i,j}_{actual} - \varepsilon^{i,j}_{error1} \right| \tag{3.6}$$

Here ,$\sigma^{i,j}$ is the new predicted stress value and is based on the previously predicted stress, $\sigma^{i-1,j-1}$ and a percentage of deviation of the strain value, β. Empirically, β should be selected to get less strain error in the next iteration and hence need less iteration to converge.

This newly predicted stress value along with the surface stress and actual strain distribution is taken as the input to find the next modulus distribution $(E_{predicted})$ based on the Hooke's law. After finding the predicted modulus in the second phase, the same Gaussian filter is applied to get the smooth modulus distribution. Using the K-mean clustering algorithm, modulus values are clustered and distinct regions are created. Each of the regions is presented by a single modulus value as done in the last phase. Now again, the FEM structure is created based on the modulus value found in the MATLAB platform. The same amount of displacement is applied on the top of the tissue structure and a new strain distribution is found ($\varepsilon^{i,j}_{error2}$). Then, the stress value is updated according to the equation (3.6) and this process is repeatedly done until it converges to a particularly targeted deviation, Δ. Here,

$$\Delta = \left| \varepsilon^{i,j}_{actual} - \varepsilon^{i,j}_{error(n)} \right| \tag{3.7}$$

where, n is the number of iteration needed to converge.

3.6 Various position, size and characteristics of the tumor

The experimental processes are applied for the various position, size and characteristics of the tumor. To get a targeted average deviation (Δ), for a different condition, an altered number of iteration is needed. Based on the number of iterations, the complexity of the structure is identified. Less iteration shows a more simple structure of predicting the modulus, whereas large iteration shows the complex structure. If the tumor is very close to the surface of the tissue structure, less number of iterations are needed. The output shows more complexity when the tumor moves to the lower part of the structure. Similarly, various size of the tumor shows its own characteristics. It's difficult to identify very small tumor whereas it is relatively easy to find the bigger tumor. Similarly, for different modulus values of tumor the prediction is examined and found that if the modulus is close to the background then it makes difficult to predict the tumor. The experimental setup also shows that after a certain level of pressure applied on the surface of the structure, it is difficult to identify the actual shape of the tumor. Figure 3.9- 3.10 are showing the background tissue with inclusion for the various size and position of the tumor.

For various parameters of the tumor, the reconstruction output will change. It is expected that inclusion close to the surface will give more accurate modulus prediction

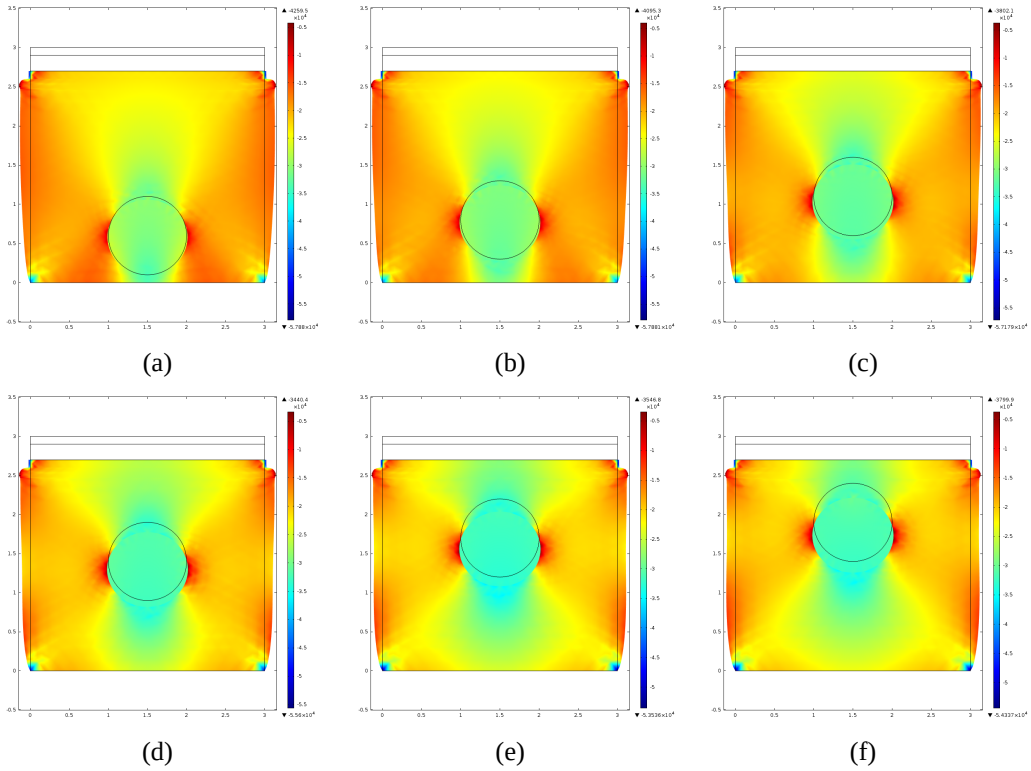

Figure 3.9: Stress distribution for different position of the tumor.

than compared to the inclusion in the depth. In the next section, the simulation result is presented and compared with different positions. Similarly, it is difficult to find out small inclusion from elastography imaging. On the other hand, bigger tumor has its large boundary. So it is expected that for a very small and large inclusion, the modulus reconstruction method will face challenges to get the satisfactory result.

It is important to analyze those aspects in order to find out the prediction error. The simulated result will give the guideline to test the proposed algorithm on the phantom data. In the simulated result, the strain distribution is very accurate. However, in real life, this strain distribution will be found from the pre and post-deformation US RF data. In any situation, accurate strain distribution data give advantage to predict a good modulus distribution.

3.7 Conclusion

In this thesis, surface stress is taken as the input for predicting the modulus of the tissue structure. Similarly, strain distribution is taken without considering the surface stress and based one this the modulus is predicted. For the same number of iterations the results are compared and always found a satisfactory result when the surface stress is considered. This comparison is presented in the next result section of the thesis. Other

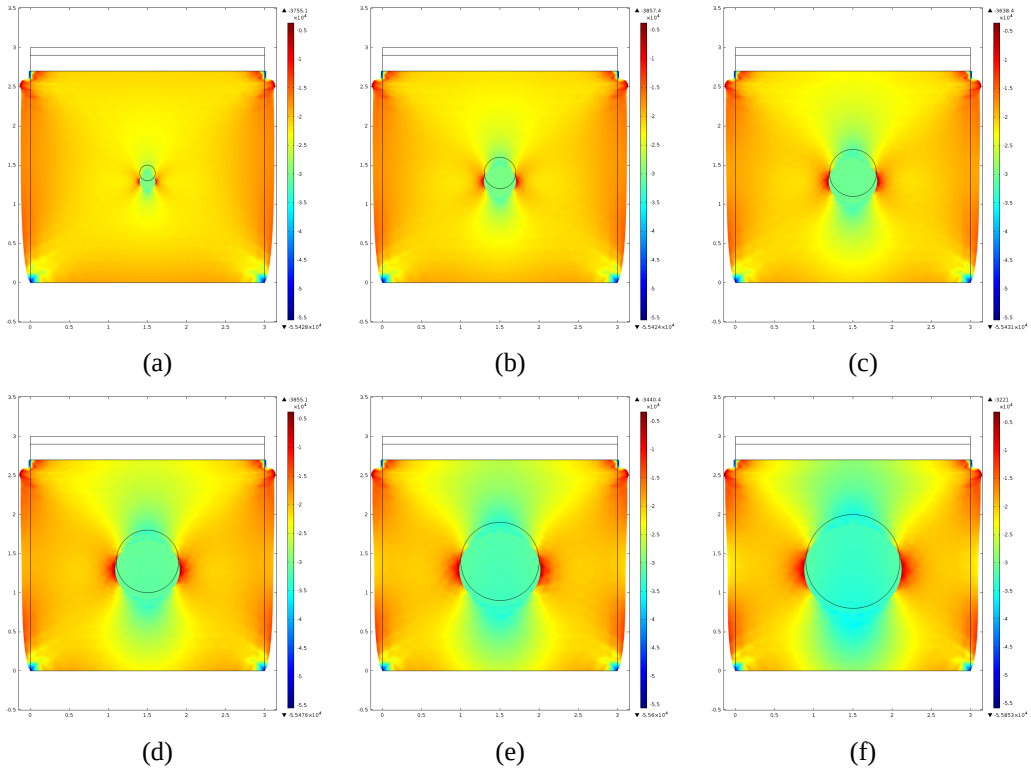

(a) (b) (c)

(d) (e) (f)

Figure 3.10: Stress distribution for different size of the tumor.

comparisons considering the different positions, sizes and characteristics of the tumor are also presented in the result section.

Chapter 4

Findings and Validation

4.1 Introduction

The tissue structure proposed in the chapter 3, is validated with the research outcome compared to the experimental data of this thesis [114]. Water is the selected material used to represent various parts of the model. Distinctions were made between soft tissue, tumor, skin and fat by varying the mechanical properties. The altered properties included the Poisson's ratio and Young's modulus according to the literature [11]. Poisson's ratio is the ratio of the proportional decrease in a lateral measurement to the proportional increase in length in a sample of material that is elastically stretched. Young's modulus is a measure of the ability of a material to withstand changes in length when under lengthwise tension or compression. Sometimes referred to as the modulus of elasticity, Young's modulus is equal to the longitudinal stress divided by the strain. Poisson's ratio is taken as 0.495 for soft tissue, tumor, skin and fat. Young's modulus is considered as 10 kPa, 40 kPa, 200 kPa and 1.5 kPa for soft tissue, tumor, skin and fat respectively. It is assumed that bone is at that side. All the other sides were left free for movement. A model of breast tissue is created using COMSOL Multiphysics software. COMSOL Multiphysics is a cross-platform finite element analysis, solver and multi-physics simulation software [111]. It allows for the creation of a conventional physics-based user interface. The size of the overall model is taken as 3 cm with and 3.6 cm depth. The tumor is modeled by 1 cm diameter circular structure and placed in different positions for analysis. Skin and fat tissue depth are taken as 0.1 cm and 0.5 cm respectively where the width is 3 cm.

In the experiment phase, it is found that the surface stress on the top surface is almost equal to that of the stress distribution just under the fat tissue for the region of interest (ROI). Figure 4.1 shows the stress profile along the surface and the surface of the soft tissue for both the whole width and as well as for the ROI section. If the surface stress is taken as the direct input for modulus prediction, it produces some unwanted modulus value in different spaces of the tissue. Since the pattern and the value of the

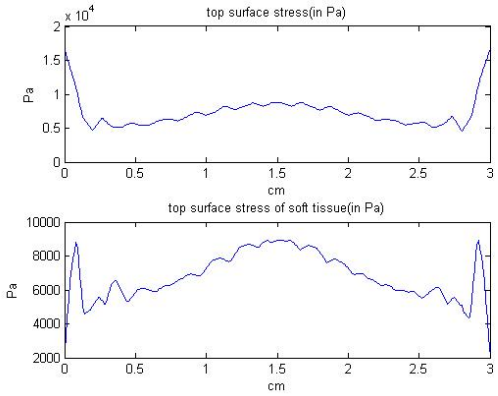

(a)

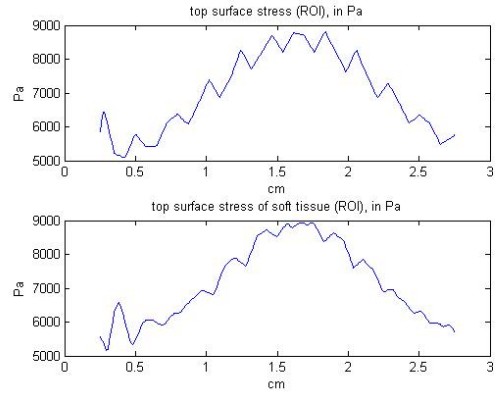

(b)

Figure 4.1: Stress distribution along to the surface of the structure and to the surface of the soft tissue. (a) Showing the full width, (b) showing the ROI section only.

surface stress is almost equal to the stress distribution just under the fat, it is effective to consider the top surface tissue (soft tissue) stress as the direct input and is considered as the equivalent of the surface stress.

In this chapter, different evaluation and validation processes are described with the result and shown with diagrams, tables and plots. The stress distribution is collected from the COMSOL and saved as .xlsx file. This data is in scattered format rather than in matrix format. By using MATLAB, this scattered data is converted to matrix distribution. It helps to find out the specific point of interest and doing all the manipulations.

4.2 With and without considering surface stress

In case of conventional elastography imaging, the compression pressure or stress is not considered for modulus reconstruction. Mostly in strain imaging, only the strain data is considered to get an idea of the distribution of the variation of the modulus. In this thesis, surface stress made by the ultrasound probe is taken as the additional informa-

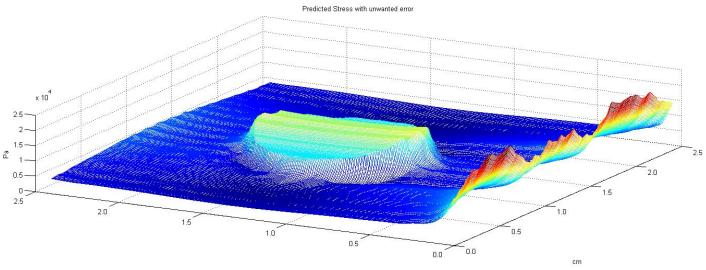

(a)

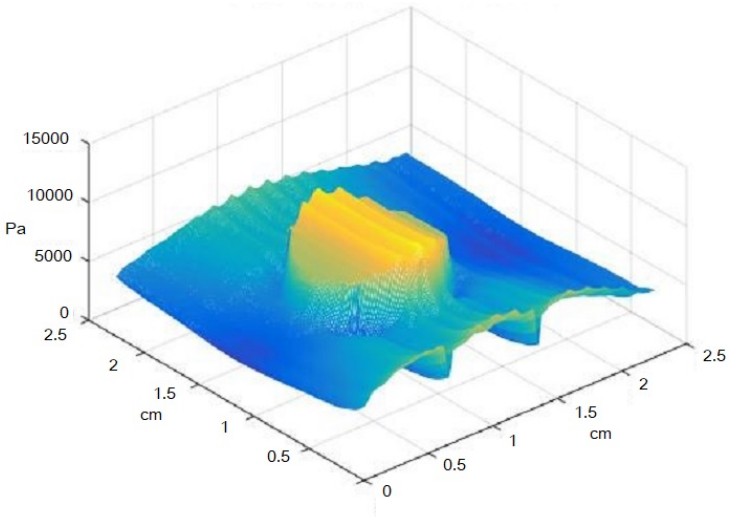

(b)

Figure 4.2: Predicted stress distribution with error due to skin and fat layer. (a) Showing the full view and (b) showing the ROI view.

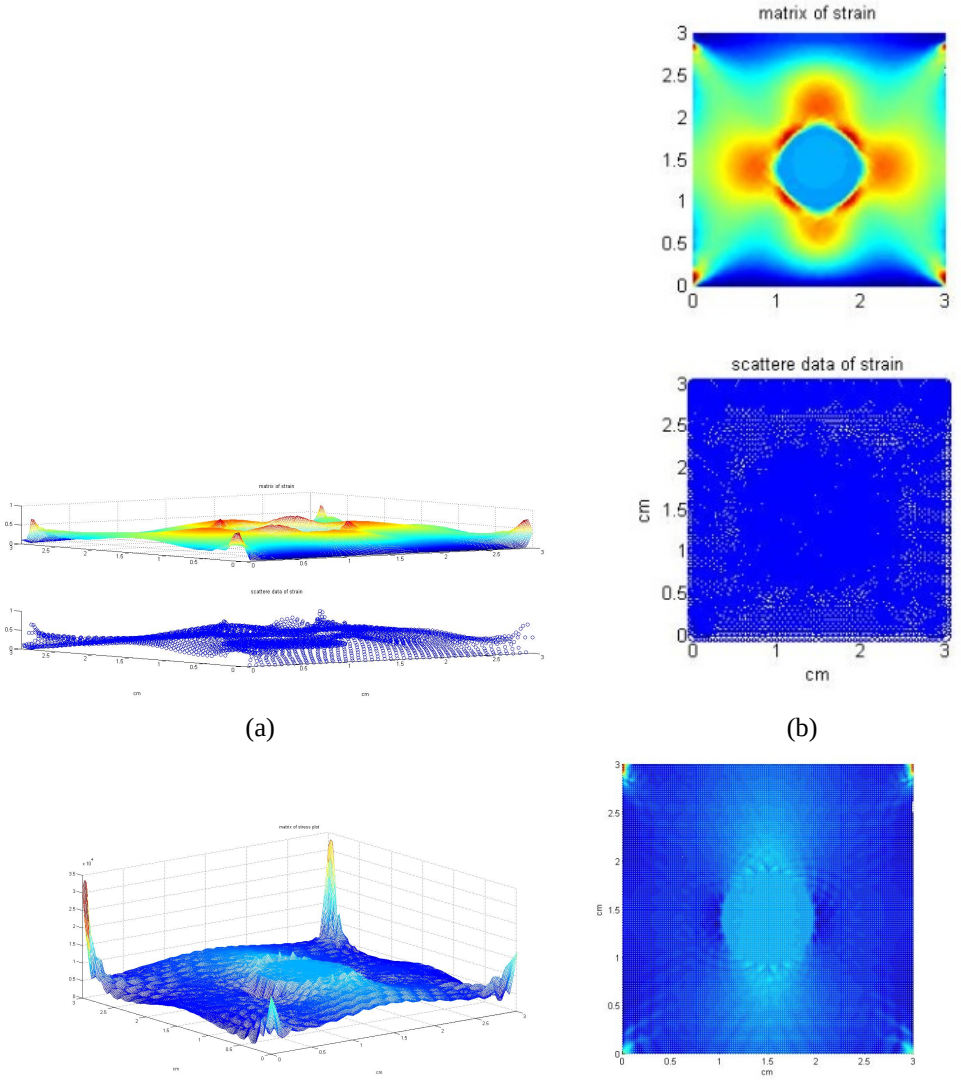

Figure 4.3: (a) and (b) shows the scattered and matrix view of the strain distribution, (c) and (d) shows actual stress distribution.

tion to predict the stress distribution, hence to predict the modulus. In COMSOL, a fixed displacement is created to simulate the pressure on the surface and the stress data is taken from the top surface. From the FEM structure, the strain data is exported to the MATLAB for the whole structure. At first, it is a scattered data which is difficult to handle. So, it is converted to matrix data to make the calculation easy. Based on the surface stress data and strain data, the modulus value is being predicted. For this, Hooke's law is the governing theory. In this phase, the surface stress value is taken as it is. All other stress values are calculated based on the surface stress and a certain percentage of change of strain value as stated in equation (3.4).

It is observed that due to the skin and the fat layer, the first predicted modulus values suffers form mentionable errors. It is also important to mention that the stress value and the stress profile just under the fat tissue or to be very specific, on the top surface of the soft tissue are almost the same which is mention in the last section. So the top surface stress of the soft tissue is taken as the surface stress. This will help to give good prediction result from the very first step. For this reason, soft tissue along with the tumor is selected as the ROI for predicting modulus and updating the stress value.

For calculating the modulus distribution, this predicted stress based on the surface stress and strain distribution is taken. It is observed that there are some sharp change in the first predicted stress distribution which is not practical. Different filtering option is tried and Gaussian filter is applied to resolve the unwanted predicted modulus problem [112]. This filtering helps to smooth the predicted value. For the Gaussian filter, the standard deviation is taken as 1 empirically.

First stress distribution is predicted based on the equation (3.4), where α has to select. For the value of $\Delta \leq 5\%$ and setting the β as 30%, the value of α is varied from 10% to 100%. That refers to the range of the α from 0.1 to 1.0. The lowest number of iteration to achieve the targeted Δ is done by setting α equals to 0.5 (50%). If the α value is increased or decreased, the iteration number need to be increased to achieve the targeted mean error value. Figure 4.4 shows the relation between the different value of α and number of iteration to catch the targeted mean error as less or equal to 5%. So it is reliable to select the value of α as 0.5 for this experiment. According to the Hookes law, modulus distribution is calculated. This ends the first iteration. For the second step, the distribution of the first predicted modulus value is clustered by using K-mean clustering algorithm and two distinct areas are selected for the next processing in COMSOL. Here each cluster is filled with the average value of that cluster which represents the modulus value input for the next iteration.

For the next iteration, this structure is taken as the input of the COMSOL where the same amount of displacement is applied on the top of the surface. The strain value

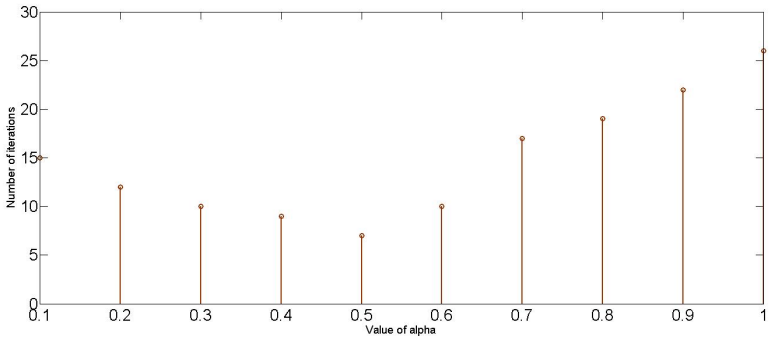

Figure 4.4: Number of iteration needed for different α.

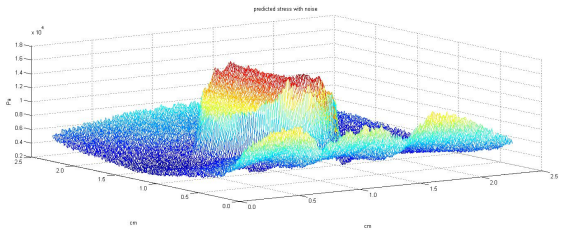

(a)

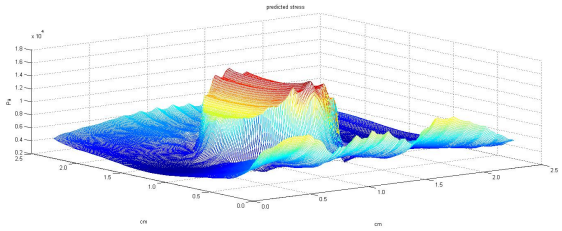

(b)

Figure 4.5: (a) First predicted stress with noise, (b) first predicted stress by applying Gaussian filter.

is exported to MATLAB for next step calculation. At this stage, the stress value is updated based on the equation (3.5) where β is taken as 0.3 or 30%. For the value of $\Delta \leq 5\%$ and and setting the α as 50%, the value of β is varied from 10% to 100%. That refers to the range of the β from 0.1 to 1.0. The lowest number of iteration to achieve the targeted Δ is done by setting β equals to 0.3 (30%). If the β value is increased or decreased, the iteration number need to be increased to achieve the targeted mean error value. Figure 4.7 shows the relation between the different value of β and number of iteration to catch the targeted mean error as less or equal to 5%. So it is reliable to select the value of β as 0.3 for this experiment.

The predicted modulus is calculated as in the first step. This completes the second iteration. The same steps are followed as long as the deviation of the strain distribution (Δ) is equal to or less than a certain level. In this case, Δ is taken as 1% which leads the modulus average error less than 4%. Figure 4.8- 4.10 shows all the outputs found

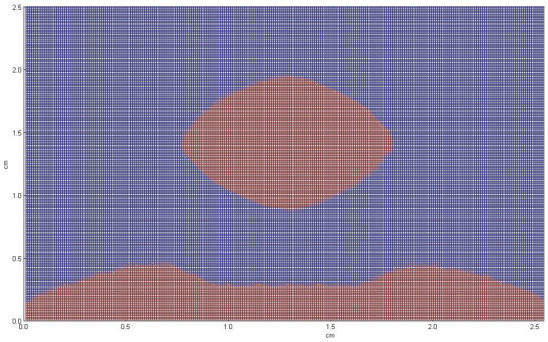

(a)

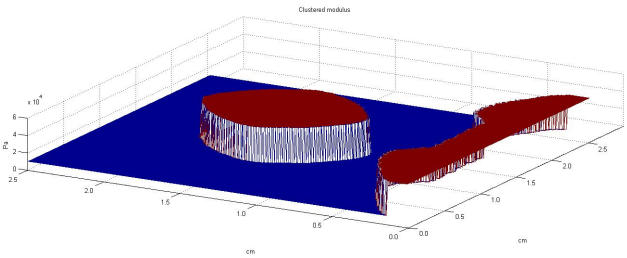

(b)

Figure 4.6: Clustered modulus value using K-mean algorithm. Each area is filled by the average value of that cluster.

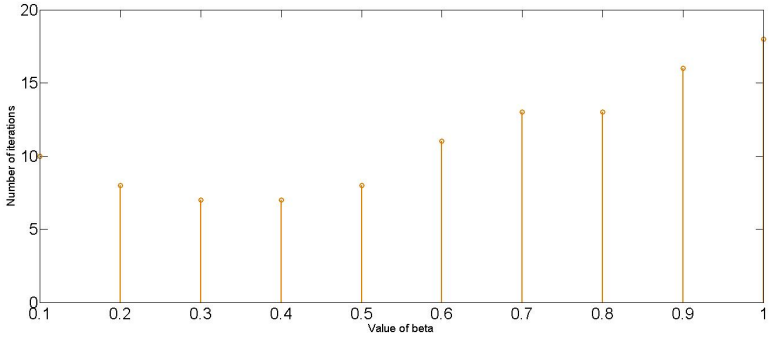

Figure 4.7: Number of iteration needed for different β.

during those iterations. For this example, it takes ten iterations to reach the Δ to 1%.

The same process is executed for the same tissue structure but the surface stress is not considered now. In this case, the initial stress distribution is considered as a constant value and taken as 10,000 Pa [115]. Ten iterations are allowed for this modulus prediction since by using the proposed novel algorithm, less than 1% error is reached by ten iterations. Figure 4.11 represents the percentage of error of modulus comparing between the actual and predicted modulus in each iteration for both considering surface stress and just taking a constant stress distribution at the beginning.

It is very significant that when the surface stress is considered, then the prediction error becomes very close to 5% by only 6 iterations. After that only 2% error lessens

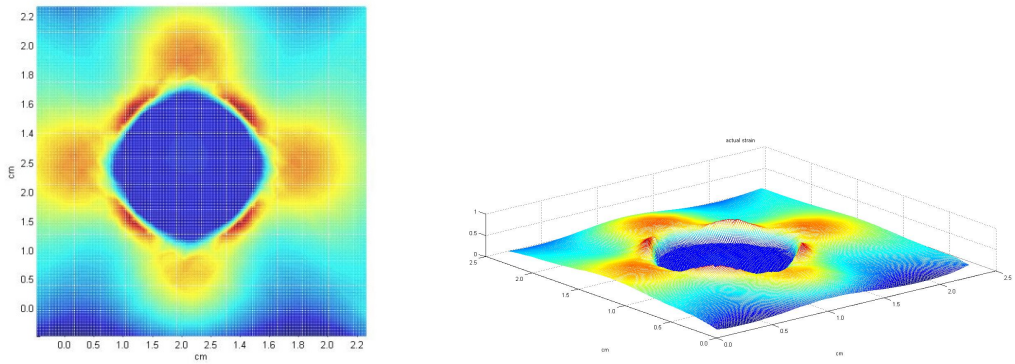

(a) (b)

Figure 4.8: (a) Top view of actual strain, (b) 3D view of actual strain.

for next 4 iterations. If 5% error is satisfactory, then only 6 iteration is enough for the final modulus prediction which will save a substantial time for reconstruction. As, this is a very time-consuming process, it may consider for practical evaluation purpose. On the other hand, while surface stress is not considered, it provides a huge error for first 4 iterations. However, after 8^{th} iterations, it gives a very constant error which is around 10%.

4.3 Considering different position

The same processes are applied to the same tissue structure where only the tumor changes the position in the axial direction. All the other parameters remain constant as mentioned in the last section. For all the different positions of the tumor, 10 iterations are done rather making Δ value fixed. It is always shows the possibility of getting the less prediction error for more iteration. However, number of iterations will take much time to complete the process.

It is completely visible from the Figure 4.12 that for all the iteration points, the predicted modulus yields a better result for those tumors which are closer to the upper surface of the structure. Here the position is varied from 1.2 cm to 2.2 cm from the top surface of the tissue structure. It is observed that, after ten iterations, the percentage of error converge to around 3.25% to 6% which is quite acceptable.

4.4 Considering different size

The same processes are applied as discussed in section 3.2 for the same tissue structure where only the tumor size is changed. All the other parameters remain constant as mentioned in section 3.2. For all the different positions of the tumor, 10 iterations are

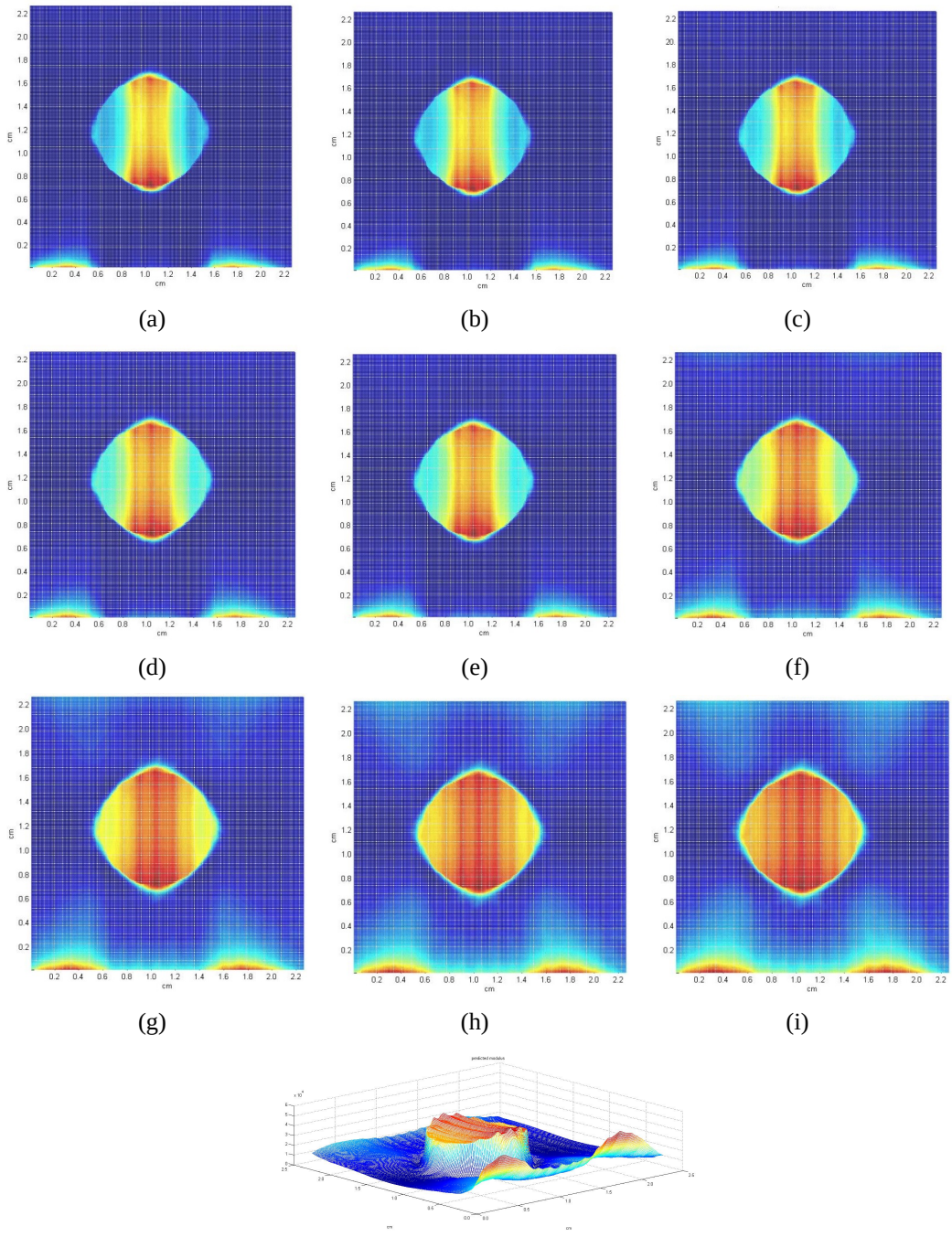

Figure 4.9: (a) to (i) shows first to ninth iterated predicted modulus distribution respectively, (j) is the 3 D view of the ninth iterated predicted modulus distribution.

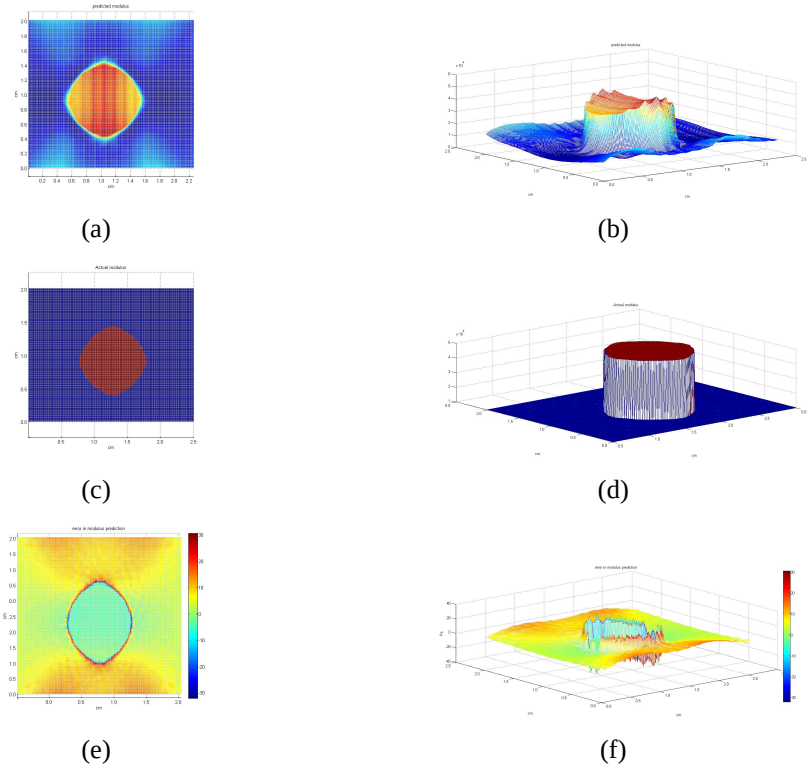

Figure 4.10: (a) and (b) is the predicted modulus distribution for $\Delta \leqslant 1\%$, (c) and (d) is the simulated modulus found from FEM model, (e) and (f) showing the error of modulus prediction.

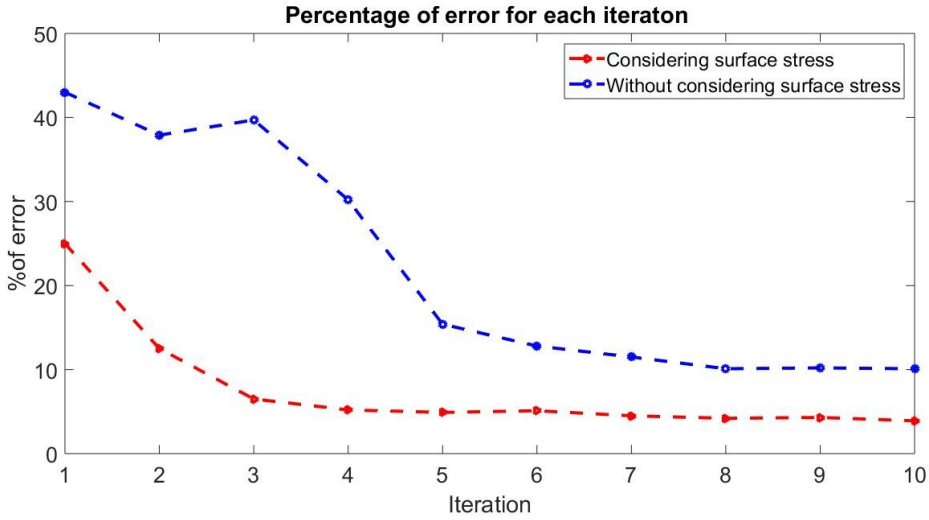

Figure 4.11: Comparison of error in percentage of the modulus prediction for considering and without considering surface stress.

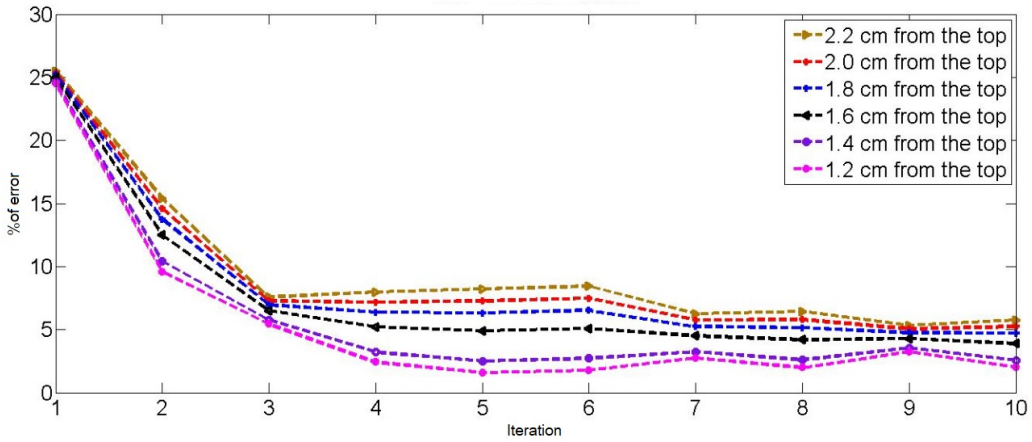

Figure 4.12: For the first ten iteration, percentage of error for different position of the tumor.

done rather making Δ value fixed. The size of the tumor is changed to 0.6 cm to 0.1 cm radius. In all the cases the tumor is fixed in the center of the soft tissue.

Form the Figure 4.14, it is very significant to observe that the higher percentage of error is formed from the tumor of 0.1 cm and 0.6 cm radius. On the other hand, the lowest percentage of error is achived from the tumor of 0.3 cm radious and the second lowest from 0.4 cm radius based tumor which shows that the prediction algorithm produces a better result for a certain size of the tumor, whereas a larger or smaller size tumor may face challenges. This result is logical since in case of the large tumor, though the visibility is increased the boundary length of the tumor and soft tissue is also increasing. The boundary area suffers to predict the stress distribution hence the modulus distribution.

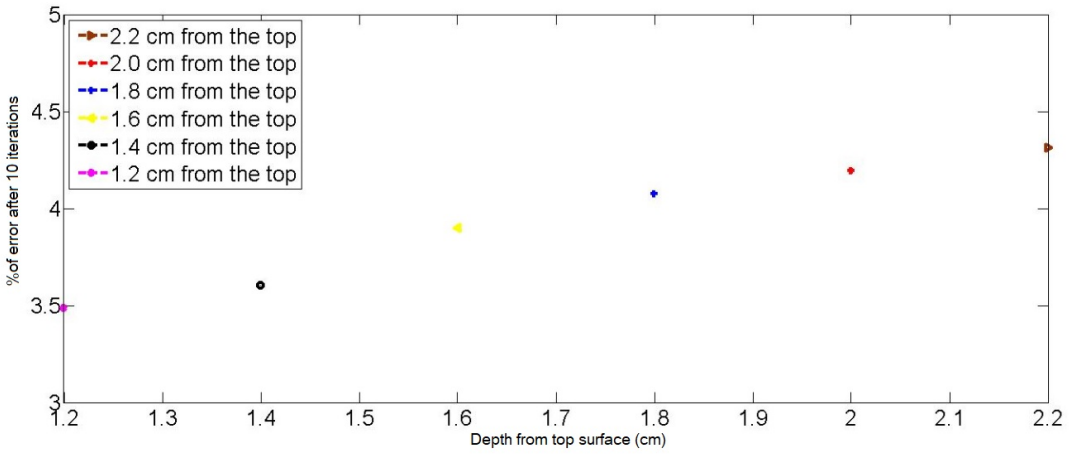

Figure 4.13: After the 10^{th} iteration, the percentage of error in modulus prediction for different depth.

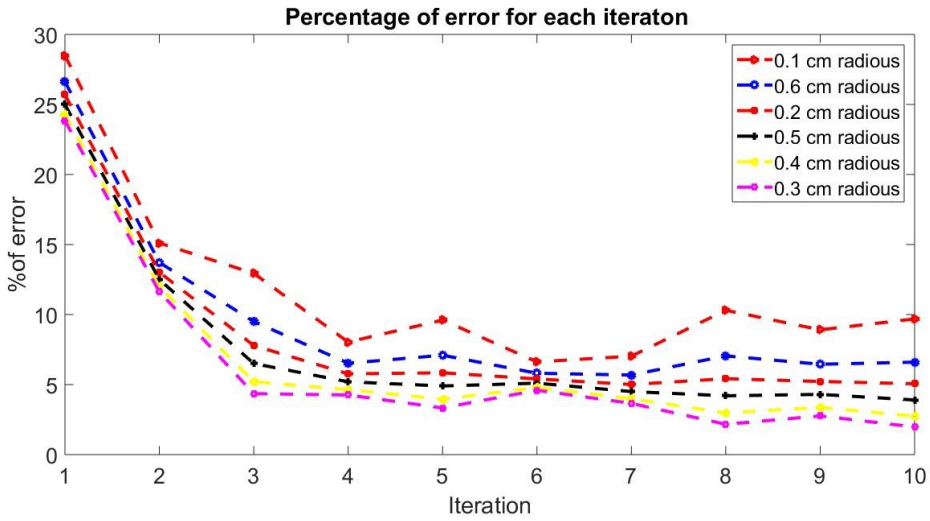

Figure 4.14: For the first ten iteration, percentage of error for different position of the tumor.

4.5 Considering mesh size of the structure

By using COMSOL software, the FEM simulation is carried out for this thesis. In real life, the strain data will be calculated from the pre and post-compression data and the surface stress data will be collected from the sensors. After that the processing will depend on the COMSOL software capabilities and manipulation. The most significant part of the manipulation is from the point of view of mesh size. It is possible to control the mesh size when the tissue structure is designed. The modulus value for each cluster is calculated from MATLAB for the first iteration. After that, the model is built in the COMSOL environment. In this phase, the mesh pattern is being selected. It is possible to select Extremely fine, Extra fine, Finer, Fine, Normal, Coarse, etc. pattern. The important thing is the mesh size can be controlled in the design process. Finer mesh

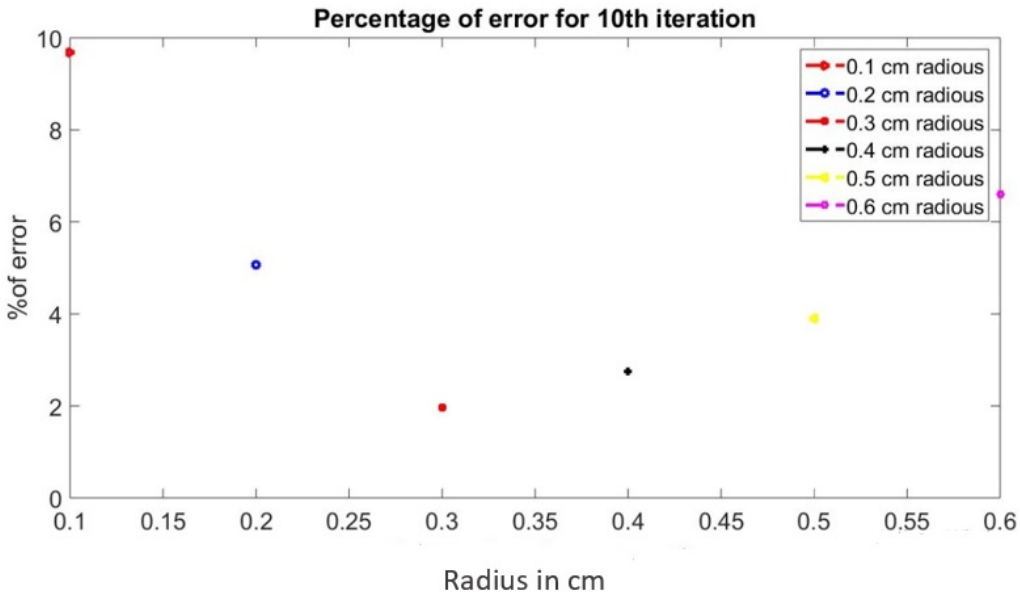

Figure 4.15: After the 10^{th} iteration, the percentage of error in modulus prediction for different size of the tumor.

will force to take longer time for calculation and that is the limitation. In this section, the percentage of modulus error is calculated based on the pattern of the mesh.

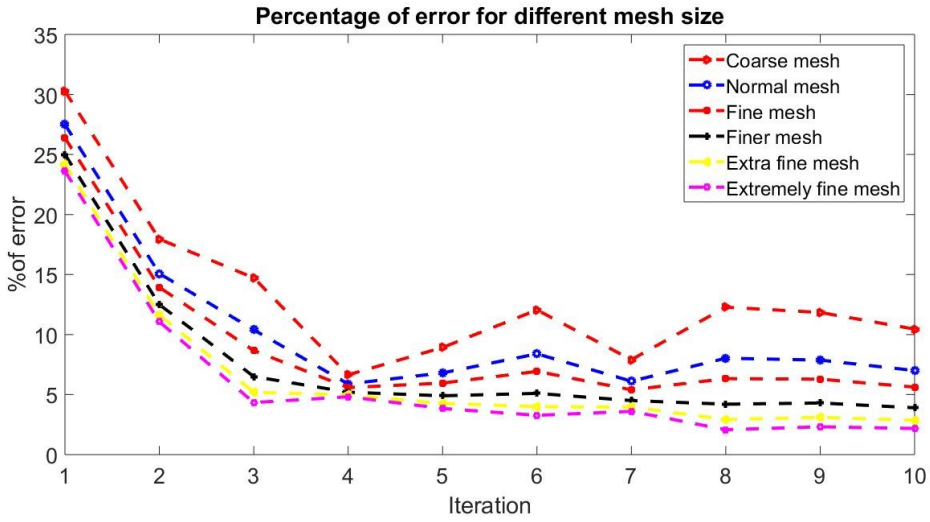

Figure 4.16: For the first ten iteration, percentage of error for different mesh type.

The performance differs for different mesh types. So, it is a tradeoff between the computation time and precise prediction of modulus distribution. Figure 4.16 shows the complete variation of the percentage of error produced in each iteration for different mesh type. This experiment is conducted for the same tissue structure.

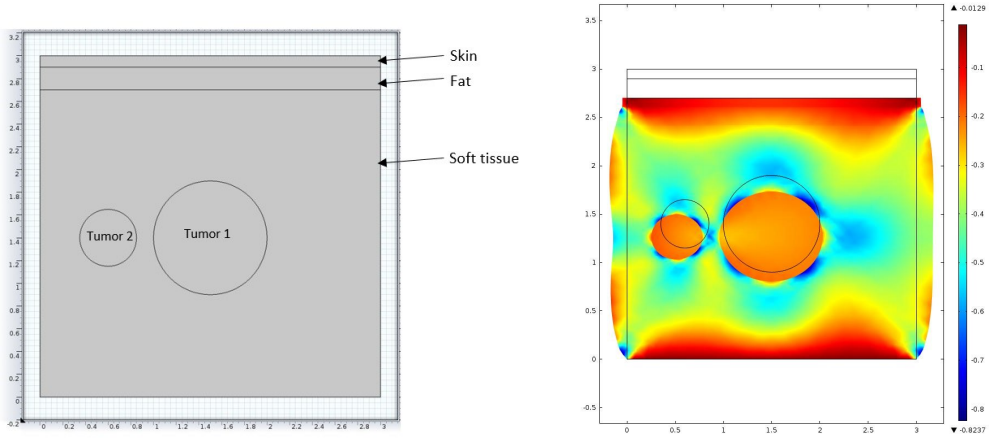

(a) (b)

Figure 4.17: (a) Tissue structure with two tumor with same characteristics, (b) strain distribution of the structure.

4.6 Considering multiple tumors

For making the understanding clear for the multiple tumors, only two tumors are simulated inside the soft tissue as shown in Figure 4.17. One of the tumors has half the radius than that of the other. Two of them have the same depth and same nature. That means both of the tumor have the same modulus value (40 kPa) and poison ratio (0.495).

For the above mentioned structure, the same processes are applied as mentioned in section 4.2. The percentage of error is calculated for first ten iterations for the multiple tumors in the same manner described as for the single tumor (larger one only). Figure 4.19 represents the comparison between the patterns of the percentage of the error of predicted modulus.

From the performance of the multiple tumor prediction, it can be mentioned that the novel algorithm stated in this thesis is very much capable to predict the modulus for multiple tumors as well. The percentage of error for the multiple tumor is only 7.5% [116]. The performance can be improved by implementing more iterations for multiple tumor case. It will take a longer time to complete the process but it will give more accurate prediction. Figure 4.17 shows the comparison between the modulus prediction between two different and same sized tumor. It is clearly observed that, the size of the tumor makes a minor effect to the modulus prediction.

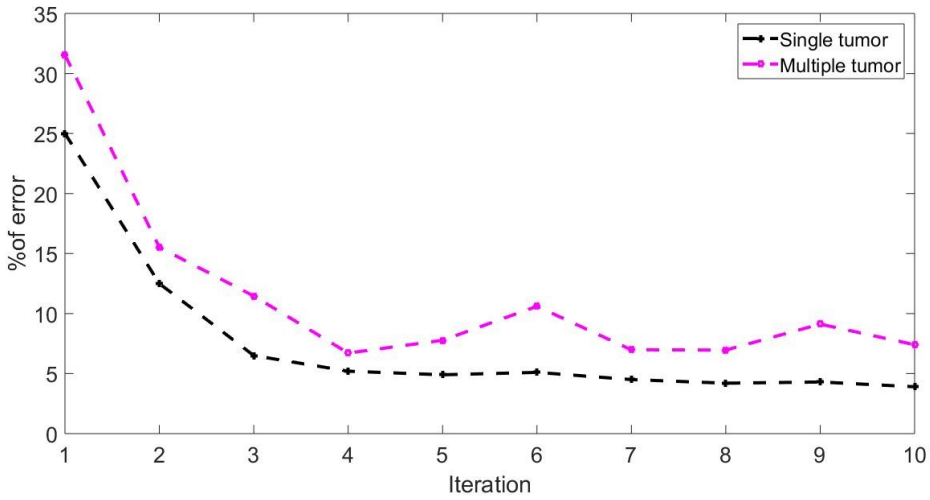

Figure 4.18: For the first ten iteration, percentage of error for different modulus value of the tumor.

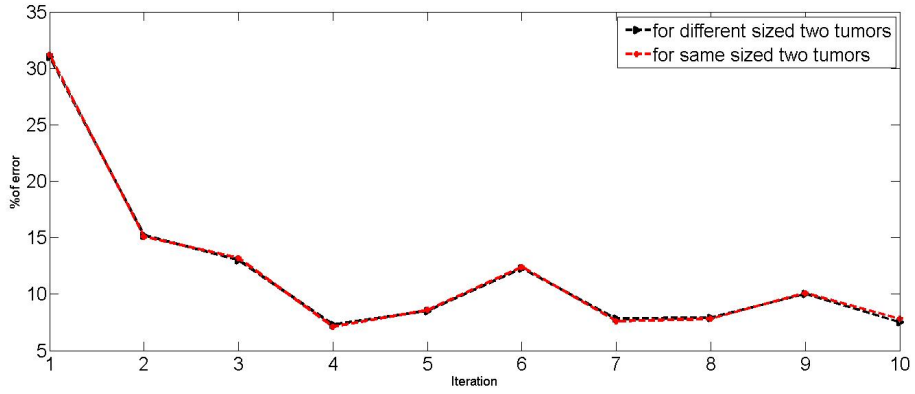

Figure 4.19: Percentage of error for the tumors having different and same size.

4.7 Considering different modulus value

For all the experiment, the modulus of the tumor and the soft tissue is taken as 40 kPa and 10 kPa respectively. At the early stage of the cancer tumor, the modulus value is very close to the surrounding soft tissue. So, it is important to examine the proposed algorithm under the different value of tumor modulus starting from very similar value of soft tissue to 40 kPa. Here, the tumor's modulus is taken as 15 kPa, 20 kPa, 30 kPa and 40 kPa for comparing the effect of the modulus prediction complexity due to the variation of the modulus distribution.

As the modulus value is closer to the background tissue, the prediction algorithm faces challenges. However, the proposed algorithm still shows satisfactory modulus distribution prediction.

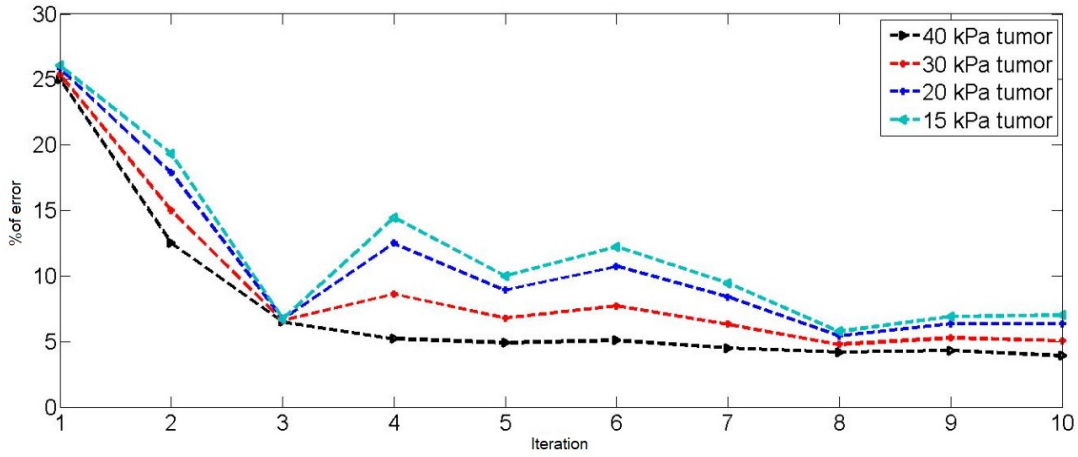

Figure 4.20: For the first ten iteration, percentage of error for different modulus value fo the tumor.

4.8 Validation with tissue mimicking phantom study

The proposed estimation method is validated with two tissue mimicking phantom studies of S. R. Mousavi $et.\ al.$ [2] which practically use two phantoms where the dimension and the deformation data is given. According to those phantoms, the simulated tissue structure is built and the proposed algorithm is run on those structure to validate this proposed algorithm. S. R. Mousavi $et.\ al.$ consisted of two parts in the phantom which mimics the breast and tumor tissues. The phantom used in the first study had a simple block-shape geometry while the one used in the second study had a more complex breast-like geometry. These two phantoms are illustrated in Figure 4.21 [115]. The first phantom is manufactured by the Computerized Imaging Reference Systems (CIRS; Pacific Northwest X-ray Inc., Gresham, USA). A mechanical device along with the US probe was used for compressing the phantom with 0.3 cm. The second phantom is constructed using gelatin and agar dissolved in water. A few drops of formaldehyde were added to the dissolved gelatin and agar to increase the melting point of the mixture and increase the phantom's resistance against developing mould. Also, glycerol is added to the mixture to regulate the ultrasound wave speed in both the normal and tumor areas such that the wave speed is approximately 1540 m/s [115]. All the materials used to construct the phantom are manufactured by Sigma-Aldrich Co. LLC. To have better image contrast between normal and tumor areas, different concentrations of Sigmacel are added to the batch prepared for each tissue type to create nonuniform backscattering. Indentation is conducted using an apparatus consisting of a load cell along with a linear servo actuator and a computer controller. The actuator is equipped with a circular plane-ended indenter.

The modulus of the inclusion and the background tissue for the first phantom are

Table 4.1: Comparison with the recent published experimental data to the predicted modulus value.

	YM ratio between inclusion over background (actual)	YM ratio between inclusion over background (S. R. Mousavi et. el. [2])	% of error by applying recent algorithm (S.R. Mousavi et. el. [2])	YM ratio between inclusion over background (applying proposed algorithm)	%of error by applying proposed algorithm
First phantom	1.70	1.86	9.41%	1.68	1.17%
Second phantom	1.60	1.49	6.87%	1.56	4.69%

Table 4.2: Comparison with the actual phantom data to the predicted modulus value.

	Inclusion modulus (actual)	Inclusion modulus (applying proposed algorithm	% of error for inclusion modulus prediction	Background modulus (actual)	Background modulus (applying proposed algorithm)	% of error for background modulus prediction
First phantom	56 kPa	57.9 kPa	3.39%	33 kPa	34.320kPa	4%
Second phantom	40 kPa	41.3 kPa	3.20%	25 kPa	26.4 kPa	5.6%

56 kPa and 33 kPa (E_{inc}/E_{bkg} =1.70), respectively. By using the proposed algorithm the modulus of the inclusion and the background tissue is found as 57.9 kPa and 34.32 kPa respectively. This implies the inclusion modulus over the background tissue modulus is equal to 1.687. S.R. Mousavi $et.\ al.$ [2] found this inclusion to background YM ratio is equal to 1.86. It implies 9.41% error comparing with the actual phantom data. Proposed algorithm shows the same error as 1.17%. Similarly, for the second phantom, the modulus of the inclusion and the background tissue and the background tissue are 40 kPa and 25 kPa (E_{inc}/E_{bkg} =1.6) respectively. By using proposed method those moduli are found as 41.3 kPa and 26.4 kPa (E_{inc}/E_{bkg} =1.56.4), respectively. It implies the error comparing to the actual data as 4.69%. On the other hand, recent publication [115] can achieve 6.87% error. In any concern, the proposed algorithm presents better output compared with the recently developed algorithm. Table 4.1 and table 4.2 represent the performance of the proposed algorithm.

4.9 Conclusion

The result in the validation phase shows the strength of the proposed algorithm. A number of cases are considered and shown with the predicted modulus with the error. For each case, the result shows a potential outcome. There are some other cases which may be consider for rigorous analysis. For all the simulations, the isotopic behavior is considered but for the real environment all the soft tissue, tumor, skin and fat could be considered as anisotropic which will add more complexity to the structure and hence the proposed algorithm will face challenges. Overall, the proposed algorithm can successfully predict modulus value for tumor and the background tissue just by knowing strain distribution and the surface stress of the structure.

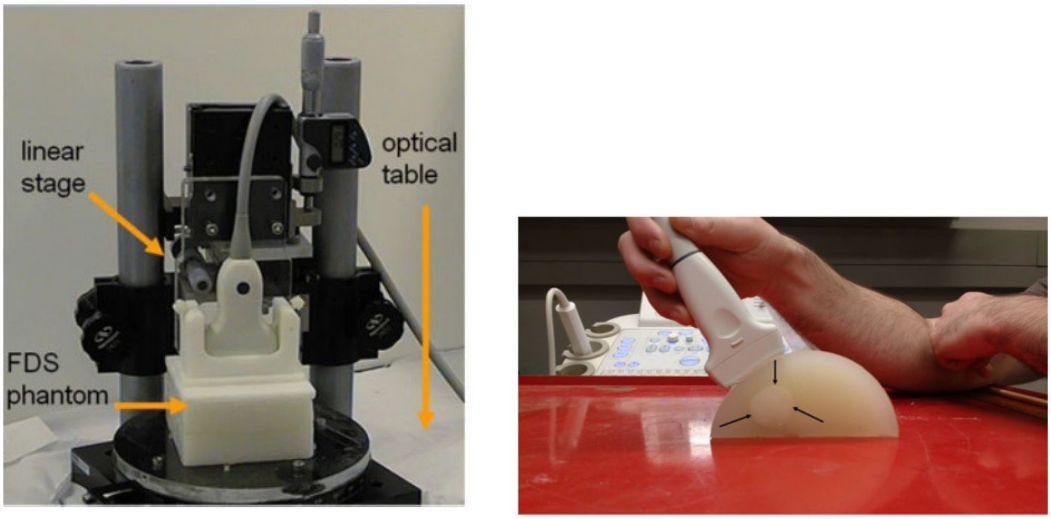

(a) (b)

Figure 4.21: Block-shape (left) and cylindrical (right) tissue mimicking phantoms consisting of an inclusion (indicated with 3 arrows) mimicking the tumor [2].

Chapter 5

Semi-automated Elastography Best Frame Selection

5.1 Introduction

Breast tumour is one of the significant causes of cancer for women. Different medical imaging techniques are used to identify breast tumour and they have their own characteristics. Ultrasound B-mode image is one of the imaging techniques by which the tumour can be detected and characterized. However, in several cases, it is not possible to locate the tumour by using only B-mode image analysis. Elastogram or strain imaging provides one further step of information to identify the malignant tumour. Each frame of the video does not have good tumour visibility in case of elastogram image. It is difficult and time consuming for a doctor to accurately detect the shape of the tumour from rapidly changing frames. Selecting the frames where the tumour is comparably more visible will help the doctor/radiologist to detect the tumour more easily.

In this dissertation, a method of semi-automated best frame selection from a strain video is proposed. The method involves two ways to select the required frames and to show the best output frames in the form of a video. It is based on Mean Pixel Difference (MPD) and Gray-Level Co-occurrence Matrix (GLCM) contrast as the image descriptors. The accuracy is also calculated by comparing it with the human visibility to the automated selected frame. Few structural and statistical methods are tied to find the quality of the image. Structural methods produce results with uncorrelated value for image quality in case of US image. On the other hand statistical methods works well for US image. Mean pixel Difference (MPD) and Grey Level Co-occurrence Matrix (GLCM) are two most popular methods for specifying the texture, especially for the gray level image.

In the earlier chapter, the modulus reconstruction method is described and the novel algorithm is proposed. It is found that by using proposed algorithm, the modulus reconstruction can be improved. However, the best frame from the elastogram sequence is still demanding to find out the best possible output in the shortest period of time. It

will give more confidence to the doctor/radiologist. After getting the best frame, it will be easy to set up to find the tumour boundary. The signal that is found directly from ultrasonography is actually RF signal. From the envelop of the RF signal, A-mode image is found. Then the A-mode image is converted into a 2D greyscale image known as B mode image. In many cases, the tumour cannot be detected from B-mode image, especially in the early stage of a malignant tumour. As these types of tumour have no specific shapes and cannot be easily differentiated from the surrounding breast tissue, B-mode image is less effective to detect the shape and size of the tumor. However, by applying pressure over the area helps to obtain the strain image and, in these cases, strain image may provide a better view of the tumour [85]. If the predicted stress data is available then the predicted modulus distribution is also available for diagnosis.

Strain is found from the difference between the pre and post compression ultrasound images [85]. As the tumour is comparatively denser than the surrounding tissue, applying pressure does not change the shape of the tumour that much. If we calculate the strain of the tumour, the change of the surrounding tissue is at a much greater scale than the tumour, which can be shown in the strain images. So, the tumour is more visible in the difference image. The strain images from the radiologist are given in the form of image sequences. Not every frame of the sequence provides a good visibility of the tumour. Because of human error, while applying pressure during ultrasonography, some frames of strain video may include more noise and the tumour may not be visible in these frames. It is a troublesome process for a doctor/radiologist to go through each and every frame and to find out the best frames based on the tumour visibility. In this chapter, a robust and effective best frame selection method is proposed. This method consists of four steps. The first step extracts the frames from the sequence. The second step pre-processes the frames to make them smoother and enhanced by reducing the speckles and noises. The third step categorises the frames according to the tumour visibility using Mean Pixel Difference (MPD) and GLCM (contrast) [3] methods as the image descriptor. The energy, homogeneity, and contrast of healthy and malignant cells of the GLCM features are significantly distinctive [11]. The final step creates a sequence with the best frames.

5.2 Methods

Figure 5.1 depicts the algorithm of our proposed method. The method can be divided into four major parts namely, Extracting frames, Pre-processing, applying MPD and GLCM, sorting and creating a video. According to the proposed method, the steps to select the best frames from a strain video are as follows:

Extracting frames from the video: Form pre and post compressed breast US data,

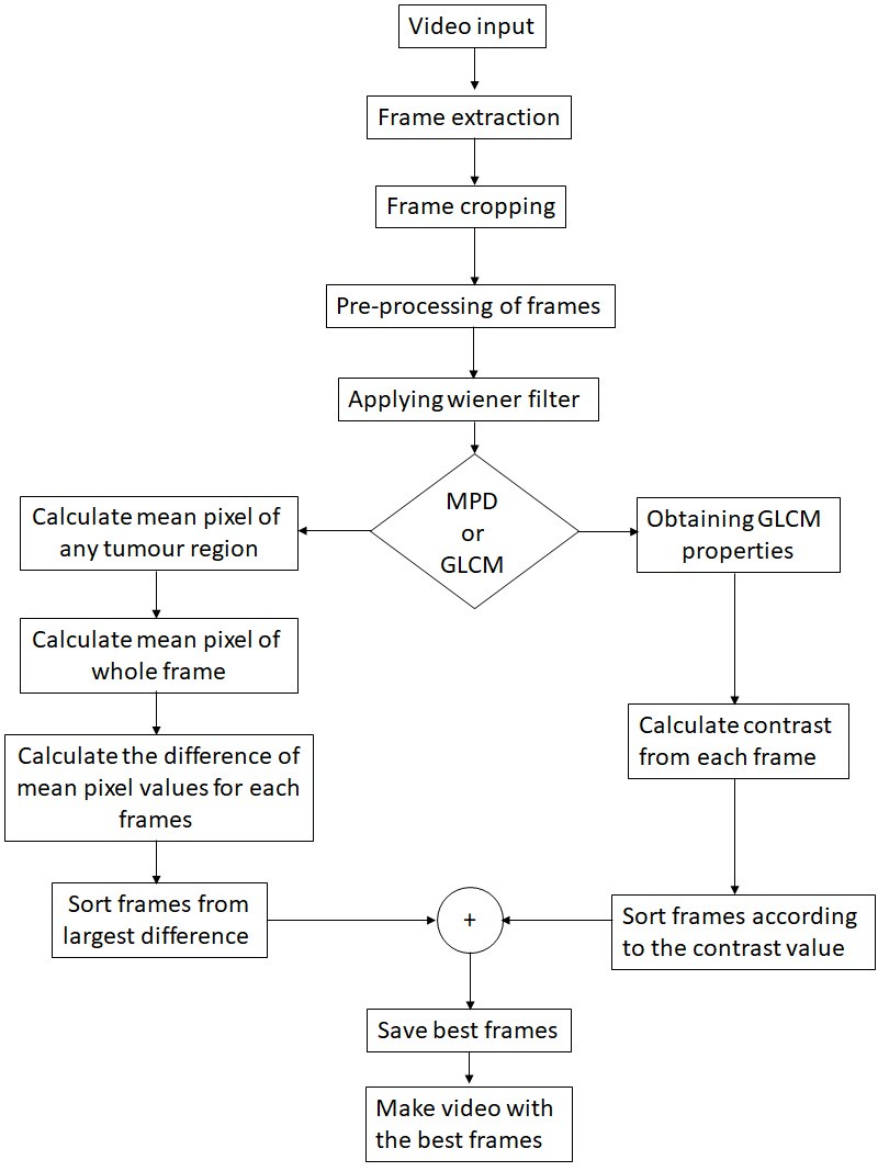

Figure 5.1: Algorithm to find the best frame.

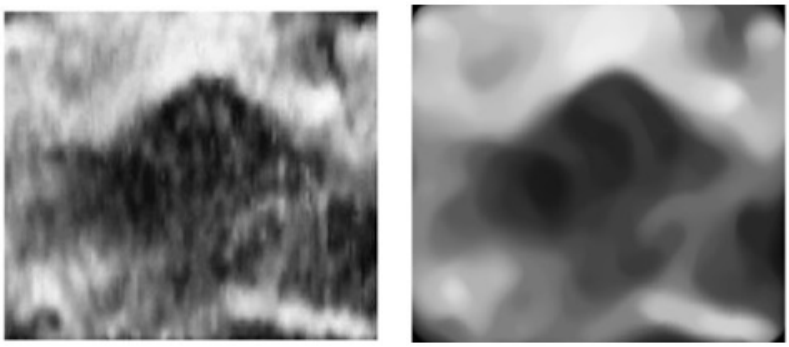

(a) (b)

Figure 5.2: Pre-processing steps: (a) before pre-processing, (b) after pre-processing. Ultrasound taken at 10 MHz frequency and 5 cm depth.

the strain can be estimated and a strain video can be formed. These frames were extracted from the video and stored in the hard drive for processing.

Pre-processing Frames: To reduce noise level and speckles, each frame was processed. If each frame is filtered 7 times using Hybrid Filter consisting of the median and Gaussian filter, the noise level is considerably reduced and becomes easier to process [12]. So, this process was followed to pre-process each frame. Wiener filter is used for de-noising before applying the MPD and GLCM. Wiener filter works well in case of speckles patterns noise [15]. Wavelet based de-noising filte is also tried. However, wavelet based filter gives the same result as wiener filter does though it takes longer time to process.

Applying MPD & GLCM: From the nature of the ultrasound images, we know that the tumour lesion, being denser, has much lower pixel values than the surrounding tissue. As a result, in strain images, the tumour region looks relatively dark while the surrounding tissue looks white.

So, the average pixel value of the whole frame must be higher than the average pixel value of the area where the tumor is confined. If the tumor is not visible in any frame, such a large mean pixel difference will not be present in that frame. As a result, we can distinguish between the required frames and noisy frames using this logic.

This is where the semi-automated CAD was applied. The whole frame and the only tumor region were selected manually. A vague idea about the location of the tumor can be obtained by going through the strain video once. On the basis of that, the tumor region was selected. Then the mathematical mean of the pixel values within both the whole frame and the selected tumor region were found using the following equation:

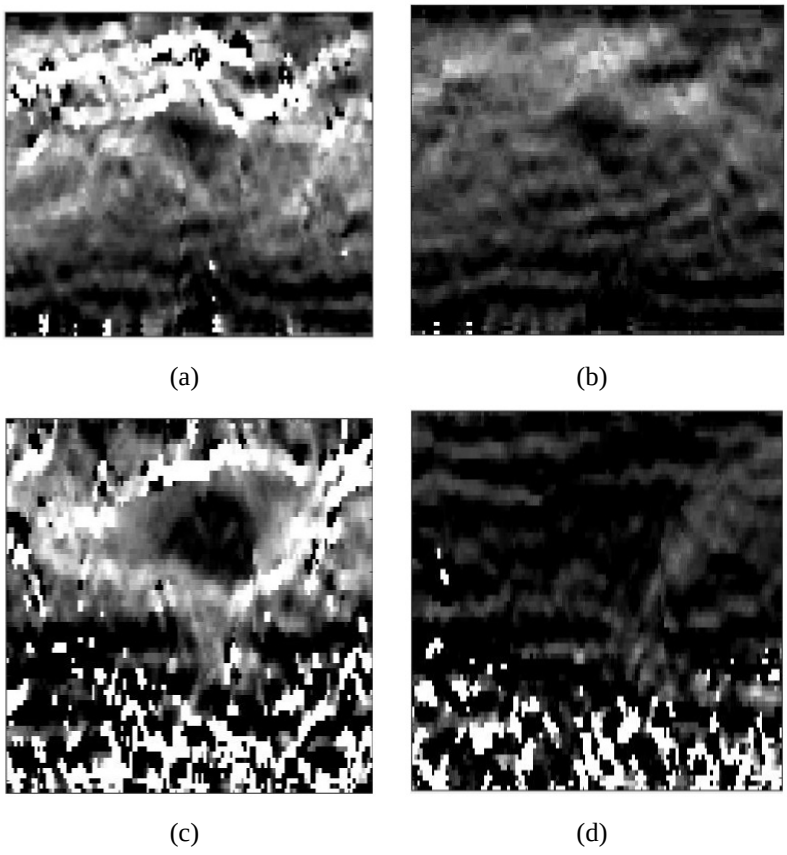

(a) (b)

(c) (d)

Figure 5.3: Some best output frames from strain videos using MPD method.

$$avg = \frac{\sum_{i=1} i^{th}\text{pixel value}}{N} \tag{5.1}$$

Where, N is the number of pixels within the area. Due to human error, it might happen that the tumor might not be detected at the accurate location while taking the ultrasonography. It might move in any random direction. In order to overcome this shortcoming, after selecting the inner tumor region, the selected area was moved towards up, down, right, left, upper right, upper left, down right, down left and the minimum pixel average was taken as the tumor region mean pixel value, because of tumor region having relatively lower pixel values.

After calculating the mean pixel values of both areas, the difference between both mean values was found and stored for each frame. As the frames with good tumor visibility will have a higher mean pixel difference, the frames were sorted according to their MPD. This process was applied to different strain videos and the outputs were noticeably better.

The other way to find the required frames is to calculate the Gray-Level Co-occurrence Matrix (GLCM) properties for each frame as the image descriptor. GLCM is texture

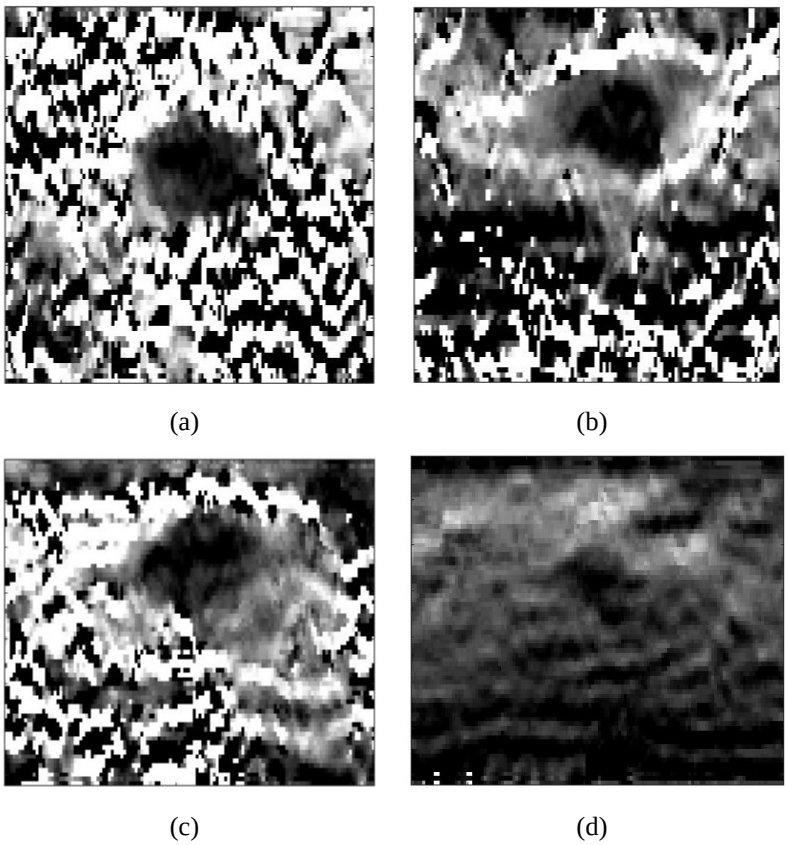

Figure 5.4: Some best output frames from strain video using GLCM contrast method.

character profile and this determines different factors like smoothness, silkiness, roughness and so on [13]. Among all of the features of GLCM, the property of contrast was used. In short form, it is called a CON. Sum of Square Variance is another name of Contrast. It defers the calculation of the intensity contrast linking pixel and its neighbor over the whole image. At constant image, contrast value is 0. In contrast measure, weight increases exponentially (0,1,4,9) as obtained from the diagonal [16].

$$avg = \frac{\sum_{i,j} p(i,j) \left|i-j\right|^2}{N} \tag{5.2}$$

Contrast is the difference in luminance or color that makes an object (or its representation in an image or display) distinguishable. In visual perception of the real world, contrast is determined by the difference in the color and brightness of the object and other objects within the same field of view [14]. GLCM contrast returns a measure of the intensity contrast between a pixel and its neighbor over the whole image. It is low if the tumor is visible and is uniform. If there is noise which makes the tumor not visible, there is no uniformly distributed tumor region and the GLCM contrast value is relatively high. So, if the tumor is more visible in any frame, in other words, distinguishable from the surrounding tissue, it will have lower GLCM contrast value than the not visible ones.

Following this process, GLCM contrast property was calculated for each of the frames and was sorted in ascending order. The corresponding frames were sorted at the same time and the required frames were found. It is observed that for our data set the range of GLCM is between zero to one, whereas for MPD method it is between 0 to 100. This is why a normalizing factor 100 is taken to normalize the MPD value to make comparable to GLCM method. After that by using liner ranking the best frame is selected based on the GLCM and normalized MPD value.

Creating a video with the best frames: A required number of frames were merged to form two videos where the tumor was most visible. Two best frames from both MPD and GLCM contrast methods were taken to form the videos. The doctor/radiologist may use these two videos to identify the tumor easily.

5.3 Result and Analysis

The proposed algorithm was implemented in MATLAB on a personal computer with a 2.5 GHz Intel Core i5 processor 8GB RAM. In this case, several breast ultrasound strain videos were used. $In\ vivo$ breast data were acquired by Louise M. Mobbs and Dr. Brian S. Garra, Department of radiology, Fletcher Allen Health Care, Burlington,

Table 5.1: Missing frames in different methods

Video No.	Missing frame for MPD	Missing frame for GLCM	Missing frame for proposed method
1.	0	1	0
2.	1	1	0
3.	0	0	0
4.	0	0	0

Table 5.2: Performances of different methods.

Total manually selected frames	Missing frame by using GLCM	Frame missing rate for GLCM method	Missing frames by using MPD	Frame missing rate for MPD	Missing frame by using proposed algorithm	Frame missing rate for proposed algorithm
08	02	25.0%	01	12.5%	00	0.0%

VT. The ultrasound images were taken at 6.6 to 14 MHz frequency and at 3.5 cm to 5.0 cm depth. Some of the final output frames are shown in the Figure 5.5. According to the proposed algorithm, both the MPD and GLCM methods are used. After that, the common frames of the selected frames are taken which makes the accuracy high. The proposed method is applied on four (04) strain videos and the result of some strain sequences (Best frame numbers selected manually and by proposed method) are shown in the table 5.2. It is considered that, if the best frame found using the proposed method within 3 frames of the manually selected frames, then it is considered as a correct frame. In every cases, the frame selection shows a significant potential. The visibility is fairly good. A video consisting of a number of frames provided a good visual on the tumor. If the two methods are compared then the MPD method produce the better tumor visibility. For all the strain sequences, two well visible frames are selected and compared with the two afore mentioned methods, as well as with the combination of those two methods. When the combination of those two methods are considered a frame of the from each method is selected and finally all two of them are arranged by ranking.

It is found from the result for a large data set that, frame missing rate for GLCM and MPD method are 18.5% and 11.11%, respectively. One the other hand, the proposed method frame missing rate is almost 3.5% which shows the improvement of the

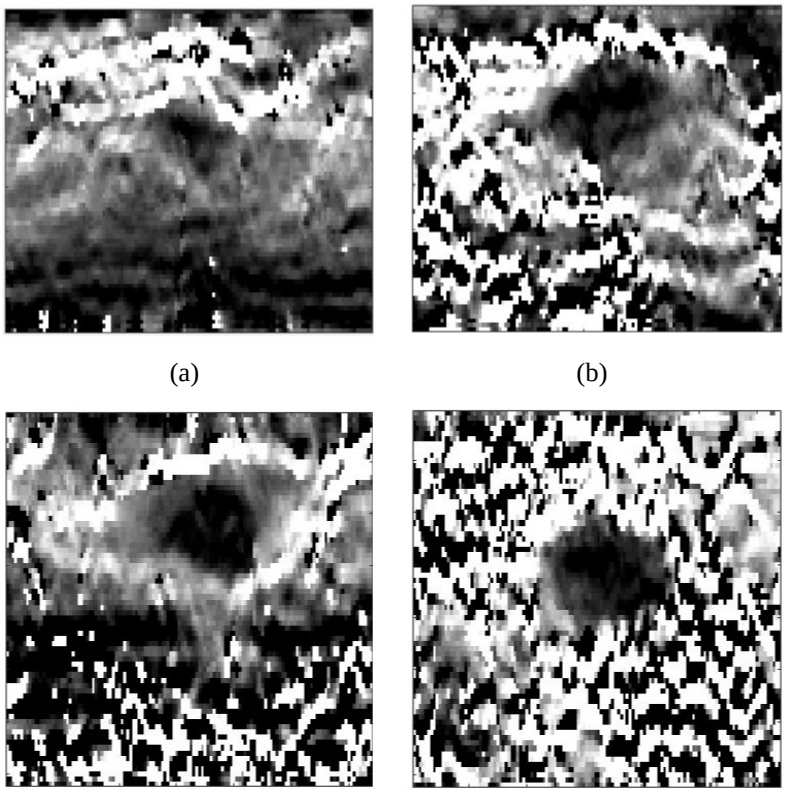

(a) (b)

(c) (d)

Figure 5.5: Some best output frames from strain video using proposed method.

accuracy of the proposed method. However, for a very small data set it gives 0% missing frame rate for the proposed method, which shows the improved accuracy of this method. Added with this fact the high quality strain image produced by the proposed method improves the detection quality.

5.4 Conclusion

In this chapter, an algorithm is discussed which can be used to find out the quality frame from a large number of stain sequences. It significantly improve the tumor detection process and also saves the detection time. In recent years, ultrasonography is becoming more and more popular and thus elastography has been widely used by the clinicians. As one of the safest and cheapest methods of detecting breast cancer, ultrasonography plays a vital rule to fight against it. One of the most complex tasks is to pre-process the frames. A better pre-processing will yield a better result. After collecting the quality frames, the segmentation process could be done easily. It will also improve the visibility of the tumor. Faulty boundary detection may misguide the doctors/radiologists. So the boundary detection should be done with careful selection of the boundary detection algorithm. The proposed algorithm saves time and effort of doctors/radiologists and helps them to detect breast tumor with higher accuracy.

Chapter 6

Conclusion

6.1 Introduction

Modulus value can give the fundamental idea of a tissue stiffness. The main goal of this dissertation is to reconstruct the modulus value by predicting stress value. Here the pre and post compression data provides the strain distribution as the input parameter. On the other hand the stress information collected from the top surface provides a fundamental advantage to predict stress distribution in a lower computational expense. A number of ways to ultrasonic elasticity imagining were considered in the literature review section. Quasistatic methods have the potential advantage of high resolution for depicting the geometry if tissue regions are separated by their relative mechanical properties. Development and implementation of practical form of quasistatic elasticity imagining on general purpose ultrasound machines can bring a lot of clinical benefits. The freehand scanning technique cannot but produce meaningful images but should not be too difficult or labour-intensive for sonographers. Easy implementation of the technique across a wide range of hardware platforms will make it all the more valuable.

This research shows the proposed methodology for unconstrained full inversion based breast elastrography considering the surface pressure of the top surface of the field of view (FOV). This work also shows that, to compute the proper stress distribution the top surface stress information gives a significant advantage. So, it gives a real edge to get the exact quantitative modulus data and the properties of the tumor. Then again, this approach helps so that it can meet a satisfactory level in less computation.

This thesis is carried out focusing on the development of an analytical model of the breast with the tumor referring to the practical physiology of the breast tissue. The main focus of the dissertation is to develop a reconstruction algorithm so that we can estimate stress distribution, which in turn estimate Youngs modulus distribution by knowing the strain distribution and surface stress. Pre and post compression RF data is the source of strain distribution and implanted sensors on the top of the US probe could provide the stress data practically. Proposed approach for the simulated tissue structure

generates a visible satisfactory outcome. Considering the surface stress, the prediction mean error comes very close to 5% by only 6 iterations. Then for every 4 iterations it changes only 2%. Considering 5% error satisfactory, only 6 iterations is enough for the final modulus prediction. Which in turn saves considerable time for reconstruction. It is a very time-consuming process and may consider for practical evaluation purpose. Then again, by not considering the surface stress, it provides a significant error for first 4 iterations. Nevertheless, it gives a very constant and acceptable error from 10% to 6% after 8th iterations. It also shows that the challenge increases to predict as the depth of the tumor increases. Then it considers different size of the tumor. The tumor of 0.1 cm and 0.6 cm radius forms the higher percentage of error which is very noteworthy. And the tumor of 0.3 cm radius forms the lowest percentage of error and 0.4 cm radius tumor forms the second lowest percentage of error. This shows that the prediction algorithm gives better results for a certain size of tumor, a larger or smaller one may get challenges.

After that, it considers the various positions of the tumor and presents the results. Noteworthy experimental result for all the iteration points shows that the predicted modulus generates greater result for the tumors close to the upper surface of the structure. After ten iterations the percentage of error comes to an acceptable percentage around 3.25% to 6% which is observable. For validation, the approach is compared with a real setup carried by S.R. Mousavi $et.\ al.$ [2]. Their phantom structure and the modulus value taken for the background tissue and inclusion was proclaimed in their work by them. The dimension and the displacement on the top surface for their work are also mentioned. The synthetic structure is made and the proposed algorithm is applied in accordance to that guideline. Then comparing the result with the practical data, it provides only 3.39% error for the first phantom inclusion and only 4% error in case of the background tissue. On the basis of that guideline, the artificial structure is developed and the predefined algorithm applied. In case of the second phantom, it gives 3.20% error and 5.6% error for inclusion and background respectively. The results are satisfactory enough.

This dissertation also described and compared with the current technologies for finding the best frame for the strain imaging which can be used for the Modulus imaging as well. Finally GLCM and MPD methods were compared with the proposed one. It shows almost zero percent error in case of proposed method where as MPD and GLCM provide 12.5% and 25% error respectively for a small data set. However for large data set it gives 18.5% and 11.11% missing frame for GLCM and MPD method respectively. On the other hand proposed algorithm gives 3.5% missing frame.

6.2 Future work

In a way, all aspects of ultrasound scanning and quasistatic imaging depend on the scan target. Before clinical testing, the propriety of specific modifications to the tracking, filtering and normalization schemes is ultimately unknown. Therefore feedback between the clinical and technical strands of future work should be beneficial. While some features of the imaging analysis may be advanced for general purpose, other aspects such as normalization may be improved by task-specific modifications which relate to the properties of particular tissues.

The proposed modulus reconstruction algorithm has some interesting and pleasant properties. Definitely, most of the cases it works with the satisfactory result though there remains scope to improve. Further technical development may improve the range of applications and the general utility of the proposed approach.

A few suggestions are now made for strands of future development that are likely to be worthwhile. These strands may be little vague. Maintaining known accuracy followed by creative exploration of the combined deformation and precision data is significant. Deformation estimation and the interface (or post processing) may be two ways of development. The key factor for the ultimate estimation of stress and modulus is deformation estimation. Strain estimation can be enhanced by enacting the efficient algorithm and with a more careful section. For data acquisition, the hardware parts have to be improved, pressure sensor should be implemented on the top of the US probe. The RF signal quality should also be maintained. It should not be hampered by the implanted pressure sensor.

Pertinent 3D tissue structure can be built for the analysis from CT or MRI data of the breast section. For better realization, complexity should be increased. Known skin, fat, background tissue and inclusion modulus and real characteristics should be considered while making phantom. Pre and post compression data should be collected from that phantom and we need to find the strain data with a cautious selection of the tracing algorithm after the validation of the proposed algorithm that can be implemented for clinical application.

So the future work should be focused on hardware implementation, 3D tissue structure simulation and phantom-based data validation.

REFERENCES

[1] J. E. Lindop, "2d and 3d elasticity imaging," Ph.D. dissertation, Pembroke College, University of Cambridge, 2008.

[2] S. R. Mousavi, H. Rivaz, A. Sadeghi-Naini, G. J. Czarnota, and A. Samani, "Breast ultrasound elastography using full inversion-based elastic modulus reconstruction," *IEEE Transactions on Computational Imaging*, vol. 3, no. 4, pp. 774–782, 2017.

[3] J. Ophir, I. Cespedes, H. Ponnekanti, Y. Yazdi, and X. Li, "Elastography: a quantitative method for imaging the elasticity of biological tissues," *Ultrasonic imaging*, vol. 13, no. 2, pp. 111–134, 1991.

[4] R. Blanks, S. Moss, C. McGahan, M. Quinn, and P. Babb, "Effect of nhs breast screening programme on mortality from breast cancer in england and wales, 1990-8: comparison of observed with predicted mortality," *Bmj*, vol. 321, no. 7262, pp. 665–669, 2000.

[5] M. B. Barton, R. Harris, and S. W. Fletcher, "Does this patient have breast cancer?: The screening clinical breast examination: should it be done? how?" *Jama*, vol. 282, no. 13, pp. 1270–1280, 1999.

[6] J. P. Kösters and P. C. Gøtzsche, "Regular self-examination or clinical examination for early detection of breast cancer," *Cochrane Database of Systematic Reviews*, no. 2, 2003.

[7] Y.-C. Fung, "Mechanical properties and active remodeling of blood vessels," in *Biomechanics*. Springer, 1993, pp. 321–391.

[8] J. D. Humphrey, "Continuum biomechanics of soft biological tissues," vol. 459, pp. 3–46, 01 2003.

[9] F. A. Duck, "Physical properties of tissue: A comprehensive reference book," 01 1990.

[10] J. M. Schmitt, "Oct elastography: imaging microscopic deformation and strain of tissue," *Opt. Express*, vol. 3, no. 6, pp. 199–211, Sep 1998.

[11] J. E. Lindop, G. M. Treece, A. H. Gee, and R. W. Prager, “3d elastography using freehand ultrasound,” *Ultrasound in medicine & biology*, vol. 32, no. 4, pp. 529–545, 2006.

[12] R. Dickinson and C. Hill, “Measurement of soft tissue motion using correlation between a-scans,” *Ultrasound in Medicine and Biology*, vol. 8, no. 3, pp. 263–271, 1982.

[13] R. M. Lerner, S. Huang, and K. J. Parker, ““sonoelasticity images derived from ultrasound signals in mechanically vibrated tissues,” *Ultrasound in Medicine and Biology*, vol. 16, no. 3, pp. 231–239, 1990.

[14] Y. Yamakoshi, J. Sato, and T. Sato, “Ultrasonic imaging of internal vibration of soft tissue under forced vibration,” *IEEE transactions on ultrasonics, ferroelectrics, and frequency control*, vol. 37, no. 2, pp. 45–53, 1990.

[15] T. Sugimoto, S. Ueha, and K. Itoh, “Tissue hardness measurement using the radiation force of focused ultrasound,” in *Ultrasonics Symposium, 1990. Proceedings., IEEE 1990*. IEEE, 1990, pp. 1377–1380.

[16] M. Fatemi and J. F. Greenleaf, “Ultrasound-stimulated vibro-acoustic spectrography,” *Science*, vol. 280, no. 5360, pp. 82–85, 1998.

[17] W. L. Duvall, L. B. Croft, and M. E. Goldman, “Can hand-carried ultrasound devices be extended for use by the noncardiology medical community?” *Echocardiography*, vol. 20, no. 5, pp. 471–476, 2003.

[18] P. Doelken and C. Strange, “Chest ultrasound for" dummies",” *Chest*, vol. 123, no. 2, pp. 332–332, 2003.

[19] T. L. Szabo, *Diagnostic ultrasound imaging: inside out*. Academic Press, 2004.

[20] S. I. Nikolov and J. A. Jensen, “In-vivo synthetic aperture flow imaging in medical ultrasound,” *IEEE transactions on ultrasonics, ferroelectrics, and frequency control*, vol. 50, no. 7, pp. 848–856, 2003.

[21] S. Smith, G. Trahey, and O. Von Ramm, “Two-dimensional arrays for medical ultrasound,” *Ultrasonic Imaging*, vol. 14, no. 3, pp. 213–233, 1992.

[22] Hippocrates and F. Adams, *The Genuine Works of Hippocrates; Translated from the Greek; with a Preliminary Discourse and Annotations by Francis Adams*. Sydenham Society, 1849.

[23] B. S. Garra, E. I. Cespedes, J. Ophir, S. R. Spratt, R. A. Zuurbier, C. M. Magnant, and M. F. Pennanen, “Elastography of breast lesions: initial clinical results.” *Radiology*, vol. 202, no. 1, pp. 79–86, 1997.

[24] J. Bercoff, M. Tanter, and M. Fink, "Supersonic shear imaging: a new technique for soft tissue elasticity mapping," *IEEE transactions on ultrasonics, ferroelectrics, and frequency control*, vol. 51, no. 4, pp. 396–409, 2004.

[25] K. T. Spencer, A. S. Anderson, A. Bhargava, A. C. Bales, M. Sorrentino, K. Furlong, and R. M. Lang, "Physician-performed point-of-care echocardiography using a laptop platform compared with physical examination in the cardiovascular patient," *Journal of the American College of Cardiology*, vol. 37, no. 8, pp. 2013–2018, 2001.

[26] F. Bray, J. Ferlay, I. Soerjomataram, R. L. Siegel, L. A. Torre, and A. Jemal, "Global cancer statistics 2018: Globocan estimates of incidence and mortality worldwide for 36 cancers in 185 countries," *CA: a cancer journal for clinicians*, vol. 68, no. 6, pp. 394–424, 2018.

[27] R. L. Siegel, K. D. Miller, and A. Jemal, "Cancer statistics, 2017," *CA: a cancer journal for clinicians*, vol. 67, no. 1, pp. 7–30, 2017.

[28] M. Malvezzi, G. Carioli, P. Bertuccio, P. Boffetta, F. Levi, C. La Vecchia, and E. Negri, "European cancer mortality predictions for the year 2017, with focus on lung cancer," *Annals of Oncology*, vol. 28, no. 5, pp. 1117–1123, 2017.

[29] P. Kennedy, M. Wagner, L. Castera, C. W. Hong, C. L. Johnson, C. B. Sirlin, and B. Taouli, "Quantitative elastography methods in liver disease: current evidence and future directions," *Radiology*, vol. 286, no. 3, pp. 738–763, 2018.

[30] A. R. Skovoroda, A. N. Klishko, D. A. Gusakyan, Y. I. Mayevshki, V. D. Yermilova, G. A. Oranskaya, and A. P. Sarvazyan, "Quantitative analysis of the mechanical characteristics of pathologically changed soft biological tissues," *Biophysics*, vol. 40, p. 1359–1364, Jun. 1995.

[31] T. L. Chenevert, A. R. Skovoroda, M. O donnell, and S. Y. Emelianov, "Elasticity reconstructive imaging by means of stimulated echo mri," *Magnetic resonance in medicine*, vol. 39, no. 3, pp. 482–490, 1998.

[32] D. Kirbach and T. Whittingham, "3d ultrasound-the kretztechnik voluson approach," *Eur J Ultrasound*, vol. 1, pp. 85–89, 1994.

[33] A. Gee, R. Prager, G. Treece, and L. Berman, "Engineering a freehand 3d ultrasound system," *Pattern Recognition Letters*, vol. 24, no. 4-5, pp. 757–777, 2003.

[34] S. Catheline, F. Wu, and M. Fink, "A solution to diffraction biases in sonoelasticity: the acoustic impulse technique," *The Journal of the Acoustical Society of America*, vol. 105, no. 5, pp. 2941–2950, 1999.

[35] T. J. Hall, Y. Zhu, and C. S. Spalding, "In vivo real-time freehand palpation imaging," *Ultrasound in medicine & biology*, vol. 29, no. 3, pp. 427–435, 2003.

[36] R. Muthupillai, D. Lomas, P. Rossman, J. F. Greenleaf, A. Manduca, and R. Ehman, "Magnetic resonance elastography by direct visualization of propagating acoustic strain waves," *Science*, vol. 269, no. 5232, pp. 1854–1857, 1995.

[37] A. Pesavento and A. Lorenz, "Real time strain imaging—a new ultrasonic method for cancer detection: first study results," in *Proceedings of IEEE Ultrasonics Symposium*, 2001, pp. 1647–1652.

[38] N. Miyanaga, H. Akaza, M. Yamakawa, T. Oikawa, N. Sekido, S. Hinotsu, K. Kawai, T. Shimazui, and T. Shiina, "Tissue elasticity imaging for diagnosis of prostate cancer: a preliminary report," *International journal of urology*, vol. 13, no. 12, pp. 1514–1518, 2006.

[39] L. Sandrin, B. Fourquet, J.-M. Hasquenoph, S. Yon, C. Fournier, F. Mal, C. Christidis, M. Ziol, B. Poulet, F. Kazemi *et al.*, "Transient elastography: a new noninvasive method for assessment of hepatic fibrosis," *Ultrasound in medicine & biology*, vol. 29, no. 12, pp. 1705–1713, 2003.

[40] C. L. De Korte, A. F. Van Der Steen, E. I. Céspedes, and G. Pasterkamp, "Intravascular ultrasound elastography in human arteries: initial experience in vitro," *Ultrasound in medicine & biology*, vol. 24, no. 3, pp. 401–408, 1998.

[41] J.-L. Gennisson, T. Baldeweck, M. Tanter, S. Catheline, M. Fink, L. Sandrin, C. Cornillon, and B. Querleux, "Assessment of elastic parameters of human skin using dynamic elastography," *IEEE transactions on ultrasonics, ferroelectrics, and frequency control*, vol. 51, no. 8, pp. 980–989, 2004.

[42] M. Vogt and H. Ermert, "Development and evaluation of a high-frequency ultrasound-based system for in vivo strain imaging of the skin," *IEEE transactions on ultrasonics, ferroelectrics, and frequency control*, vol. 52, no. 3, pp. 375–385, 2005.

[43] T. Fitzpatrick and I. Freedberg, "Fitzpatrick's dermatology in general medicine, ed 6. new york city," *McGraw-Hill*, vol. 2, pp. 2059–2060, 2003.

[44] S. Emelianov, X. Chen, M. O'donnell, B. Knipp, D. Myers, T. Wakefield, and J. Rubin, "Triplex ultrasound: elasticity imaging to age deep venous thrombosis," *Ultrasound in medicine & biology*, vol. 28, no. 6, pp. 757–767, 2002.

[45] J. A. Schaar, C. L. de Korte, F. Mastik, C. Strijder, G. Pasterkamp, E. Boersma, P. W. Serruys, and A. F. van der Steen, "Characterizing vulnerable plaque fea-

tures with intravascular elastography," *Circulation*, vol. 108, no. 21, pp. 2636–2641, 2003.

[46] K. Kaluzynski, X. Chen, S. Y. Emelianov, A. R. Skovoroda, and M. O'Donnell, "Strain rate imaging using two-dimensional speckle tracking," *IEEE transactions on ultrasonics, ferroelectrics, and frequency control*, vol. 48, no. 4, pp. 1111–1123, 2001.

[47] J. D'hooge, B. Bijnens, J. Thoen, F. Van de Werf, G. R. Sutherland, and P. Suetens, "Echocardiographic strain and strain-rate imaging: a new tool to study regional myocardial function," *IEEE transactions on medical imaging*, vol. 21, no. 9, pp. 1022–1030, 2002.

[48] R. Righetti, F. Kallel, R. J. Stafford, R. E. Price, T. A. Krouskop, J. D. Hazle, and J. Ophir, "Elastographic characterization of hifu-induced lesions in canine livers," *Ultrasound in medicine & biology*, vol. 25, no. 7, pp. 1099–1113, 1999.

[49] J. Bercoff, M. Pernot, M. Tanter, and M. Fink, "Monitoring thermally-induced lesions with supersonic shear imaging," *Ultrasonic imaging*, vol. 26, no. 2, pp. 71–84, 2004.

[50] A. Chakraborty, G. Berry, J. Bamber, and N. Dorward, "Intra-operative ultrasound elastography and registered magnetic resonance imaging of brain tumours: a feasibility study," *Ultrasound*, vol. 14, no. 1, pp. 43–49, 2006.

[51] L. Landau, "Em lifshitz theory of elasticity," *Course of theoretical physics*, vol. 7, 1986.

[52] W. Flugge, "Viscoelasticity, blaisdell pub," *Co., Waltham, MA*, p. 92, 1967.

[53] V. C. Mow and W. M. Lai, "Recent developments in synovial joint biomechanics," *Siam Review*, vol. 22, no. 3, pp. 275–317, 1980.

[54] G. P. Berry, J. C. Bamber, C. G. Armstrong, N. R. Miller, and P. E. Barbone, "Towards an acoustic model-based poroelastic imaging method: I. theoretical foundation," *Ultrasound in medicine & biology*, vol. 32, no. 4, pp. 547–567, 2006.

[55] S. Shapiro, "The status of breast cancer screening: a quarter of a century of research," *World journal of surgery*, vol. 13, no. 1, pp. 9–18, 1989.

[56] A. P. Sarvazyan, O. V. Rudenko, S. D. Swanson, J. B. Fowlkes, and S. Y. Emelianov, "Shear wave elasticity imaging: a new ultrasonic technology of medical diagnostics," *Ultrasound in medicine & biology*, vol. 24, no. 9, pp. 1419–1435, 1998.

[57] J. F. Young, A. Bentur, and S. Mindess, "The science and technology of civil engineering materials," 1998.

[58] A. Tarantola, *Inverse problem theory and methods for model parameter estimation*. siam, 2005, vol. 89.

[59] P. E. Barbone and J. C. Bamber, "Quantitative elasticity imaging: what can and cannot be inferred from strain images," *Physics in Medicine & Biology*, vol. 47, no. 12, p. 2147, 2002.

[60] P. G. Ciarlet, B. Miara, and J.-M. Thomas, *Introduction to numerical linear algebra and optimisation*. Cambridge University Press, 1989.

[61] M. F. Insana, C. Pellot-Barakat, M. Sridhar, and K. K. Lindfors, "Viscoelastic imaging of breast tumor microenvironment with ultrasound," *Journal of mammary gland biology and neoplasia*, vol. 9, no. 4, pp. 393–404, 2004.

[62] S. Chen, M. Fatemi, and J. F. Greenleaf, "Quantifying elasticity and viscosity from measurement of shear wave speed dispersion," *The Journal of the Acoustical Society of America*, vol. 115, no. 6, pp. 2781–2785, 2004.

[63] R. Sinkus, M. Tanter, T. Xydeas, S. Catheline, J. Bercoff, and M. Fink, "Viscoelastic shear properties of in vivo breast lesions measured by mr elastography," *Magnetic resonance imaging*, vol. 23, no. 2, pp. 159–165, 2005.

[64] R. Righetti, J. Ophir, S. Srinivasan, and T. A. Krouskop, "The feasibility of using elastography for imaging the poisson's ratio in porous media," *Ultrasound in medicine & biology*, vol. 30, no. 2, pp. 215–228, 2004.

[65] G. P. Berry, J. C. Bamber, N. R. Miller, P. E. Barbone, N. L. Bush, and C. G. Armstrong, "Towards an acoustic model-based poroelastic imaging method: Ii. experimental investigation," *Ultrasound in medicine & biology*, vol. 32, no. 12, pp. 1869–1885, 2006.

[66] J. F. Greenleaf, M. Fatemi, and M. Insana, "Selected methods for imaging elastic properties of biological tissues," *Annual review of biomedical engineering*, vol. 5, no. 1, pp. 57–78, 2003.

[67] D. Napolitano, C.-H. Chou, G. McLaughlin, T.-L. Ji, L. Mo, D. DeBusschere, and R. Steins, "Sound speed correction in ultrasound imaging," *Ultrasonics*, vol. 44, pp. e43–e46, 2006.

[68] S. Catheline, J.-L. Gennisson, M. Tanter, and M. Fink, "Observation of shock transverse waves in elastic media," *Physical review letters*, vol. 91, no. 16, p. 164301, 2003.

[69] K. J. Parker, L. S. Taylor, S. Gracewski, and D. J. Rubens, "A unified view of imaging the elastic properties of tissue," *The Journal of the Acoustical Society of America*, vol. 117, no. 5, pp. 2705–2712, 2005.

[70] T. Matsumura, S. Tamano, R. Shinomura, T. Mitake, M. Yamakawa, T. Shiina, A. Itoh, and E. Ueno, "Diagnostic results for breast disease by real-time elasticity imaging system," in *Ultrasonics Symposium, 2004 IEEE*, vol. 2. IEEE, 2004, pp. 1484–1487.

[71] C. L. De Korte, E. I. Cespedes, A. Van Der Steen, G. Pasterkamp, and N. Bom, "Intravascular ultrasound elastography: assessment and imaging of elastic properties of diseased arteries and vulnerable plaque." *European journal of ultrasound: official journal of the European Federation of Societies for Ultrasound in Medicine and Biology*, vol. 7, no. 3, p. 219, 1998.

[72] H. Ponnekanti, J. Ophir, and I. Cespedes, "Axial stress distributions between coaxial compressors in elastography: an analytical model," *Ultrasound in Medicine and Biology*, vol. 18, no. 8, pp. 667–673, 1992.

[73] G. M. Treece, A. H. Gee, and R. W. Prager, "Rf and amplitude-based probe pressure correction for 3d ultrasound," *Ultrasound in medicine & biology*, vol. 31, no. 4, pp. 493–503, 2005.

[74] D. W. Baker, "Pulsed ultrasonic doppler blood-flow sensing," *IEEE SU*, vol. 17, pp. 170–185, 1975.

[75] C. Kasai, K. Namekawa, A. Koyano, and R. Omoto, "Real-time two-dimensional blood flow imaging using an autocorrelation technique," *IEEE Transactions on sonics and ultrasonics*, vol. 32, no. 3, pp. 458–464, 1985.

[76] A. Pesavento, C. Perrey, M. Krueger, and H. Ermert, "A time-efficient and accurate strain estimation concept for ultrasonic elastography using iterative phase zero estimation," *IEEE transactions on ultrasonics, ferroelectrics, and frequency control*, vol. 46, no. 5, pp. 1057–1067, 1999.

[77] T. Varghese and J. Ophir, "A theoretical framework for performance characterization of elastography: The strain filter," *IEEE transactions on ultrasonics, ferroelectrics, and frequency control*, vol. 44, no. 1, pp. 164–172, 1997.

[78] C. Sumi and K. Nakayama, "A robust numerical solution to reconstruct a globally relative shear modulus distribution from strain measurements," *IEEE transactions on medical imaging*, vol. 17, no. 3, pp. 419–428, 1998.

[79] K. Raghavan and A. E. Yagle, "Forward and inverse problems in elasticity imaging of soft tissues," *IEEE Transactions on nuclear science*, vol. 41, no. 4, pp. 1639–1648, 1994.

[80] F. Kallel and M. Bertrand, "Tissue elasticity reconstruction using linear perturbation method," *IEEE Transactions on Medical Imaging*, vol. 15, no. 3, pp. 299–313, 1996.

[81] M. Doyley, P. Meaney, and J. Bamber, "Evaluation of an iterative reconstruction method for quantitative elastography," *Physics in Medicine & Biology*, vol. 45, no. 6, p. 1521, 2000.

[82] S. R. Aglyamov, A. R. Skovoroda, H. Xie, K. Kim, J. M. Rubin, M. O'Donnell, T. W. Wakefield, D. Myers, and S. Y. Emelianov, "Model-based reconstructive elasticity imaging using ultrasound," *International journal of biomedical imaging*, vol. 2007, 2007.

[83] D. M. Regner, G. K. Hesley, N. J. Hangiandreou, M. J. Morton, M. R. Nordland, D. D. Meixner, T. J. Hall, M. A. Farrell, J. N. Mandrekar, W. S. Harmsen *et al.*, "Breast lesions: evaluation with us strain imaging–clinical experience of multiple observers," *Radiology*, vol. 238, no. 2, pp. 425–437, 2006.

[84] W. Svensson and D. Amiras, "Ultrasound elasticity imaging," *Breast Cancer Online*, vol. 9, no. 6, pp. 1–7, 2006.

[85] T. A. Krouskop, T. M. Wheeler, F. Kallel, B. S. Garra, and T. Hall, "Elastic moduli of breast and prostate tissues under compression," *Ultrasonic imaging*, vol. 20, no. 4, pp. 260–274, 1998.

[86] H. Ponnekanti, J. Ophir, Y. Huang, and I. Céspedes, "Fundamental mechanical limitations on the visualization of elasticity contrast in elastography," *Ultrasound in Medicine and Biology*, vol. 21, no. 4, pp. 533–543, 1995.

[87] L. Gao, K. Parker, S. Alam, and R. Lerner, "Sonoelasticity imaging: theory and experimental verification," *The Journal of the Acoustical Society of America*, vol. 97, no. 6, pp. 3875–3886, 1995.

[88] L. Taylor, B. Porter, D. Rubens, and K. Parker, "Three-dimensional sonoelastography: principles and practices," *Physics in Medicine & Biology*, vol. 45, no. 6, p. 1477, 2000.

[89] K. Parker, S. Huang, R. Musulin, and R. Lerner, "Tissue response to mechanical vibrations for "sonoelasticity imaging" *Ultrasound in medicine & biology*, vol. 16, no. 3, pp. 241–246, 1990.

[90] S.-R. Huang, R. M. Lerner, and K. J. Parker, "On estimating the amplitude of harmonic vibration from the doppler spectrum of reflected signals," *The Journal of the Acoustical Society of America*, vol. 88, no. 6, pp. 2702–2712, 1990.

[91] K. J. Parker, D. Fu, S. M. Graceswki, F. Yeung, and S. F. Levinson, "Vibration sonoelastography and the detectability of lesions," *Ultrasound in medicine & biology*, vol. 24, no. 9, pp. 1437–1447, 1998.

[92] Z. Wu, L. S. Taylor, D. J. Rubens, and K. J. Parker, "Shear wave focusing for three-dimensional sonoelastography," *The Journal of the Acoustical Society of America*, vol. 111, no. 1, pp. 439–446, 2002.

[93] D. J. Rubens, M. A. Hadley, S. K. Alam, L. Gao, R. D. Mayer, and K. J. Parker, "Sonoelasticity imaging of prostate cancer: in vitro results." *Radiology*, vol. 195, no. 2, pp. 379–383, 1995.

[94] L. S. Taylor, D. J. Rubens, B. C. Porter, Z. Wu, R. B. Baggs, P. A. di Sant'Agnese, G. Nadasdy, D. Pasternack, E. M. Messing, P. Nigwekar *et al.*, "Prostate cancer: three-dimensional sonoelastography for in vitro detection," *Radiology*, vol. 237, no. 3, pp. 981–985, 2005.

[95] M. Sanada, M. Ebara, H. Fukuda, M. Yoshikawa, N. Sugiura, H. Saisho, Y. Yamakoshi, K. Ohmura, A. Kobayashi, and F. Kondoh, "Clinical evaluation of sonoelasticity measurement in liver using ultrasonic imaging of internal forced low-frequency vibration," *Ultrasound in medicine & biology*, vol. 26, no. 9, pp. 1455–1460, 2000.

[96] N. Masuda, T. Tsujita, T. Ebuchi, and Y. Yamakoshi, "Low-frequency elastic wave imaging by adaptive combination of fundamental and tissue harmonic ultrasonic waves," *Japanese journal of applied physics*, vol. 42, no. 5S, p. 3271, 2003.

[97] Z. Wu, L. S. Taylor, D. J. Rubens, and K. J. Parker, "Sonoelastographic imaging of interference patterns for estimation of the shear velocity of homogeneous biomaterials," *Physics in Medicine & Biology*, vol. 49, no. 6, p. 911, 2004.

[98] J. McLaughlin, D. Renzi, K. Parker, and Z. Wu, "Shear wave speed recovery using moving interference patterns obtained in sonoelastography experiments," *The Journal of the Acoustical Society of America*, vol. 121, no. 4, pp. 2438–2446, 2007.

[99] Z. Wu, K. Hoyt, D. J. Rubens, and K. J. Parker, "Sonoelastographic imaging of interference patterns for estimation of shear velocity distribution in biomaterials," *The Journal of the Acoustical Society of America*, vol. 120, no. 1, pp. 535–545, 2006.

[100] K. Hoyt, K. J. Parker, and D. J. Rubens, "Real-time shear velocity imaging using sonoelastographic techniques," *Ultrasound in medicine & biology*, vol. 33, no. 7, pp. 1086–1097, 2007.

[101] M. Fatemi and J. F. Greenleaf, "Vibro-acoustography: An imaging modality based on ultrasound-stimulated acoustic emission," *Proceedings of the National Academy of Sciences*, vol. 96, no. 12, pp. 6603–6608, 1999.

[102] A. Alizad, M. Fatemi, L. E. Wold, and J. F. Greenleaf, "Performance of vibro-acoustography in detecting microcalcifications in excised human breast tissue: A study of 74 tissue samples," *IEEE transactions on medical imaging*, vol. 23, no. 3, pp. 307–312, 2004.

[103] M. Fatemi, L. E. Wold, A. Alizad, and J. F. Greenleaf, "Vibro-acoustic tissue mammography," *IEEE transactions on medical imaging*, vol. 21, no. 1, pp. 1–8, 2002.

[104] A. Alizad, L. E. Wold, J. F. Greenleaf, and M. Fatemi, "Imaging mass lesions by vibro-acoustography: modeling and experiments," *IEEE transactions on medical imaging*, vol. 23, no. 9, pp. 1087–1093, 2004.

[105] L. Sandrin, S. Catheline, M. Tanter, X. Hennequin, and M. Fink, "Time-resolved pulsed elastography with ultrafast ultrasonic imaging," *Ultrasonic imaging*, vol. 21, no. 4, pp. 259–272, 1999.

[106] L. Sandrin, M. Tanter, J.-L. Gennisson, S. Catheline, and M. Fink, "Shear elasticity probe for soft tissues with 1-d transient elastography," *IEEE transactions on ultrasonics, ferroelectrics, and frequency control*, vol. 49, no. 4, pp. 436–446, 2002.

[107] L. Sandrin, M. Tanter, S. Catheline, and M. Fink, "Shear modulus imaging with 2-d transient elastography," *IEEE transactions on ultrasonics, ferroelectrics, and frequency control*, vol. 49, no. 4, pp. 426–435, 2002.

[108] K. Nightingale, "Acoustic radiation force impulse (arfi) imaging: a review," *Current medical imaging reviews*, vol. 7, no. 4, pp. 328–339, 2011.

[109] M. Tanter, J. Bercoff, A. Athanasiou, T. Deffieux, J.-L. Gennisson, G. Montaldo, M. Muller, A. Tardivon, and M. Fink, "Quantitative assessment of breast lesion viscoelasticity: initial clinical results using supersonic shear imaging," *Ultrasound in medicine & biology*, vol. 34, no. 9, pp. 1373–1386, 2008.

[110] Y. Zhu, T. J. Hall, and J. Jiang, "A finite-element approach for young's modulus reconstruction," *IEEE transactions on medical imaging*, vol. 23, no. 7, pp. 890–901, 2003.

[111] P. Forrest, *Breast cancer screening: report to the Health Ministers of England, Wales, Scotland & Northern Ireland*. HMSO, 1986.

[112] C. E. Rasmussen, "Gaussian processes in machine learning," in *Advanced lectures on machine learning*. Springer, 2004, pp. 63–71.

[113] A. Joshi and R. Kaur, "A review: Comparative study of various clustering techniques in data mining," *International Journal of Advanced Research in Computer Science and Software Engineering*, vol. 3, no. 3, 2013.

[114] A. Gefen and B. Dilmoney, “Mechanics of the normal woman’s breast,” *Technology and Health Care*, vol. 15, no. 4, pp. 259–271, 2007.

[115] S. R. Mousavi, H. Rivaz, A. Sadeghi-Naini, G. J. Czarnota, and A. Samani, “Breast ultrasound elastography using full inversion-based elastic modulus reconstruction,” *IEEE Transactions on Computational Imaging*, vol. 3, no. 4, pp. 774–782, 2017.

[116] A. Samani, J. Zubovits, and D. Plewes, “Elastic moduli of normal and pathological human breast tissues: an inversion-technique-based investigation of 169 samples,” *Physics in medicine & biology*, vol. 52, no. 6, p. 1565, 2007.